Technische Universität München

Fakultät für Medizin

Nuklearmedizinische Klinik und Poliklinik, Klinikum rechts der Isar

Galectin-3 immunotargeting as a novel approach for thyroid nodules characterization and thyroid cancer imaging

Francesco De Rose

Vollständiger Abdruck der von der Fakultät für Medizin der Technischen Universität München zur Erlangung des akademischen Grades eines Doktors der Naturwissenschaften (Dr.rer.nat.) genehmigten Dissertation.

Vorsitzender:	Prof. Dr. Hana Algül
Prüfer der Dissertation:	1. Prof. Dr. Markus Schwaiger
	2. Prof. Dr. Gabriele Multhoff
	3. Prof. Dr. Arne Skerra

Die Dissertation wurde am 06.02.2020 bei der Technischen Universität München eingereicht und durch die Fakultät für Medizin am 11.08.2020 angenommen.

To my grandfather Natale

TABLE OF CONTENTS

FIGURE INDEX

TABLE INDEX

SUMMARY

Thyroid cancer (TC) is the most common endocrine malignancy and its incidence and mortality are increasing over the last years. The lack of a rapid and direct method for the biological characterization of thyroid nodules, combined with the significant incidence of benignant lesion, makes the thyroid cancer diagnosis challenging. This translates often for the patients into a long series of diagnostic studies and unnecessary surgery.

The β-galactoside binding protein galectin-3 has been proved to be a reliable thyroid cancer biomarker, since its expression is restricted to thyroid follicular, papillar and undifferentiated carcinomas while it is absent in normal thyrocytes or benign nodules. Therefore, with the goal to investigate the possibility to improve the thyroid cancer diagnosis, a specific *in vivo* positron emission tomography (PET) imaging approach was developed using ^{89}Zr-labeled antibodies (immuno-PET) against galectin-3. This method was compared with the sodium-iodide symporter (NIS) mediated radio-iodine imaging, considered as the golden standard for thyroid imaging. To mimic the human condition during the *in vivo* experiments, orthotopic murine models of papillar (BcPAP) and anaplastic (CAL62 and FRO82-1) thyroid cancers were established inoculating the tumor cells in the left thyroid lobe of mouse thyroid.

An immuno-PET tracer, ^{89}Zr-DFO-F(ab')$_2$, was tested *in vitro* for cell binding on monolayer cultures and on spheroids, a 3D cell model reproducing the *in vivo* cell-to-cell interactions. Our tracer showed high antigen affinity, high immunoreactivity and stability. *In vivo* studies demonstrated, moreover, high specificity and selective accumulation in TC. PET/CT imaging exhibited for all the cell lines studied an excellent image contrast, specific signal associated to the orthotopic-implanted tumors and no uptake in the tumor-free thyroid lobe.

This work demonstrated for the first time that galectin-3 targeting outperforms the radioiodine-based imaging by specifically targeting tumor tissue helping to discriminate between benign nodules and thyroid tumor lesions. The translation of this method into clinical setting promises to improve the management of patients with thyroid nodules and reduce unnecessary thyroid surgery.

1 **INTRODUCTION**

1.1 Thyroid cancer

Thyroid cancer (TC) is a disease that includes a variety of lesions occurring in the thyroid gland with different progression and mortality, caused by an abnormal growth of cells with the potential to metastasize in other parts of the body. It comprises a spectrum of diseases ranging from indolent papillary carcinoma to anaplastic carcinoma, a cancer with fatal prognosis.

While the age-adjusted incidence of many cancer has significantly decreased over the last years, the incidence of thyroid cancer has significantly increased, tripling from 1983 to 2012 (Morris et al. 2016). To date, TC presents the fastest growing cancer incidence rates in men and women since 2005 (Morris, Tuttle, and Davies 2016; Siegel, Miller, and Jemal 2018) and it is the most common endocrine cancer in the USA and Australia (Ferlay et al. 2015).

Thyroid cancers develop both from thyrocytes (follicular epithelial cells) and from neuroendocrine C cells (calcitonin-producing parafollicular cells) (Figure 1). The World Health Organization (WHO) classifies the TCs according to their derivation and morphological characteristics (Lloyd et al. 2017), see Table 1 for classification and statistic details.

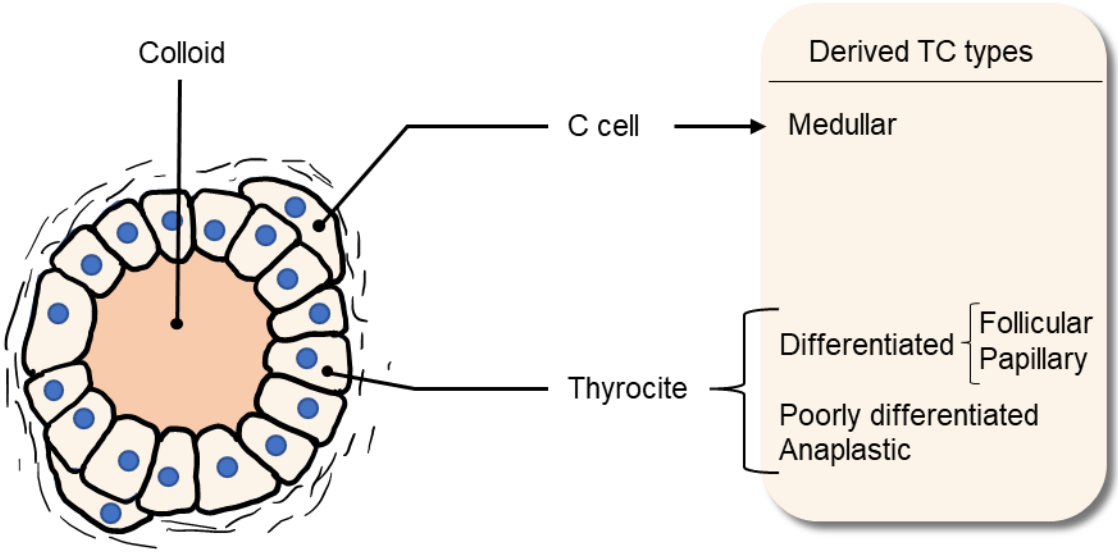

Figure 1. Bidimensional structure of a thyroid follicle, functional unit of the thyroid parenchyma and list of the most common TCs.

Follicular-derived cancers are distinguished among:

- Papillary thyroid carcinoma (PTC), the most common form of thyroid cancer, representing more than 70% of cases. This type of cancer shows evidence of follicular

differentiation and possesses characteristic morphological features as papillae and large nuclei with irregular contours and grooves. Other common anatomical features are poorly defined margins and the presence of psammoma bodies (concentric calcified constructs). PTC has excellent prognosis that was demonstrated to be dependent on clinical extent of the disease and dimension of the tumor (Gilliland et al. 1997).

- Follicular thyroid carcinoma (FTC), the second most common type of thyroid cancer, includes more than 10% of all thyroid carcinomas. All the thyroid malignancies presenting follicular differentiation, in combination with a tick and irregular encapsulation and lack of the typical PTC nuclear features, fall in the definition of FTC. The FTCs are further divided in three subclasses based on the invasiveness of the tumor: minimally invasive without vascular invasion (MI FTC), minimally invasive with vascular invasion (angioinvasive MI FTC) and widely invasive (WI FTC). The disease-free survival is >80% and strongly dependent from the degree of vascular invasion (O'Neill et al. 2011).
- Anaplastic (undifferentiated) thyroid carcinoma (ATC), is the rarest thyrocytes-derived cancer type, but the most aggressive, with a 10-year survival rate <15%. It is characterized by the loss of follicular differentiation being negative to thyroglobulin expression, an infiltrative growth with local invasion, and distant metastasis in lungs, bones, pleura and brain.
- Poorly-differentiated thyroid carcinoma (PDTC), is an aggressive cancer form that shows characteristics and prognosis intermediate between differentiated and anaplastic thyroid cancer (Nishida et al. 1999). The histopathological criteria for the diagnosis of PDTCs were listed in the Turin proposal (Volante et al. 2007): 1) presence of clusters with solid, trabecular or insular morphology; 2) absence of PTC nuclear features; 3) one among hyperchromatic nuclei, increased mitoses or necrosis.

Medullary thyroid carcinoma (MTC) is generated from C cells, accounting for around the 3% of all thyroid cancer cases and presenting a 10-year survival rate >70%. Typical features of this cancer are the positivity to calcitonin staining, with a related high level of this protein in the

serum, and a circumscribed but non-encapsulated tumor mass. Histological pattern can have a wide variety of appearances and psammoma bodies are common.

Less frequent classifications include Hürtle cells tumors, haematolymphoids tumors, squamous cell carcinomas and soft tissues sarcomas.

Table 1. *Thyroid cancer classification and statistic details.*

TC type	Derivation	Prevalence among TCs	10-years survival rate	Median age group at diagnosis
Papillar (differentiated)	Follicular cells	64–91%[1,2]	98-93%[3,4]	40-49[1]
Follicular (differentiated)	Follicular cells	5-17%[1,2]	92-85%[3,4]	40-49[1]
Poorly differentiated	Follicular cells	0.3-6.7%[5]	50-45%[6]	50-59[6]
Anaplastic (undifferentiated)	Follicular cells	2-4%[1,2]	14-13%[3,4]	>69[1]
Medullar	C cells	2-5%[2,5]	80-75%[3,4]	30-39[1]

References: 1 (Hundahl et al. 2000), 2 (Dal Maso et al. 2017), 3 (Hundahl et al. 1998), 4 (Gilliland et al. 1997), 5 (Lloyd et al. 2017), 6 (Nishida et al. 1999)

1.1.1 Thyroid cancer genetic profile

In the last 20 years, after the release of the first human genome sequence draft, the interest of the scientific community focalized on the research of cancer mutation profiles with the perspective of a better knowledge of the etiology and the development of new treatments. Nowadays, most of the TC-causing mutations are known as well as secondary mutations. The use of these genetic abnormalities as diagnostic biomarker has been proposed but not yet validated (Lloyd et al. 2017). Activating mutations of the BRAF and RAS genes, as well as rearrangements of RET and PPARG genes, involving misregulations of the mitogen-activated protein kinases (MAPK) and PI_3K/ATK/mTOR pathways, are the most common genetic alterations found in TC (Clark et al. 2016). These mutations are mutually exclusive and accumulate with secondarily genetic events, suggesting a multistep carcinogenesis model (Nikiforova and Nikiforov 2009).

BRAF mutations and RET rearrangements are exclusive of PTC and of the derivative poorly-differentiated and anaplastic tumors. The most common BRAF mutation is the BRAFV600E

point mutation, occurring in 45-70% of PTCs (Nikiforova, Kimura, et al. 2003). It is associated with the progression to undifferentiated forms and to the decrease of the transmembrane glycoprotein sodium-iodide symporter (NIS) expression (Riesco-Eizaguirre et al. 2006; Ricarte-Filho et al. 2009). PDTC and ATC bringing this mutation often present extrathyrodeal extension and lymph node metastases (Xing et al. 2009; Basolo et al. 2010). The RET/PTC rearrangements are found in 10-12% of PTC cases and correlates often with indeterminate diagnoses (Marotta et al. 2011). Despite the fact that tumors harboring RET/PTC rearrangements rarely show dedifferentiation, they present high risk of metastasis when occurring at young age (Adeniran et al. 2006).

FTC and dedifferentiated carcinomas originated from these show a prevalence of RAS family mutations (30-50%), including KRAS, HRAS and NRAS, that rarely occur also in PTC (0-5%) (Clark et al. 2016). Meanwhile in PTC this mutation is often related to encapsulated malignancies, in FTC it correlates with an adverse prognosis and differentiation (Wreesmann et al. 2004).

Another FTC-exclusive abnormality is represented by the PPARG/PAX8 rearrangement (30-40% of the cases), resulting to be mutual exclusive with RAS mutations (Nikiforova, Lynch, et al. 2003). These tumors present at young age and are characterized by small size and occasional vascular invasion (Marques et al. 2004). Generally, they present a favorable prognosis (Nikiforova et al. 2002).

PDTC and ATC shows a huge variety of genetic alterations, part of them depends from the originating differentiated TC (Clark et al. 2016). RAS mutations has high prevalence over any other genetic modification, correlating with presence of distant metastases and recurrence (Hara et al. 1994). The PTC dedifferentiation and prognosis are mostly related to the accumulation of secondary alterations as TP53, PIK3CA and AKT1 (Penna et al. 2016). TERT mutation correlates with advanced stages of follicular cells-derived TC, it is related to presence of metastases and high mortality (Penna et al. 2016).

In MTC RET proto-oncogene mutations are predominant both in the hereditary forms (see paragraph 1.1.2) and sporadic forms (40-60% of the cases) (Lloyd et al. 2017).

1.1.2 Internal factors for thyroid cancer

Thyroid cancer occurs more frequently in women, representing three-quarters of the cases (Siegel, Miller, and Jemal 2015). An involvement of reproductive and hormonal factors was hypothesized since the gender disparity increases from the time of puberty and decrease after menopause, but further studies led to inconclusive evidences showing weak or equivocal association (Rahbari, Zhang, and Kebebew 2010; Peterson, De, and Nuttall 2012). Genetic susceptibility is proved as a risk factor for MTC (about 30% of the cases). The heritable MTC syndrome, known as multiple endocrine neoplasia type 2 (MEN2), is due to germinal mutations in the RET gene (Lloyd et al. 2017; Liska et al. 2005). Inherited predisposition has been highlighted also for PTC for pathologies like the familial adenomatous polyposis, the Werner syndrome and the Corney complex (Pal et al. 2001; Clark et al. 2016).

1.1.3 External factors for thyroid cancer

Exposure to ionizing radiation is reported to induce DNA damages, directly or by generating reactive oxygen species. These damages include single or double strand breaks resulting in deletions and chromosomal rearrangements (Williams 2008). Studies revealed that the exposure to ionizing radiation is the main environmental cause for the increase of PTC and, in minor extent, of FTC incidence, especially during the early childhood and also in the context of medical therapies (Neta et al. 2013; Nikiforov 2006). RET/PTC and AKAP9/BRAF rearrangements, typical for PTC, has been associated to radiation exposure (Nikiforova, Kimura, et al. 2003; Rabes et al. 2000). The relation between the exposure to radiations and RET gene modifications was further confirmed in studies on the population of Chernobyl (Kondo, Ezzat, and Asa 2006).

The daily iodine intake is considered one of the possible dietary factors that influence TC incidence. Studies demonstrated that in regions of iodine insufficiency the reduced iodine intake lead to an increment of FTC incidence reaching the 40% among all the TC cases (Dal Maso et al. 2009). In contrast, the adoption of a strategy of iodine supplementation is paired to an increase of PTC incidence (Blomberg et al. 2012).

Other risk factors still under investigation are smoking, obesity, diabetes, height and different thyroid pathological conditions (Dal Maso et al. 2009; Lloyd et al. 2017).

1.2 Thyroid cancer diagnosis: state of the art

1.2.1 Thyroid nodules

The ATA defines the thyroid nodules as “discrete lesions within the thyroid gland, radiologically distinct from surrounding parenchyma” (Cooper et al. 2006), this is a wide and general definition that includes both benign and malignant lesions. Thyroid nodules are very common entities, they are usually detected by palpation during physical examination of patients already presenting symptoms as pain and swollen of the thyroid. They can be found also incidentally by ultrasound (US) screening or radiographic studies using computed tomography (CT), as well as by magnetic resonance imaging (MRI). In the latter cases they are referred as “incidentalomas” (Tan and Gharib 1997).

The reported prevalence of thyroid nodules in countries with a sufficient iodine dietary intake is around 4%, while an increased value, around 10%, is reported for areas with a relative iodine deficiency (Pinchera et al. 1996; Reiners et al. 2004). Nodules are more common in women (Mazzaferri 1993) and there is an occurrence of multiple nodules (multinodularity) in more than one third of the cases (Tan and Gharib 1997).

The estimated overall population prevalence of thyroid nodules by palpation is around 4-7%. This value extremely increases, ranging from 30 to 76%, if the estimation is made considering the ultrasound-detectable nodules. These data are confirmed by studies performed via surgery at autopsy, detecting one or more nodules in 50-65% non-pathological thyroid examined, indicating that most of the cases remain undiagnosed during the patient’s lifetime (Tan and Gharib 1997; Mortensen, Woolner, and Bennett 1955; Mazzaferri 1993).

Presence of nodularities, palpable or detected via US, is the first symptom of TC. However, *per se*, it is not indicative of a medical condition, since the occurrence of malignancy is relatively rare and benign nodules usually don’t need to be treated (Gharib et al. 2010a). After the detection and the physiological estimation of the nodule via US, the cancer risk is normally evaluated via thyrotropin (THS) serum level determination and fine-needle aspiration (FNAB)

followed by cytology or immunohistochemistry (IHC), as shown in the algorithm in Figure 2. Other tools used to predict the malignant potential include magnetic resonance imaging (MRI), computed tomography (CT) and ^{18}F-fluorodeoxyglucose ([^{18}F]FDG) PET.

After the diagnosis, patients with malignant or suspicious lesions usually undergo surgery with total or partial thyroidectomy or radioiodine therapy in case of hyperfunctioning. Patients with benign or small lesions are monitored via clinical follow up, repeating an FNAB in case of a 50% increase in the lesion volume. In case of compressive symptoms or toxic nodular diseases, benign thyroid nodules can be treated via radioiodine (^{131}I) therapy, percutaneous ethanol injections or surgery (Popoveniuc and Jonklaas 2012).

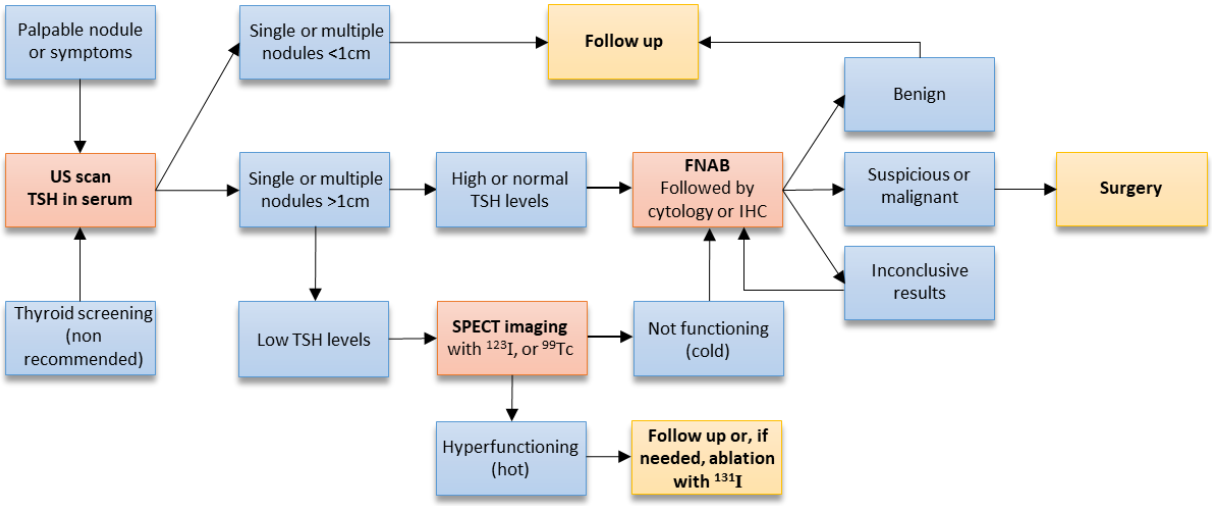

Figure 2. Simplified algorithm for the evaluation of a patient with possible malignant thyroid nodules.

The prevalence of malignancy, among diagnosed thyroid nodules, is lower than 5% (Hegedus 2004; Tan and Gharib 1997), resulting in big amount of efforts and costs to spot a relatively small number of TCs. The detection is limited also by the lack of specificity of the imaging techniques, such as ultrasound and SPECT, that can provide only anatomical and unspecific physiological information, and to the high number of inconclusive results obtained by FNAB, making the finding of TC, in certain cases, hard as “find the needle in the haystack” (Boelaert and McCabe 2011).

The complicated diagnosis of TC leads often to diagnostic surgery and overtreatment of thyroid. Already in the late ‘80s, reports on patients undergone to thyroid surgery highlighted the problem, demonstrating that excised nodules were malignant only in the 5-6.5% of the

cases, even with the benefit of biopsy (Werk et al. 1984; Belfiore et al. 1989). The recent use of panels of gene mutations and molecular markers, and the improvement in preoperative diagnosis only slightly reduced unnecessary surgery, that is still a consistent part of the total operations (Boelaert and McCabe 2011; Frates et al. 2006) with the consequence of live-long thyroid hormone replacement therapy (Jegerlehner et al. 2017).

1.2.2 TSH as a serum marker

The thyroid-stimulating hormone (TSH) is produced by the pituitary gland and has as primary biological function the promotion of thyroxine and triiodothyronine synthesis in the thyroid.

A negative feedback mechanism permits the regulation of TSH production and its release in blood flow in case of thyroid hormones imbalance. For this reason, the determination of serum TSH has a diagnostic valence for all the disease causing a thyroid dysfunction.

Higher serum TSH levels have been associated with an increased malignancy risk in patients with thyroid nodules (Boelaert et al. 2006), and an involvement in the TC progression have been suggested but not proved (Haymart et al. 2009). Low serum TSH levels can indicate presence of malignancy when occur together with a hypofunctioning thyroid (Popoveniuc and Jonklaas 2012). For these reasons, ATA recommends the measurement of serum TSH as a part of the first evaluation of patients bearing thyroid nodule >1 cm.

1.2.3 Use and limitations of ultrasound scan and elastography

Since four decades, ultrasonography constitutes an important part of the routine diagnosis of thyroid diseases, being preferred for its non-invasivity and reduced costs compared with any other diagnostic tool. With this technique, it is possible to accurately detect nonpalpable and subclinical nodules, estimate the size and volume, and differentiate cysts from solid nodules. It is also used, in couple with other techniques, for diagnostic (e.g. as a guidance for FNAB) or therapeutic procedures (Marqusee et al. 2000).

Some suspicious features can be identified via ultrasound exam (US) and considered for an evaluation of the malignancy risk. Among these, the highest specificities were found for microcalcifications (86-95%), irregular margins (83-85%), hypoechogenicity (43.4%) and

increased vascularity (49-81%) (Gharib and Papini 2007). The positive predictive value of these risk factors for malignancy is, unfortunately, reduced due to low sensitivity. However, it needs to be considered that the finding of these features alone is not sufficient to discriminate benign and malignant nodules (Papini 2003). Other recognized risk factors are elliptical shape and extracapsular growth (Gharib and Papini 2007).

If on one hand the use of high frequencies transducers can detect nodules smaller than 3 mm, on the other hand it was demonstrated that the prevalence of cancers in palpable nodules and in incidentalomas detected via US are the same (Gharib 1994). For these reasons an accurate diagnostic exam is suggested only for nodules with a size ≥1cm and an US screening for thyroid nodules is not recommended for the general population (Musholt et al. 2011).

Ultrasound elastography (USE) is an innovative tool that can assess the hardness of a tissue based on the distortion of US signal under the application of an external force. Despite different studies showed that this technique is highly specific and sensitive in the determination of certain malignancies (Rago et al. 2010), nevertheless it can't differentiate nodules with a calcified shell or blurred margins, like follicular carcinomas versus follicular adenomas (Rago and Vitti 2008). The use of USE is limited to high-end US instruments, this reduces the cost-effectiveness of the methodology.

1.2.4 Fine-needle aspiration biopsy (FNAB)

The FNAB is a safe and inexpensive procedure, characterized by an elevate accuracy, chosen as technique of election for the diagnosis of thyroid nodules. It represents, nowadays, the most reliable tool for determination and characterization of TC.

ATA recommends the use of FNAB on thyroid nodules in case of hypoechoic nodules bigger than 1cm size with suspicious features as irregular margins, intranodular vascularity or microcalcifications (Haugen et al. 2016).

The procedure is considered minimally invasive and is performed without local anesthesia. A 10ml syringe equipped with a 23- or 25-gauge needle is used, and the needle inserted into the nodule with the help of a syringe holder. The position of the needle is checked via palpation or more often via US-assistance, for difficult-to-palpate and nonpalpable nodules, while the

patient is in a supine position with the neck flexed backward. After the suction is released, the aspirated material is stained immediately for the cytological or histological evaluation. To decrease the false-negative results it is possible to repeat this operation multiple times (Hamburger and Hamburger 1986), depending on the characteristics of the thyroid nodule and the operator's preference (Kim et al. 2008).

Limitations of FNAB are well documented in the scientific literature and depend on different factors. In some cases, the limiting factor is represented by inadequate sampling, occurring especially in multinodular goiters, when the operation must be repeated several times for each nodule. In other cases, limitations are represented by the difficulty to distinguish morphologically between cancers and adenomas, or by the overlapping of benign and malignant features (Baloch institutional 1998). For these reason uncertain outcomes in thyroid nodules diagnosis are very common. Indeterminate cytology results, that are found in about 20% of patients (Gharib and Goellner 1993), normally require a second sampling that anyway give an indeterminate outcome in one third of cases (Goellner et al. 1987; Ziemianska, Kopczynski, and Kowalska 2016). Studies demonstrate that, indeterminate cytology is often due to the presence of cystic fluids or blood in the lesion. US-guided FNAB showed to drastically decrease nondiagnostic results (Danese et al. 1998). Suspicious results represent another limitation of FNAB, occurring in about 20% of the cases, and among these the majority usually undergo surgery. Histological examination of the excised thyroid shows that only around 25% of suspicious cases are malignant (Papini et al. 2002; Bartolazzi et al. 2001).

Despite the efforts to improve the preoperative diagnosis, FNAB is still leading to ~80% of unnecessary surgery, that cause high psychological and social costs (Boelaert and McCabe 2011; Frates et al. 2006).

1.2.5 Role of NIS as marker of thyroid misfunctioning

At the beginning of the 20th century, several studies investigated thyroid and its functionality, demonstrating the accumulation of iodine in the gland for the production of hormones (Marine 1915; Kendall 1915). The mechanism of iodine incorporation involves the transmembrane

glycoprotein sodium-iodide symporter (NIS) that actively transport one iodine anion every two sodium cations (Dohan et al. 2003).

NIS expression can be reduced or lost as a result of thyroid clinical conditions or cancer cells dedifferentiation, dropping the accumulation of iodine (Xing et al. 2005). It has been demonstrated that the presence of the BRAF gene mutation BRAFV600E reduces significantly the NIS expression (Chakravarty et al. 2011). For these reasons, the study of the distribution of radioiodine (a generic name that is referred to iodine radioactive isotopes) in the patient body can discriminate hypofunctioning nodules (cold), from normal (warm) and hyperfunctioning (hot) ones (see paragraph 1.2.6). Despite this, the radioiodine scan is not considered diagnostic for thyroid nodule evaluation, since even warm and hot nodules revealed to be malignant in the 10% and 5% of cases respectively (Gharib et al. 2010a; Gharib et al. 1984), while the risk of cancer among cold lesions reaches 15%. A sensitivity between 89% and 93% for diagnosis of thyroid cancer with this technique has been estimated, but a specificity of only 5% and a positive predictive value of 10% (Gharib and Papini 2007; Cases and Surks 2000).

1.2.6 Thyroid scintigraphy and SPECT

During the 1930s, as soon as the technology to produce artificial radionuclides was available, an increasing interest in the use of as radiotracer led to the discovery of the long half-life isotope ^{131}I and its diagnostic use in thyroid, taking advantage of the NIS-mediated uptake (Seidlin, Marinelli, and Oshry 1946). Later, scientist as Saul Hertz (1905-1950) and Arthur Roberts (1912-2004) started to study thyroid physiology and to treat thyroid diseases with ^{131}I on human patients (Sawin and Becker 1997). Following studies demonstrated that other chemical specimens can be trapped by the thyroid, as pertechnetate, in use in nuclear imaging as [^{99m}Tc]-pertechnetate (Wolff 1964).

Radionuclide thyroid imaging was originally performed with a rectilinear scanner map that gave an exact bi-dimensional reproduction of the thyroid, facilitating the localization of palpable anomalies. With the advent of gamma camera, and the consecutive development of scintigraphy, a better resolution led to the detection of nonpalpable lesions with a size about

1-2 cm for the first time (Freitas et al. 1985). In the 1980s the diffusion of the single photon emission computed tomography (SPECT), consisting of a gamma camera able to rotate around the patient to take images at multiple positions and a following computer-assisted reconstruction for 3D imaging, removed the limitations due to superimposition artifacts and allowed accurate volume measurements and anatomic localization (Chen et al. 1988).

Nowadays the radionuclide scan of thyroid is the most important diagnostic tool for thyroid disorders when FNAB is unavailable and represents the only technique suitable for the evaluation of the functional status of the thyroid. The tracers that showed best results are listed in Table 2.

Table 2. *Radiopharmaceuticals used in TC diagnosis via scintigraphy and SPECT.*

Tracer (emission)	Half-life	Rad/MBq in thyroid	Dose used for imaging (MBq)	Limitations	Ref
^{131}I (β,γ)	8.05 d	21.81	1.1-1.9	- NIS-mediated uptake - High absorbed radiation dose due to β emission	1
^{123}I (γ)	13.3 h	0.214	5.6-14.8	- NIS-mediated uptake - More expensive than other iodine isotopes	1
^{125}I (γ)	60 d	15.89	1.1-1.9	- NIS-mediated uptake - Low energetic emission interval - Long half-life	1
[^{99m}Tc]-pertechnate (γ)	6 h	0.004	185-370	- NIS-mediated uptake - Not organified by the thyroid, then not suitable for functional imaging	2
^{201}Tl (γ)	73 h	0.08	74-111	- Uptake revealed also in cases of adenomas and thyroiditis - Elevate sensitivity only in association with radioiodine scan	3
[^{99m}Tc]-sestaMIBI (γ)	6 h	0.0005	185-740	- Suitable only for MTC - Elevate sensitivity only in combination with FNAB and ^{99m}Tc-pertechnate scan	4

References: 1 (Gottschalk 1988), 2 (Powsner and Powsner 2006), 3 (el-Desouki 1991), 4 (Nakahara and Sagawa 1996).

Radioactive isotopes of iodine are the only known agents that can be incorporated by thyrocytes and afterwards organified, allowing an assessment on the physiological status of the thyroid gland. To reach the maximum peak of organification, radioiodine requires to be orally administered 24 hours before the scan. For this reason, an isotope of iodine with a low

photon energy and 10-20 hours half-life ($t_{1/2}$) is preferred to ^{131}I. Among more than 20 known iodine isotopes, ^{123}I appears to be the ideal radioiodine species ($t_{1/2}$=13.2 h, photon energy 159 keV), and it currently is the most used radionuclide for thyroid functional assessment.
Differently from iodine, [^{99m}Tc]-pertechnetate is not organified by thyroid but only trapped. This does not allow functional studies of the nodule and it can lead to a discordance with the results obtained via radioiodine imaging (Freitas et al. 1985; Turner and Spencer 1976).
Due to the low specificity of NIS as TC marker (see paragraph 1.2.5), thyroid scintigraphy or SPECT with radioiodine is recommended only in a limited number of cases, in particular for patients with low THS concentration, to evaluate the possibility of a toxic nodule (Musholt et al. 2011). Only in those cases, patients with hot nodules don't undergo surgery because of a negligible cancer risk (Mazzaferri 1993). The diagnostic specificity of radioiodine scan is further decreased for lesions smaller than 1 cm, which may not be identified by scan (Gharib and Papini 2007).
Tracers as ^{201}Tl and [^{99m}Tc]-sestamethoxyisobuthilisonitrile ([^{99m}Tc]-sestaMIBI), that present a fast turnover, revealed to be retained in tumors, their uptake in thyroid nodules is not mediated by NIS transport and demonstrated to improve the prediction of malignancy (Maublant et al. 1993). ^{201}Tl is quickly accumulated in well-perfused thyroid lesions, for this reason it is used to image thyroid nodules that results negative to radioiodine and [^{99m}Tc]-pertechnate in patients with increased serum thyroglobulin. Whereas, benign nodules tend to lose tracer faster, while most malignant tumors retained thallium (Ochi et al. 1982). [^{99m}Tc]-sestaMIBI accumulates within mitochondria in tumors as consequence of the inner membrane polarization, due to the acceleration of the respiratory chain reaction. Among TCs this phenomenon occurs only in MTC. A differential diagnosis is, then, possible only after FNAB and radioiodine scan (Learoyd et al. 1997; Sathekge et al. 2001).

1.2.7 Thyroid cancer overdiagnosis

In the last decades, the introduction of new diagnostic technologies and the progresses in the existent ones, combined with the development in the medical surveillance and screening, has enormously improved the detection of thyroid suspicious lesions, making possible the detection

of asymptomatic malignances and tumors of <1cm in size, e.g. micropapillary thyroid cancer (MPTC). The greatest impact on TC diagnosis has been provided by the advent of the medical neck ultrasonography in combination with the FNAB.

Recently, many authors have highlighted how overdiagnosis plays a major role in the constant increase of TC cases, referring to a “thyroid cancer epidemic of overdiagnosis” (Roman, Morris, and Davies 2017; Kitahara and Sosa 2016; La Vecchia et al. 2015; Vaccarella et al. 2016). Data from different studies support this idea, demonstrating how the increasing of TC cases is referred to the most common histologic type, PTC, represented by tumors with size <2.0 cm (MPTC contributes for ~50% of the overall increase). Conversely, the incidence of mortality associated to PTC has shown to remain stable or to decrease, given the frequently benign course (Enewold et al. 2009; Davies and Welch 2006; Pazaitou-Panayiotou, Capezzone, and Pacini 2007). A study from the International Agency for Research on Cancer (IARC) has estimated the changing of TC incidence after the introduction of neck ultrasound in the surveillance, concluding that this accounts for more than 60% of TC diagnoses in USA, Italy, Korea, France and Australia (Vaccarella et al. 2015). However, with a deeper view on all the possible causes, the extent of the overdiagnosis role is still debated (Wartofsky 2010; Liu, Su, and Xiao 2017).

Since 2015, new guidelines have introduced different recommendations to reduce the overdiagnosis of low risk thyroid cancer (Gharib et al. 2010b). The practice of thyroid cancer screening in asymptomatic patients is now strongly discouraged, whereas patients with MPTC and other very low risk TC or concurrent severe diseases are suggested to be managed by an approach of “active surveillance” (Bibbins-Domingo et al. 2017; Haugen et al. 2016). The criteria for the use of FNAB were revised by the American Thyroid Association (ATA), indicating that nodules of <1cm in size should not be biopsied except when family history of MTC or exposure to radiations is known. Furthermore, some thyroid neoplasms previously classified as malignant are now designed as benign after the reconsideration of adverse clinical outcomes and biological characteristics (Nikiforov et al. 2016).

Lack of specificity and limitations of the most common TC diagnostic techniques are discussed further in this dissertation. It is notable, that the diagnostic criteria are still mostly based on the size of the nodules, leading to a delayed diagnosis of the aggressive ATCs that present a rapid progression.

However, the problem of thyroid diagnosis is wider than the solely overdiagnosis issue. The discussion can't be pursued further without taking into account the high prevalence of benign thyroid nodules, with similar features as TCs, that makes challenging the detection of malignancies.

1.3 Use of PET imaging for thyroid cancer diagnosis

1.3.1 PET imaging

The positron emission tomography (PET), invented in the early 1960s by David Kuhl, is a non-invasive imaging technique capable of measuring the concentration of a positron-emitter radiotracer in the tissues (Semmler and Schwaiger 1997).

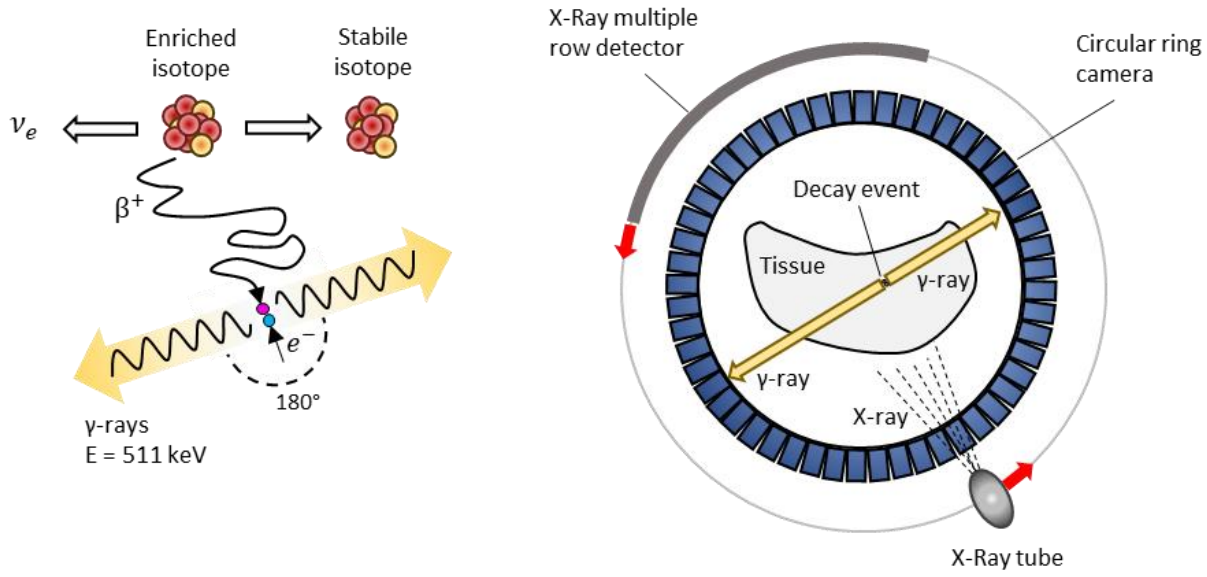

Figure 3. Basic principles of PET and PET/CT instrument.

Representation of the beta plus (β^+) decay (left) to a stable isotope of a proton enriched radionuclide with mass number A and atomic number Z, following the formula ${}^{A}_{Z}E \rightarrow {}^{A}_{Z-1}X + \nu_e + \beta^+$, where ν_e indicates the emission of an electron neutrino and β^+ the emission a positron.

The positron, after scattering off nuclei and electrons for approximately 10^{-10} seconds, annihilate with an atomic electron generating collinear gamma-rays.
Simplified scheme of the PET/CT detection system (right), formed by a circular ring camera for the detection of the collinear gamma-rays and a CT device formed by a rotating X-ray emitter and a detector on the opposite side.

The basic for PET functioning is represented in Figure 3. A PET-suitable proton-enriched isotope decays releasing a positron, the antiparticle of an electron, which scatters in the tissues until the mutual annihilation with an atomic electron. The annihilation produces two collinear divergent gamma-ray with energy of 511 KeV each, which can be registered by a detector with ring geometry and the position of the event reconstructed. In the light of this, the coupling with CT, based on the detection of single attenuated X-rays, is technically feasible and allows the possibility to recorder information about the morphology of the tissues in which the decay occurred.

PET displays sensitivity and specificity several order of magnitude higher than other nuclear medicine techniques. This make the investigative procedure ideal for *in vivo* tracer studies at picomolar levels (Jones 1996) and well suited for the investigation of cellular and molecular events in diagnostic, as well as during and after therapies. Limitations to resolution are due to the scattering of the positron before annihilation, depending on: i) the positron endpoint energy (an intrinsic characteristic of the radioisotope), ii) the chemical structure of tissues, iii) the diameter of the ring detector, that affects the possibility to register annihilation radiation when the angle between gamma-rays slightly differs from 180° (noncollinearity).

PET finds an application in the medical imaging field since the 1980s, with significant advances after the 1990s along with the idea of coupling PET with computed tomography (CT) (Townsend 2008). Nowadays, all the sold PET machines are integrated PET/CT scanners and they are typically used in oncological clinical imaging and investigation. Currently, oncologic PET/CT scans are largely operated injecting [^{18}F]-fluorodeoxyglucose ([^{18}F]-FDG), a radio-fluorinated derivative of glucose, playing a fundamental role in guided biopsies, hypermetabolic lesions ablation, assessment of the radiotherapy success, staging of FDG-avid lesions and surgical planning (Cazzato et al. 2018; El-Galaly, Gormsen, and Hutchings 2018). In a lesser

extent, PET/CT is used for the detection and diagnosis of neuroendocrine tumors using approved radiotracers that showed high specificity for these pathologies as the 3,4-dioxyphenylalanine derivative ^{18}F-DOPA and the somatostatin ligand ^{68}Ga-DOTATOC (Boy et al. 2018; Ambrosini et al. 2015). ^{18}F-cohline is an approved PET-radiotracer for the imaging of suspect prostate cancer or for follow-up procedures, while prostate-specific membrane antigen (PMSA) derivatives, as for example ^{68}Ga-PSMA-11, are not yet approved by international regulatory bodies (Glunde et al. 2015; Barbosa et al. 2018).

1.3.2 [^{18}F]-FDG PET/CT imaging of TC

The use of PET/CT in oncology makes possible the combination of the nuclear imaging high sensitivity with the spatial resolution of CT, but the quality of the results is linked to the pharmacokinetic characteristics and to the specificity of the designated tracer. Among the PET/CT tracers, [^{18}F]-FDG plays a key role in the oncology practice for many different cancers, due to the accelerated glucose metabolism in tumors (Warburg, Wind, and Negelein 1927).

Despite [^{18}F]-FDG is not a specific tracer for tumors, nevertheless it has a proven role in the diagnosis and monitoring of a large variety of metabolic diseases, inflammatory processes and infections.

The massive use of [^{18}F]-FDG-PET/CT scan for whole body imaging in clinical practice raised the interest on the incidental FDG uptake in the thyroid, which shows a prevalence around 2-3%. In the light of this, over the last years efforts have been made to set an algorithm for the workup of FDG-detected incidentalomas (Nilsson et al. 2011). In fact, unlike other organs in the head and neck region, as brain, eyes, tonsils and salivary glands, there is no specific uptake in thyroid gland (Nakamoto et al. 2005). This allows the distinction of FDG uptake areas that usually falls in two patterns: on one hand a diffuse signal, that is more frequent and usually benign, on the other hand a focal signal, that presents 30% to 50% chance of being cancer, mostly due to primary cancer and in rare cases to metastases (Chen et al. 2007; Mosci and

Iagaru 2011). However, well-differentiated TCs has often shown a deficiency of [^{18}F]-FDG uptake, usually paired to a retained ability to trap iodine (Feine 1998).

Due to the lack of specificity, [^{18}F]-FDG PET/CT has a minor role in TC diagnosis and management of patients. Its use is limited to the imaging of undifferentiated nodules that do not present iodine uptake, detection of distant metastases, pre-surgical evaluations (as calculation of tumor volumes and identification of surgical resectable sites) and the assessment of post-therapy changes (Mosci and Iagaru 2011; Fletcher et al. 2008).

In selected cases of undifferentiated and differentiated TC, a direct impact on the clinical management and patient outcomes was observed (Bogsrud et al. 2008; Wang et al. 1999).

1.3.3 Other tracers for PET/CT imaging of TC

With the exception of the [^{18}F]-FDG-mediated imaging, the use of PET/CT in thyroid oncology is still marginal, and a very little effort and consideration is given to the validation of novel radiotracer for the use of PET in diagnosis. Despite the fact that PET is largely considered more sensitive than scintigraphy and SPECT, the higher costs, not compensated with studies on tracers suitable for other tumors than DTC and MTC, discourage further progresses in PET/CT diagnostic imaging (Townsend 2008). The most promising PET/CT tracers for TC imaging are listed in Table 3.

Table 3. Radiotracers used in TC diagnosis via PET/CT.

Tracer	Half-life	Target	Limitations	Ref.
^{124}I	4.18 d	NIS	- No discrimination between malignant and benign nodules - High costs - Long half-life	1
[^{18}F]-TFB	109.8 min	NIS	- No discrimination between malignant and benignant nodules	2
^{68}Ga-DOTATOC; ^{68}Ga-DOTALAN; ^{68}Ga-DOTATATE	67.8 min	Somatostatin receptors	- Specificity limited to MTC and DTC - No significant advantages if compared with [^{18}F]-FDG	3, 4
^{18}F-DOPA	109.8 min	-	- Specificity limited to MTC - Lack of studies on the accumulation mechanism	5
68Ga-HBED-CC-PSMA	67.8 min	PSMA	- Specificity limited to MTC and DTC - No significant advantages if compared with [^{18}F]-FDG	6

References: 1 (Eschmann et al. 2002), 2 (Anbar, Guttmann, and Lewitus 1960), 3 (Middendorp et al. 2010), 4 (Traub-Weidinger et al. 2015), 5 (Caobelli et al. 2018), 6 (Lutje, Cohnen, et al. 2017).

^{124}I is the most common PET tracer for thyroid imaging, used as a PET-suitable surrogate of ^{123}I due to its decay, consisting in a 22% of positron emission, and its half-life of 4.18 days, appropriate for organification studies (Eschmann et al. 2002). The comparison in the oncological field with the SPECT radiotracers ^{123}I and ^{131}I showed a diagnostic concordance rate up to 97% and an enhanced detection of residual and metastatic tumor foci (Ruhlmann et al. 2016; Van Nostrand et al. 2010). However, this radiotracer suffers from the same limitations of radioiodine, in fact, the use of ^{124}I is restricted to the detection and surgery planning of metastases derived from tumors that maintained the expression of NIS (Santhanam, Solnes, and Rowe 2017). Even when compared with [^{18}F]-FDG-PET/CT, no technical or clinical advantages are demonstrated so far (Pentlow et al. 1991; Buscombe 2007).

Tetrafluoroborate (TFB) is a fluorinated ion that interacts with NIS being accumulated in cells and inhibiting the uptake of iodine (Anbar, Guttmann, and Lewitus 1960). Its radiofluorinated equivalent, [^{18}F]-TFB, act as an analogous of radioiodine in PET imaging, showing equivalent performances in mice and non-human primates (Marti-Climent et al. 2015; Khoshnevisan et al. 2016). It is characterized by faster uptake and clearance in comparison to ^{124}I, this encourage a translation to phase 2 trials (O'Doherty et al. 2017). Nevertheless, exactly as ^{124}I, the use of this tracer is limited to diagnosis of DTC metastases in whole body scans.

Radiotracers direct to targets different than NIS were also studied. Somatostatin receptor subtypes and PMSA are demonstrated to be overexpressed in medullary and differentiated thyroid cancers and proposed as target for the evaluation of tumors with a decreased or absent NIS expression (Traub-Weidinger et al. 2015; Lutje, Gomez, et al. 2017). Somatostatin receptor antagonists labeled with positron emitters, as ^{68}Ga-DOTATOC (FDA approved), ^{68}Ga-DOTALAN and ^{68}Ga-DOTATATE, were successfully tested on patients, but possible advantages in comparison with [^{18}F]-FDG remain still under debate (Middendorp et al. 2010; Pisarek et al. 2009).

MTCs were found to accumulate 3,4-dihyroxyphenylalanine (DOPA) due to amino acid transporter overexpression, this opened the possibility to image this type of TC using the ^{18}F-

fluorinated derivative of DOPA (^{18}F-DOPA) (Kauhanen et al. 2009). The tracer revealed a direct correlation between malignancy and calcitonin levels (Caobelli et al. 2018) and a moderate higher sensitivity if compared with [^{18}F]-FDG, but reduced signal (Beuthien-Baumann et al. 2007; Marzola et al. 2010).

1.3.4 Immuno-PET imaging principles

The idea to combine the sensitivity and resolution of nuclear medicine diagnostic instruments with the specificity of antibody targeting, creating an indirect method for the *in vivo* visualization of organs or diseases, is not new in the field. Already in 1948 Pressman et al. demonstrated that radiolabeled polyclonal antibodies can be used to perform imaging on small animals via scintigraphy (Pressman and Keighley 1948). Afterwards, Bale et al. extended the procedure to human subjects, but the outcomes still presented low resolution (Bale, Contreras, and Grady 1980). Better results were reached with the use of the hybridoma technology to produce great quantities of highly selective IgG monoclonal antibodies (mAb) binding a single epitope on one antigen (Kohler and Milstein 1975; Goldenberg 1993; Herlyn et al. 1979).

IgG antibodies can be digested in smaller units by proteolytic enzymes (Figure 4): papain splits the heavy chain to form two fragment antigen binding (Fab) and one non-binding fragment crystalline (Fc), while pepsin removes the Fc fragment maintaining the Fab units together by the hinge region (Porter 1959; Nisonoff et al. 1960). Smaller antibody fragments have shown several advantages if compared with the full mAbs. They have a faster distribution and clearance from the vascular system, on the same time they can diffuse in the interstitial space more quickly, resulting in an enhanced tumor to background ratio (Jain 1990). The absence of a Fc region leads to less unspecific binding (since many cells present membrane receptors that bind the Fc region), easier purification by affinity, weaker immune response against the tracer and a reduced accumulation in liver. Nevertheless, modifications of the three-dimensional structure can change the immunoreactivity and the affinity of the binding site for the epitope. Moreover, the smaller dimension of the product reduces the availability of amino acidic residues for conjugation with a dye or a radionuclide ligand.

More recently, the era of genetic engineering combined with the use of the phage display technology, opened the possibility to molecular design and production of proteins. These new methods permitted the development of chimeric or humanized mAb or antibody fragments and, additionally, of a myriad of small antibody-based proteins as single chain antibodies, microantibodies, minibodies and several variants. These products showed a variety of different characteristics amplifying pro and cons of the antibody fragments use (Harmsen and De Haard 2007; Huston et al. 1988; Kennedy et al. 2018; Serafini 1993).

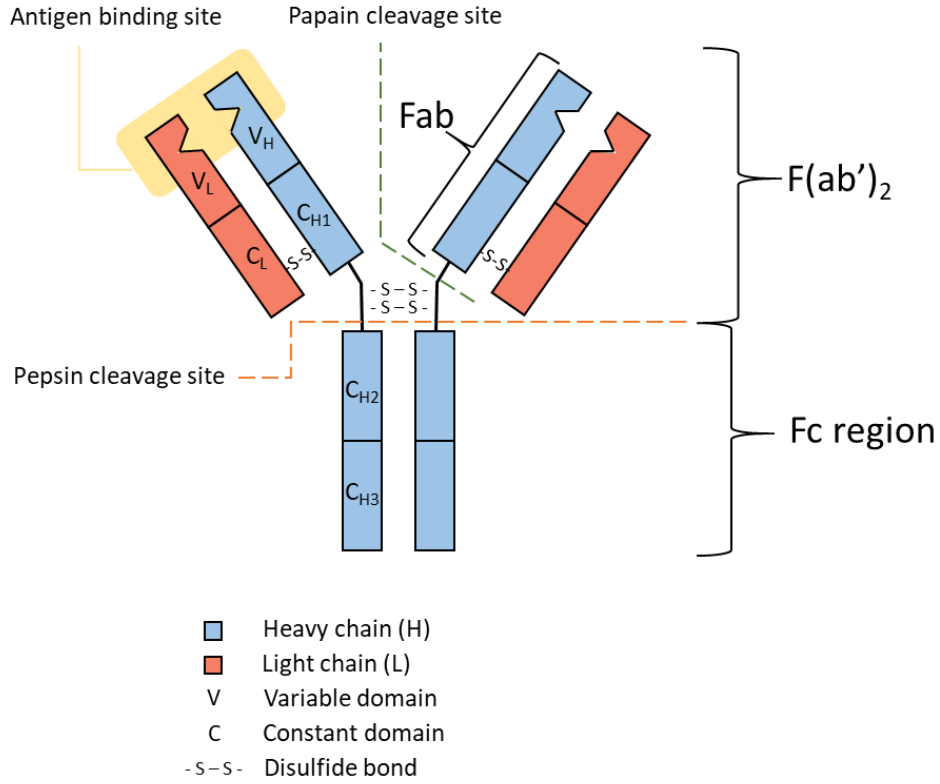

Figure 4. IgG antibody structure and cleavage sites.

In the last decades, the “come back” of the interest for “immunotargeting” in nuclear medicine imaging was due to the recent progresses in oncology and medical imaging. On one hand, there was a discovery of a huge quantity of specific tumor biomarkers candidates by oncogenic and transduction pathway studies. On the other hand, PET found an ample diffusion as technique with high sensitivity and resolution, combined with the high specificity of antibodies radiolabeled with β-emitters.

For the production of an antibody-based immuno-tracer for PET, the physical half-life of the chosen β-emitter radionuclide must match with the biological half-life of the antibody. The most common radionuclides for small antibody fragments and peptides characterized by a fast clearance are ^{18}F ($t_{1/2}$=110 min) and ^{68}Ga ($t_{1/2}$=68 min), while ^{89}Zr ($t_{1/2}$=78 h) and ^{124}I ($t_{1/2}$=100 h) match perfectly with the biological half-life of full antibodies and big antibody fragments ($F(ab')_2$). In addition, ^{64}Cu ($t_{1/2}$=13 h) can be used for a large number of molecules with different sizes.

^{18}F and ^{124}I can be integrated into the protein primary structure respectively via fluorination or iodination reactions, but consequent phenomena of internalization lead to cellular catabolism with unspecific retention and release in the surrounding tissues. This problem can be handled with the introduction of prosthetic groups (McBride et al. 2009; Kim et al. 2016).

The radiolabeling of a β-emitter metal to protein is possible by conjugation with a suitable bifunctional chelator directly to an amino acidic residue, for example forming a peptide bond with a lysine residue (primary amine), or it can be achieved using a linker, usually a polyethylene glycol chain (PEG), to avoid changes in the three-dimensional structure and guarantee a retained immunoreactivity. For ^{68}Ga and ^{64}Cu is indicated a bifunctional chelator as tetraxetan (DOTA) derivatives (Bailly et al. 2016), that has been shown to be suitable even for the chelation of ^{89}Zr (Pandya et al. 2017). The routinely exadentate ligand for ^{89}Zr is desferrioxamine (DFO), that is currently used in clinical practice for iron and aluminum poisoning, and chelates zirconium in mild conditions (Vugts and van Dongen 2011).

1.4 Galectin-3 as a thyroid cancer biomarker

1.4.1 Galectin-3 molecular functions and biological processes

Galectins are a class of proteins from the lectin family with the principal molecular function of bind β-galactoside sugars and their derivatives, they are found in humans, rat, mice and many other animal species (Kasai and Hirabayashi 1996).

Galectins tend to associate in polymers and are divided in three classes, depending from the structures they can form: i) dimeric galectins form homodimers, ii) tandem galectins form heterodimers, iii) chimeric galectins can form polymers with more than two dimers.

Galectin-3 (Gal3), with a molecular weight around 32 kDa, is the only chimeric galectin. It possesses a structure characterized by two domains:

- An amino-terminal (N-terminal) domain, that possesses a tandem repeats short amino acid segments (Pro–Gly–Ala–Tyr–Pro–Gly) which show tendency to self-associate in oligomers of up to five molecules (pentamers) (Lepur et al. 2012);
- A carboxylic-terminal characteristic carbohydrate-recognition domain (CRD), which characterizes the basic function of Gal3, and the recognition and binding of glycoproteins and glycolipids.

Gal3 is expressed throughout the body, especially in intestines, urogenital tract, lungs and heart with a considerably high expression in epithelial, endothelial, myeloid cells and fibroblasts (Le Marer 2000; Diaz-Alvarez and Ortega 2017). In the cells, it is expressed as cytoplasmic protein, but it also can traverse the intracellular membranes and be located in the nucleoplasm and mitochondria. Gal3 can be also externalized, preferably via exosomal transport mechanism (Figure 5), then triggered by detachment-sensitive cell mechano-sensors, and consequently internalized via endosomes (Thery et al. 2001; Baptiste et al. 2007).

A great variety of Gal3 interaction partners have been found in all the compartments in which it is expressed. In the nucleus it binds RNA-associated proteins, acting as part of ribonucleoprotein complexes and as a pre-mRNA splicing factor (Wang et al. 1995) being then implicated in the cellular growth regulation, anti-apoptotic functions and mRNA splicing (Akahani et al. 1997; Dagher, Wang, and Patterson 1995). In the cytosol and on the membrane Gal3 interacts with proteins such Bcl-2, K-Ras, annexin VII, and cytokeratins playing an important role in the cell migration (Dumic, Dabelic, and Flogel 2006; Qi et al. 2014). In the extracellular milieu, Gal3 is associated to membrane proteins and extracellular proteins, as T-cells receptors, and components of the extracellular matrix, as laminin, fibronectin, vitronectin, N-CAM and integrin (Nangia-Makker et al. 2000; Hughes 2001). Here, it is involved in cell adhesion mechanisms, the control of the immunosuppression, modulating the T-cell activation (Peng et al. 2008), immunity against pathogens as *Candida albicans*, acute or chronic

inflammation and pathogenesis of diabetic complications (Goetz et al. 2008; Diaz-Alvarez and Ortega 2017; Pugliese et al. 2015; Kohatsu et al. 2006).

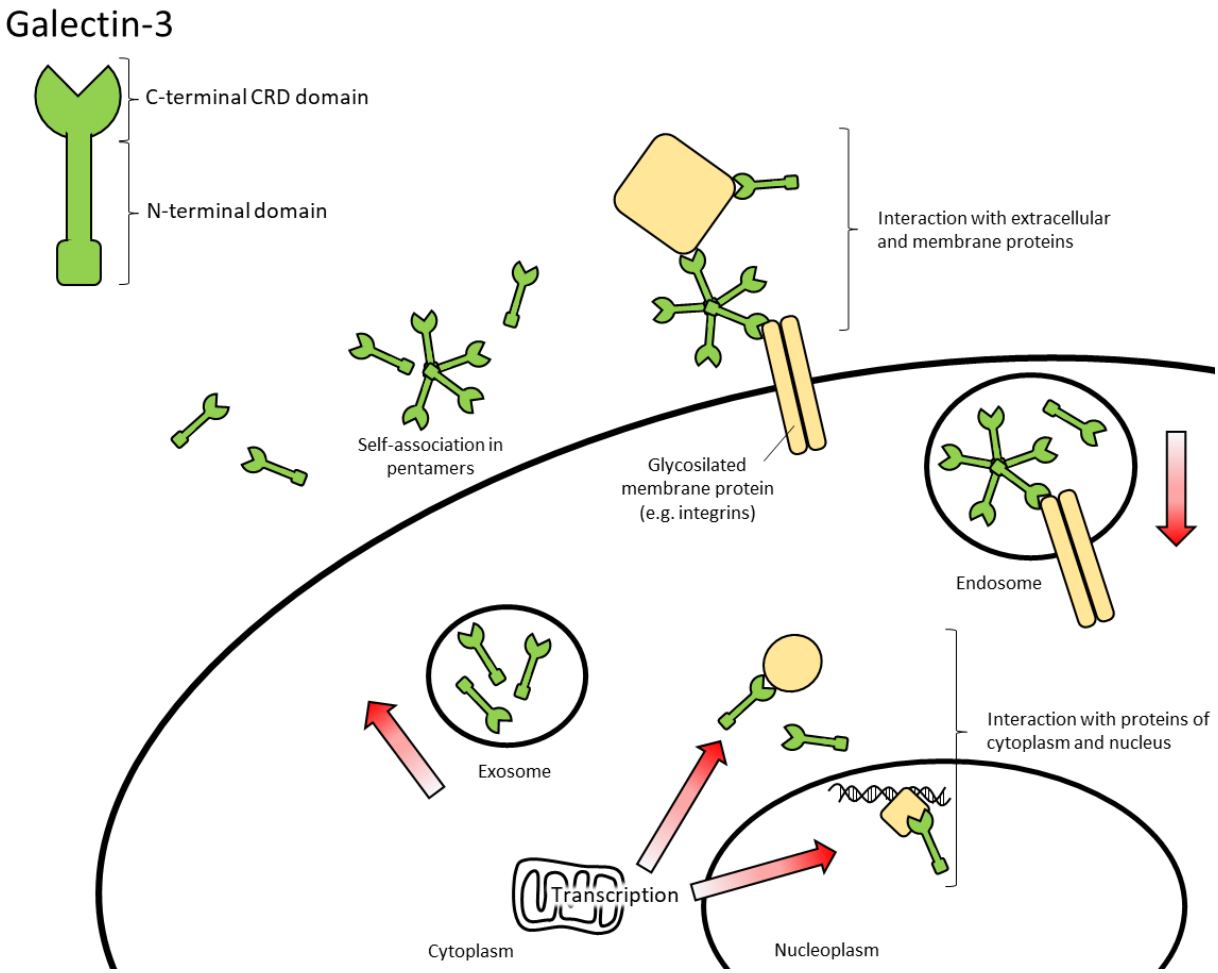

Figure 5. Schematic presentation of Gal3 localization and interactions.

The role of Gal3 as diagnostic prognostic biomarker as well as therapeutic target for a wide range of pathologies has been extensively treated in the last two decades (Sciacchitano et al. 2018). Molecular biological studies have proven that Gal3 contributes to the enhancement of different processes related with malignant transformation in several tissue and consecutive the development of aggressive treats. It interferes with the cysteine protease pathways, having an anti-apoptotic effect, and at the same time it activates K-ras, the most important RAS oncoprotein, that enhance MAPK activation promoting tumor transformation (Akahani et al. 1997; Elad-Sfadia et al. 2004). Gal3 has also a role in the development of metastases, due to its anti-anoikis properties, crucial for anchorage-independent cell survival (Nangia-Makker, Balan, and Raz 2012; Kim et al. 1999). Moreover, the Gal3 phosphorylation have been

demonstrate to promote tumorigenicity, modulating a variety of genes that may play a role in malignant transformation, anti-apoptotic functions, preventing p53-induced apoptosis and inducing cell cycle arrest (Mazurek et al. 2005; Cecchinelli et al. 2006; Yoshii et al. 2002). Due to its association to angiogenesis, Gal3 is involved in a further series of cell events related to tumor progression and metastatic processes (Fortuna-Costa et al. 2014; Goetz et al. 2008). Different studies reported evidences that its downregulation can suppress the tumorigenicity and induce apoptosis in cancer cells (Honjo et al. 2001; Nakahara, Oka, and Raz 2005).

1.4.2 Galectin-3 expression in thyroid cancer

The interest in funding a novel TC markers finds its roots in the need of an immunohistochemical method for the interpretation of indeterminate or suspicious thyroid nodule FNABs. In a review of 2003, Segev et al. individuated up to 12 different thyroid cancer markers that, in different extent, hold the promise as FNAB adjuncts for more precise outcomes, and wished for further studies on single and combined markers to present an exhaustive panel for diagnosis of suspicious thyroid lesions that can guarantee high sensitivity and specificity (Segev et al. 2003). Despite this, to the present days, no stand-alone specific thyroid tumor biomarkers are available to regularly and reliably distinguish benign from malignant thyroid tumors (Negro, Greco, and Colosimo 2017).

Among the possible markers, Gal3 has recently received significant attention. Its role in thyroid tumor has been extensively investigated since 1997, when it was first reported as a phenotypic feature of malignant thyroid neoplasms (Fernandez et al. 1997). Followings studies focalized on the relation between thyroid nodules and Gal3 discovering that in thyroid tissue the expression of Gal3 is exclusively restricted to malignant transformed epithelial thyroid cells. It has been demonstrated that the hypomethylation state of 5 CpG sites in the genome, that codifies for Gal-3, is highly associated with thyroid malignancies while a forced expression via Gal3 cDNA transfection have been proven to generate a transformed phenotype (Takenaka et al. 2003; Keller et al. 2013)

The role of Gal3 was extensively studied in DTC. Inhibition of Gal3 showed to improve the apoptotic activity and radiosensitivity, suggesting a use for therapeutic strategies (Lin et al.

2009). Shankar et al. in 2013 demonstrated that Gal3 acts in synergy with Caveolin-1 promoting focal adhesion, indicating that this protein is involved in migration and metastatic processes (Shankar et al. 2012). Studies involving mRNA expression analysis of DTC proved that the overexpression of Gal3, as well as Galectin-1, have a role in tumor progression (Salajegheh et al. 2014).

In 2001, a large study on histological material conducted by Bartolazzi et al. reported that 94% of the thyroid cancer types considered invariably express Gal3 with the exception of MTC, while only the 2% of the benign nodules were Gal3 positive, characterizing the Gal3 immunostaining as an adjunct to FNAB (Bartolazzi et al. 2001). Afterwards, several independent studies listed Gal3 in panels of biomarkers that can be used to improve the specificity and sensitivity of thyroid nodules FNAB. Wiseman et al. reported a wide panel taking in account the expression of Gal3 and six other markers, reaching a sensitivity of 88% and a specificity of 94%, while other research groups proposed panel sets made of three proteins, including fibronectin-1, HBME-1, hexokinase III and cyclin A, reporting specificities higher than 96% (Prasad et al. 2005; Hooft et al. 2008).

Gal3, with its overall sensitivity of 78% and specificity of 93%, is considered the most accurate standing alone marker for TC diagnosis validated in blind for the thyroid nodule characterization, capable to improve the diagnosis of TC helping with the discrimination between benign and malignant nodules (Bartolazzi, Orlandi, et al. 2008; Griffith et al. 2008).

The use of Gal3 expression analysis is, since 2006, taken in consideration by the ATA for the management of patients with thyroid nodules (Gharib et al. 2006), and nowadays strongly recommended for the clinical practice (Cooper et al. 2009; Gharib et al. 2016).

2 **AIM OF THE PROJECT**

Despite the use of a wide range of well-established techniques, the clinical criteria for the management of patient with suspicious thyroid nodules are still far from perfect. The decisional process about the possibility to perform nodular biopsies is mostly based on the size of the nodule, this leads to an excessive long follow-up period that can delay the diagnosis of aggressive forms of TC. On the other hand, when biopsies outcomes are uncertain, the patient usually goes through overtreatment (Rosato et al. 2004). In the light of this, a diagnostic imaging operated with a specific agent capable to discriminate and localize thyroid malignancies, characterizing clinically significant or insignificant tumors prior to surgery, would significantly diminish thyroid surgeries and reduce healthcare costs (Scott-Combes and Kinsman 2007). For this purpose, taking into account the importance of Gal3 as thyroid tumor marker, the use of the immuno-PET methodology for developing tracers targeting Gal3 for a pre-surgical non-invasive imaging might be the most sensible approach in terms of specificity and sensitivity. The possibility to image thyroid tumors expressing Gal3 *in vitro* and *in vivo* with this kind of tracer was already demonstrated by our group (D'Alessandria et al. 2016) using a radiolabeled full anti-Gal3 mAb, but a large uptake in liver and slow clearance from blood represent big limitations due to the use of a full mAb.

With the purpose of clinical translation and to achieve high imaging contrast, an essential step is represented by the production of a smaller immuno-tracer, reducing in this way the unspecific uptake in liver and increasing the clearance from blood. At the same time, the high affinity for Gal3 must be maintained to ensure a specific accumulation in the tumor, to this end any changing in the molecular structure must not (or only slightly) affect the antibody variable domain. For these reasons the tracer was designed starting from an anti-Gal3 $F(ab')_2$, produced via pepsin digestion from the anti-Gal3 rat mAb M3/38 from Mabtech (Inohara et al. 1999). The antibody fragment was conjugated with DFO and radiolabeled with ^{89}Zr, a positron emitter that possess a suitable physical half-life (Bailly et al. 2016; Holland et al. 2010; Meijs et al. 1997) for labeling full antibodies and their derived fragments ($F(ab')_2$, Fab', scFab). The

obtained radiotracer was deeply characterized *in vitro* for cell binding, immunoreactivity, internalization into thyroid tumor cells expressing Gal3 and stability.

For the further evaluation of our method and for a comparison with the radioiodine scan, that is considered the thyroid imaging golden standard (see paragraph 1.2.5), novel *in vitro* and *in vivo* models able to closely reproduce the structure of the tumor and environment of the original anatomical site in patients were developed. For *in vitro* tests the TC cells lines were grown as 3D cultures forming spheroids and aggregates, these structures are comparable to microtumors (diameter <1 cm) and were used to quantify and highlight differences in the protein and genetic expression of NIS and Gal3. Moreover, spheroids can in a good extent reproduce cell to cell interactions, conditions of distance from blood vessels microenvironment, diffusion and convection phenomena and metabolic profiles, resulting ideal for studies on the time-dependent penetration of the tracer of the probe in the inner layers (Minchinton and Tannock 2006; Zhou et al. 2013). The *in vivo* tests were performed on a clinically relevant mice models established via orthotropic implantation of TC cells in the thyroid left lobe, mimicking the pathological conditions of human patients and allowing the use of the healthy right thyroid lobe as internal control. The growth of the tumors was confirmed and monitored via ultrasound scan.

To validate our method in contrast to the unspecific routine diagnostic techniques for the thyroid nodules characterization, one group of animals underwent to PET/CT scan with ^{124}I, as an analogue of ^{123}I and ^{99m}Tc-pertechnetate NIS-dependent scintigraphy, while a second group received injection of a near infrared dye conjugate of the anti-Gal3 $F(ab')_2$ for fluorescence molecular tomography imaging and subsequently an injection of the developed radioimmunotracer followed by PET/CT scan. The PET results obtained with the routine and novel methods were compared and the reliability and predictability of immuno-PET outcomes were evaluated via anatomical inspection during necropsy and by correlation with biodistribution studies.

All the experiments were performed using three different TC cell lines, a PTC (BcPAP) and two ATCs (FRO82-1 and CAL62).

3 **MATERIALS**

3.1 Technical equipment

Table 4. *Technical equipment.*

INSTRUMENT	**COMPANY**
10 µl glass syringe	Hamilton Company, Reno, NV
AccuBlock Digital Dry Bath	Labnet International, Edison, NJ, USA
Analytical balance AC210S	Sartorius, Göttingen, Germany
Analytical balance SI-64	Denver Instrument, Göttingen, Germany
Aperio AT2 scanner	Leica Biosystems, Nussloch, Germany
Ball mill Micro-Dismembrator II	B. Braun, Melsungen, Germany
Biorevo BZ-9000	Keyence, Osaka, Giappone
BondMax RXm system	Leica, Wetzlar, Germany
CelloShaker Variospeed	Chemetron, Milan, Italy
Centrifuge Biofuge 13	Heraeus, Hanau, Germany
Centrifuge Fresco 21	Heraeus, Hanau, Germany
Centrifuge J2-HS	Beckman Coulter, Brea, USA
Centrifuge Megafuge 1.0R	Heraeus, Hanau, Germany
Countess Automated Cell Counter	Invitrogen, Carlsbad, CA, USA
CRC-25R Dose Calibrator	Capintec, Florham Park, NJ, USA
Casy counter	Schärfe, Seelow, Germany
Electrode N 5800 A	SI Analitics, Mainz, Germany
FACSCalibur Flow Cytometer	BD Biosciences, Franklin Lakes, NJ, USA
FMT2500 Imaging System	VisEn Medical Inc., Bedford, MA, USA
Freezer (-20°C)	Liebherr-International AG, Bulle, Switzerland
Freezer (-80°C)	Haier, Tsingtao, Cina
Gabi Radioactivity-HPLC-flow-monitor	Elysia-Raytest, Liège, Belgium
Gamma Counter 1480Wizard3	Wallac, PerkinElmer, Waltham, USA

Gamma Counter 2480Wizard2	PerkinElmer, Waltham, USA
GFL Shaking Water Bath 1092	GENEO Labstore, Lübeck, Germany
Gilson Pipette Pipetman Classic P2, P10, P20, P100, P200, P1000	Gilson, Middleton, Germany
Imaging plate scanner HDCR35 Bio	Dürr NDT, Bietigheim-Bissingen, Germany
Incubator Heracell 240i	Thermo Fischer Scientific, Waltham, USA
Incubator Hood TH 15	Edmund Bühler, Bodelshausen, Germany
Inveon small animal PET/CT scanner	Siemens, Knoxville, USA
Laminar Flow HB 2472	Heraeus Holding, Hanau, Germany
LC-20A Prominence HPLC system	Shimadzu, Kyōto, Japan
Magnet agitator	Janke & Kunkel, Staufen, Germany
Magnetic stirrer and heater RCT basic	IKA, Staufen im Breisgau, Germany
Magnetic Stirrer with Heater RH Basic 2	IKA, Staufen im Breisgau, Germany
Mastercycler Personal Thermal Cycler System	Eppendorf AG, Hamburg, Germany
Microplate reader EL800	Tecan, Männnedorf, Switzerland
Microscope Axiovert 10	Carl Zeiss Microscopy, Oberkochen, Germany
Microwave MW 7809	Severin, Sundern, Germany
Milli Q UF-Plus	Merck Millipore, Darmstadt, Germany
Mini-PROTEAN® Tetra cell system	Bio-Rad Laboratories, Hercules, USA
Mini-PROTEAN® Tetra Vertical Electrophoresis Cell	Bio-Rad Laboratories, Hercules, USA
Mini Trans-Blot® Blotting Cell	Bio-Rad Laboratories, Hercules, USA
MS550D Transducer	Visualsonics, Toronto, Ontario, Canada
MyFuge Mini	Benchmark Scientific, Sayreville, NJ, USA
NanoDrop ND-1000	VWR, Radnor, PA, USA

Nanophotometer	Implen GmbH, Munich, Germany
pH/Ionmeters S220 Seven Compact	Mettler Toledo, Schwerzenbach, Switzerland
Pipetus	Hirschmann, Eberstadt, Germany
Precision balance 440-35N	Denver Instrument, Göttingen, Germany
Radio-TLC-scanner	Eckert & Ziegler, Berlin, Germany
Repeater pipette 4780	Eppendorf AG, Hamburg, Germany
Rotary microtome HM 355S	Thermo Fischer Scientific, Waltham, USA
Rotator SB2	Stuart, Stone, UK
SE-HPLC BioSep™ (SEC-s3000 LC Column)	Phenomenex, Aschaffenburg, Germany
Shaking-hybridization oven OV3	Biometra, Göttingen, Germany
Sigma Delta Vaporizer	Penlon Limited, Abingdon, UK
Single-channel pipettes 0.1-2.5/2-20/ 20-100/100-1000µl	Eppendorf AG, Hamburg, Germany
Steam Sterilizer HV50	HMC Europe, Tüßling, Germany
StepOne Real-Time PCR System	Applied Biosystem, Life technologies, Waltham, MA, USA
Stereomicroscope Stemi DV4 Spot	Carl Zeiss, Oberkochen, Germany
Temperature control ETS-D4 fuzzy	IKA, Staufen im Breisgau, Germany
Thermomixer comfort	Eppendorf AG, Hamburg, Germany
Ultasound Vevo 2100 Imaging System	Visualsonics, Toronto, Ontario, Canada
Ultra Turrax Tube Drive Homogenator	IKA, Staufen im Breisgau, Germany
Ultrasonic Cleaner USC-TH	VWR, Radnor, PA, USA
Vortexer	Bender & Hobe, Switzerland
Vortexer 4 Basic	IKA, Staufen im Breisgau, Germany
Vortexer Vibrofix VF1	IKA, Staufen im Breisgau, Germany

Vortex-Genie 2	Scientific Industries, Bohemia, NY
X-Ray cassette	Rego X-ray GmbH, Augsburg, Germany
Yarra SEC-3000 Analytical Column	Phenomenex, Aschaffenburg, Germany

3.2 Consumables

Table 5. *Consumables.*

Consumable	**Company**
10% precast polyacrylamide MP TGX Gel 10W 30 µl	Bio-Rad Laboratories, Hercules, USA
50ml tubes	Corning Inc., Corning, NY, USA
50ml/15ml tubes	Greiner Bio-One, Frickenhausen, Germany
8-well chamber slide	Lab-tek
Amicon Ultra Centrifugal Filters 0.5ml: 100KDa, 50KDa, 30kDa	Merck Millipore, Darmstadt, Germany
Aspiration pipette (2ml)	Sarstedt, Nümbrecht, Germany
Cell culture F-Bottom well plates	TPP Techno Plastic products, Trasadingen, Switzerland
Cellstar Cell culture flask	Greiner Bio-One, Frickenhausen, Germany
Chromatography paper (iTLC-SA)	Varian, Lake Forest, CA
CL-XPosure Film	Waltham, MA, USA
Combitips 5/10ml	Eppendorf AG, Hamburg, Germany
Countless Cell counting slide	Invitrogen, Carlsbad, CA, USA
Cryotube vials	Nunc, Roskilde, Denmark
Disposal hypodermic needles 26G/30G	B. Braun, Melsungen, Germany
Filter tips (10µl, 200µl, 1000µl)	Sarstedt, Nümbrecht, Germany
Glass beads	IKA, Staufen im Breisgau, Germany
Gloves latex	Semperguard, Wien, Austria
Gloves nitrile	Sempermed, Wien, Austria

MColor pHast pH indicator strips	Merck Millipore, Darmstadt, Germany
MicroAmp Optical 96-Well Reaction Plate	Applied Biosystems, Foster City, CA, USA
MicroAmp Optical Adhesive Film	Applied Biosystems, Foster City, CA, USA
Mini TransBlot Filter Paper	Bio-Rad Laboratories, Hercules, USA
Object slides SuperFrost Plus	Thermo Fischer Scientific, Waltham, USA
Parafilm	Pechiney Plastic Packaging, Chicago, USA
PCR tubes	Eppendorf AG, Hamburg, Germany
Phosphor imaging plate	Fujifilm, Tokyo, Japan
Pipette tips (10µl, 200µl, 1000µl)	Sarstedt, Nümbrecht, Germany
Polystyrene V-bottom tubes	Sarstedt, Nümbrecht, Germany
Protein LoBind Tubes 0,5 and 1,5 ml	Eppendorf AG, Hamburg, Germany
PVDF Membrane	Merck Millipore, Darmstadt, Germany
Reaction tubes (1.5µl and 2ml)	Sarstedt, Nümbrecht, Germany
Scintillator vials 20 ml	Sarstedt, Nümbrecht, Germany
Sealing foil	Alpha laboratories, Hampshire, UK
Sephadex G-25 M, PD10 column	GE Healthcare, Buckinghamshire, UK
Sep-Pak Accell Plus QMA Plus Short Cartridge	Waters, Milford, MA, USA
Sep-Pak Alumina N Short Cartridge	Waters, Milford, MA, USA
Serological pipettes (2/5/10/25/50ml)	Sarstedt, Nümbrecht, Germany
Single-use syringes, Injekt-F 1ml and Injekt 20 ml	B. Braun, Melsungen, Germany
Stericup 0,22µm Vacuum Filter Units	Merck Millipore, Darmstadt, Germany
Syringe BD Microfine 1 ml	Becton, Franklin Lakes, NJ,USA
Syringe Filter (0.22µm)	Merck, Darmstadt, Germany
TLC Aluminum Sheets Silica Gel 60F_{154}	Merck Millipore, Darmstadt, Germany
Ultra low cluster 96 well plates U-bottom plates	Corning Inc., Corning, NY, USA

Ultra Turrax disperser tubes BMT-G	IKA, Staufen im Breisgau, Germany
Ultrasound Gel	Dahlhausen, Köln, Germany

3.3 Chemicals

Table 6. *Chemicals.*

REAGENTS AND SOLVENTS	**COMPANY**
1,4 Dithiothreitol (DTT)	Sigma-Aldrich, Taufkirchen, Germany
10% Neutral buffered formalin	Leica Biosystems, Nussloch, Germany
10x TAQ reaction buffer	BioLabs, Ipswich, MA, USA
1-Bromo-3chloropropane	Sigma-Aldrich, Taufkirchen, Germany
2,5-dihydroxybenzoic acid (gentisic acid)	Sigma-Aldrich, Taufkirchen, Germany
2-Propanol	Sigma-Aldrich, Taufkirchen, Germany
Acetonitrile for DNA synthesis	Merck, Darmstadt, Germany
Agarose	Roth, Karlsruhe, Germany
AlexaFluor488 TFP ester (TEA salt)	Invitrogen, Carlsbad, USA
Alkaline phosphatase chromogen	Abcam, Cambridge, UK
Ammonium persulfate (APS)	Sigma-Aldrich, Taufkirchen, Germany
Boron trifluoride diethyl eterate	Sigma-Aldrich, Taufkirchen, Germany
Bovine serum albumine (BSA)	Sigma-Aldrich, Taufkirchen, Germany
BupH PBS Pack	Thermo Fischer Scientific, Waltham, USA
Carrier-free $Na^{125}I$	Hartmann Analytic, Braunschweig, Germany
Citric acid	Sigma-Aldrich, Taufkirchen, Germany
Coomassie Brilliant Blue	Bio-Rad Laboratories, Hercules, USA
Cy5.5 mono NHS ester	GE Healthcare, Buckinghamshire, UK
DAPI Solution (1 mg/mL)	Thermo Fischer Scientific, Waltham, USA
DEPTC treated water	Merck, Darmstadt, Germany
Para- isothyocyanatobenzyl - desferrioxamine (DFO-Bz-NCS)	Macrocyclics, Inc, Dallas, USA

Disodium phosphate	Sigma-Aldrich, Taufkirchen, Germany
DMEM	Invitrogen, Carlsbad, USA
DMSO	Sigma-Aldrich, Taufkirchen, Germany
dNTP Mix	BioLabs, Ipswich, MA, USA
DTPA	Sigma-Aldrich, Taufkirchen, Germany
Dulbecco's PBS	Merck, Darmstadt, Germany
EDTA	Invitrogen, Carlsbad, USA
EnVision+ System- HRP labelled Polymer	Dako, Agilent Technologies, Glostrup, Denmark
Ethanol	Merck, Darmstadt, Germany
Ethidium Bromide	Roth, Karlsruhe, Germany
Fetal bovine Serum (FCS)	Invitrogen, Carlsbad, USA
Ficoll	Biochrom, Berlin, Germany
Full range rainbow ECL marker	GE Healthcare, Buckinghamshire, UK
Glacial acetic acid	Sigma-Aldrich, Taufkirchen, Germany
Glycine	Sigma-Aldrich, Taufkirchen, Germany
H[^{18}F]	TU Munich, München Germany
Haematoxylin	Merck, Darmstadt, Germany
Hanks' Balanced Salt Solution	Invitrogen, Carlsbad, USA
HEPES	Invitrogen, Carlsbad, USA
Human serum	TU Munich, München Germany
Human thyrocytes total RNA extract	Takara, Japan
Hydrochloric acid 37%	Sigma-Aldrich, Taufkirchen, Germany
Iodine-124	BV Cyclotron VU, Amsterdam, Netherlands
Iodine-125	BV Cyclotron VU, Amsterdam, Netherlands
Isoflurane	CP Pharma, Burgendorf, Germany
Isopropyl alcohol	Merck, Darmstadt, Germany
Magnesium chloride	BioLabs, Ipswich, MA, USA

Methanol	Sigma-Aldrich, Taufkirchen, Germany
Monosodium phosphate	Sigma-Aldrich, Taufkirchen, Germany
NHS-Activated Agarose Dry Resin	Thermo Fischer Scientific, Waltham, USA
Non-fat dry milk powder	Sigma-Aldrich, Taufkirchen, Germany
Oxalic acid	Sigma-Aldrich, Taufkirchen, Germany
Paraformaldehyde (PFA)	Sigma-Aldrich, Taufkirchen, Germany
Penicillin/Streptomycin	Invitrogen, Carlsbad, USA
Potassium perchlorate	Sigma-Aldrich, Taufkirchen, Germany
PowerUP Sybr green mastermix	Applied Biosystem, Life technologies, Waltham, MA, USA
Protamine sulfate	MP Biomedicals, Illkirch, France
Recombinant human Galectin-3	Thermo Fischer Scientific, Waltham, USA
Recombinant protein G	R&D systems Minneapolis, MN, USA
Recovery Cell Culture Freezing Medium	Gibco, Grand Island, NY, USA
Roti®-Load 1 reducing protein loading buffer	Carl Roth, Karlsruhe, Germany
Roti®-Load 2 non-reducing protein loading buffer	Carl Roth, Karlsruhe, Germany
Rotiphorese® Gel 40	Carl Roth, Karlsruhe, Germany
RPMI 1640	Invitrogen, Carlsbad, USA
Sodium acetate	Sigma-Aldrich, Taufkirchen, Germany
Sodium azide	Sigma-Aldrich, Taufkirchen, Germany
Sodium bicarbonate	Sigma-Aldrich, Taufkirchen, Germany
Sodium carbonate	Sigma-Aldrich, Taufkirchen, Germany
Sodium chloride	Sigma-Aldrich, Taufkirchen, Germany
Sodium Dodecyl Sulfate (SDS)	Bio-Rad Laboratories, Hercules, USA
Sodium formate	Sigma-Aldrich, Taufkirchen, Germany
Sodium hydroxide	Sigma-Aldrich, Taufkirchen, Germany

Sodium Iodide	Sigma-Aldrich, Taufkirchen, Germany
Sulfuric acid 1M	Roth, Karlsruhe, Germany
TAQ DNA Polymerase	BioLabs, Ipswich, MA, USA
Technical buffer solutions for pHmeter pH 4.01, 7.00 and 10.01	Mettler Toledo, Schwerzenbach, Switzerland
TEMED	Sigma-Aldrich, Taufkirchen, Germany
TRIS	Sigma-Aldrich, Taufkirchen, Germany
Triton X	Bio-Rad Laboratories, Hercules, USA
TRIzol	Invitrogen, Carlsbad, USA
Trypan Blue	Applied Biosystem, Life technologies, Waltham, MA, USA
Trypsine / EDTA (0.5%)	PAA laboratories, Pasching, Austria
Tween20	Sigma Aldrich, Taufkirchen, Germany
Typan blue	Invitrogen, Carlsbad, USA
Ultra-low IgG Fetal bovine Serum	BIO&SELL, Feucht bei Nürnberg, Germany
Yeast RNA 10 mg/ml	Invitrogen, Carlsbad, USA
Zirconium (IV) chloride	Sigma-Aldrich, Taufkirchen, Germany
Zirconium-89	BV Cyclotron VU, Amsterdam, Netherlands

3.4 Oligodeoyxnucleotides

All the primers were synthetized by Sigma Aldrich. Unless otherwise specified the primers were designed according to the Primer3 software (Untergasser et al. 2012).

Table 7. *Primers.*

Gene	**Sequence 5'-3'**	**Reference**
GAPDH	Sense: GAGTCAACGGATTTGGTCGT Antisense: TTGATTTTGGAGGGATCTCG	(Li et al. 2016)
β-actin	Sense: GCGAGAAGATGACCCAGATC	

	Antisense GGATAGCACAGCCTGGATAG	
NIS	Sense: CTGCCCCAGACCAGTACATGCC Antisense: TGACGGTGAAGGAGCCCTGAAG	(Slominski et al. 2002)
Gal3	Sense: GCCTCGCATGCTGATAACAA Antisense: ACCGACTGTCTTTCTTCCCT	

3.5 Antibodies

3.5.1 Antibodies for western blot

Table 8. *Primary antibodies for western blot.*

Name	Isotype	Clone	Dilution	Company
Anti-Galectin-3	Rat IgG_{2a}	M3/38	1:5'000	Mabtech, Nacka Strand, Sweden
Anti-GAPDH	Mouse IgG_1	CB1001	1:6'000	Merck, Darmstadt, Germany
Anti-NIS	Mouse IgG_1	SPM186	1:500	Abcam, Cambridge, UK
Anti-TTF1	Rabbit IgG	07-601	1:500	Merck, Darmstadt, Germany

Table 9. *Secondary antibodies for western blot.*

Name	Isotype	Clone	Dilution	Company
Anti-Rat-AP	Goat IgG	A8438	1:5'000	Sigma Aldrich, Taufkirchen, Germany
Anti-Mouse-AP	Donkey IgG	AP192A	1:1'000	Merck, Darmstadt, Germany
Anti-Rabbit-HRP	Goat IgG	AP307A	1:5'000	Merck, Darmstadt, Germany
Anti-Mouse-HRP	Goat IgG	AP124P	1:5'000	Merck, Darmstadt, Germany

3.5.2 Antibodies for immunohistochemistry

Table 10. *Antibodies for immunohistochemistry.*

Name	Isotype	Clone	Company
Anti-Galectin-3-HRP	Rat IgG_{2a}	3720-3	Mabtech, Nacka Strand, Sweden
Anti-NIS	Rabbit IgG	GTX37599	Genetex, Irvine, CA, USA
Anti-Rabbit-HRP	Goat IgG	AP307A	Merck, Darmstadt, Germany

3.5.3 Antibodies for fluorescence microscopy

Table 11. *Antibodies for fluorescence microscopy.*

Name	Isotype	Clone	Company
Anti-γH2AX [p Ser139]	IgG1κ	2F3	Novus Biologicals, Littleton, USA

3.6 Media, buffers and solutions

3.6.1 Media

Table 12. *Media.*

NAME	COMPOSITION
BcPAP and FRO culture media	RPMI 1640 supplemented with 10% (w/v) FCS
CAL62 culture medium	DMEM supplemented with 10% (w/v) FCS
Binding medium	Dulbecco's PBS + 10% (w/v) BSA
Bleaching medium	Dulbecco's PBS + 5% (w/v) FCS
Washing buffer	Dulbecco's PBS + 1% (w/v) FCS

3.6.2 Buffers and solutions

Table 13. *Buffers and solutions.*

NAME	COMPOSITION	APPLICATION

Ammonium eluent	1M ammonium acetate, 50% (v/v) methanol	TLC run
Blocking buffer	PBST + 5% (w/v) non-fat dry milk	Western blot
Citrate solution	0.1M trisodium citrate dehydrate, pH5.0	TLC run
Coupling buffer	0.1M sodium phosphate, 0.15M sodium chloride, pH7.2	Protein G affinity column
Destaining solution	30% (v/v) methanol, 10% (v/v) glacial acetic acid	SDS-PAGE
DTPA solution	50mM DTPA, pH5.0	TLC run, stability test
Elution/storage acetic acid buffer	0.25M acetic acid, 3.2 mM gentisic acid	Purification, storage
HEPES buffer	0.5M HEPES, pH7.0	Tracer labeling
Hypotonic buffer	20mM HEPES, 1mM MgCl2, 0.5mM $CaCl_2$, pH7.4	Cell counting
Incubation buffer	0.1M sodium formate pH2.8	Tracer synthesis
RIPA buffer	14mM NaCl, 5mM TRIS, 0.35mM SDS, 2% Triton X-100, 1mM EDTA, 1% (v/v) Protease inhibitor cocktail	Cell lysis and protein extraction
Membrane lysis solution	5% (w/v) benzalkonium chloride, 3% (v/v) acetic acid	Cell counting
PBS	0.1M phosphate buffer, 0.15M sodium chloride, 0.05% (m/v) NaN_3 pH7.0	SE-HPLC
Non reducing loading buffer	250mM Tris-HCl pH6.8, 40% (v/v) glycerol, 8% (w/v) SDS, 3mM bromophenol blue	Electrophoresis (SDS-PAGE, WB)
Oxalic acid solution	1M oxalic acid	Tracer labeling

PBST buffer	PBS + 0,5% (v/v) Tween20	WB
Quenching buffer	1M TRIS, pH7.4	Protein G affinity column
Reducing loading buffer	250mM Tris-HCl pH6.8, 40% (v/v) glycerol, 200mM DTT, 8% (w/v) SDS, 3mM bromophenol blue	Electrophoresis (SDS-PAGE, WB)
Running buffer	25mM TRIS, 190mM glycine, 3.5mM SDS	Electrophoresis (SDS-PAGE, WB)
Sodium bicarbonate buffer	0.1M sodium bicarbonate	Probes synthesis
Sodium carbonate solution	2M sodium carbonate	Tracer labeling
Coomassie Brilliant Blue staining solution	45% (v/v) methanol, 10% (v/v) glacial acetic acid, 0.25% (v/v) coomassie blrilliant blue	SDS-PAGE
TAE buffer	2M TRIS, 1M glacial acetic acid, 0.5M Sodium EDTA pH8.0	Electrophoresis
Transfer buffer	48mM TRIS, 39mM glycine, 20% (v/v) methanol	WB

3.7 Kits

Table 14. *Kits.*

Name	**Company**
iScript cDNA Synthesis Kit	Bio-Rad Laboratories, Hercules, USA
LookOut Mycoplasma PCR Detection Kit	Sigma Aldrich, Taufkirchen, Germany
Pierce™ F(ab')$_2$ Preparation Kit	Thermo Fischer Scientific, Waltham, USA
Supersignal West Pico Chemiluminescent Substrate Kit	Thermo Fischer Scientific, Waltham, USA

3.8 Cell lines

Table 15. *Cell lines.*

Name	Type	Origin
BcPAP (RRID:CVCL_0153)	Human poorly differentiated thyroid gland carcinoma	DSMZ-German Collection of Microorganisms and Cell Cultures, Leibniz, Germany
CAL62 (RRID:CVCL_1112)	Human thyroid gland undifferentiated (anaplastic) carcinoma	DSMZ-German Collection of Microorganisms and Cell Cultures, Leibniz, Germany
FRO82-1 (RRID:CVCL_6287)	Human thyroid gland undifferentiated (anaplastic) carcinoma	American Type Culture Collection, Rockville, MD, USA

3.9 Mouse strain

Table 16. *Mouse strain.*

Strain	Origin
CD1-Foxn1$^{nu/nu}$ mice	Charles River Laboratories, Sulzfeld, Germany

3.10 Softwares

AIDA Image analyzer software version 4.21

Bio-Chrom Lite

Chromatography Data System (CDS) Software Chromeleon version 6.8

DB Biosciences CellQuest Pro

Graph Pad Prism version 5.01

ImageJ version 1.44d

Inveon Research Workplace

Keyence BZ-II Analyzer

Keyence BZ-II Viewer

Leica Aperio ImageScope version 12.3.1.5011

Life Technologies StepOne software version 2.3

Origin 2017 Version 94E

PerkinElmer ChemDraw professional version 15.1

VisEn FMT™2500 Software

VisualSonics Vevo Lab version 2.2.0

4 **METHODS**

4.1 Cell cultures

4.1.1 Cells storage and thawing

Before freezing, the cells were detached from the growing flask surface using 60µl/cm^2 of warm Trypsin / EDTA solution incubating for 5 min at 37°C. The obtained suspension was diluted 1:3 with the appropriate warm culture medium (see Table 12) to inactivate the trypsin and centrifuged at 500G for 3 min. The cell pellet was washed twice in ice cold Dulbecco's PBS and resuspended in 1 ml of ice-cold freezing medium in a cryotube. To ensure a gentle cooling rate (1°C/min) samples were put in a proper container (see Table 4) filled with isopropyl alcohol at -80°C for one night. For long term storage samples were moved to liquid nitrogen (-180°C). For cell thawing, the samples were briefly warmed at room temperature and poured in 10ml of culture medium centrifuging 500G for 3 min. The supernatant was removed, and the cell pellet was resuspended in the proper medium, transferred in an appropriate cell culture flask for monolayer growth and stored into an incubator at 37°C and 5% CO_2 atmosphere.

4.1.2 Monolayer growth procedure

After the thawing procedures the growth of the cells was monitored daily by medium color check and observation under microscope (see Table 4). Both the cell culture media used contain phenol red as indicator, when the color of the medium turned yellow, indicating a pH below 6.8, it was sucked out and replaced with fresh one. Microscope observations gave an approximated estimation of cells viability and degree of confluence. When the cells reached about 90% of confluence, they were detached from the cell culture flask as seen above, washed and resuspended in 10ml of PBS in order to be counted via Countess automated system (see Table 4). Briefly, 10µl of the suspension were mixed with 10µl of trypan blue and injected in the two wells of a Countess cell counting slide, this one was inserted in the counting system to obtain a measure of viability and of the number of the cells per ml. Therefore, the cells were centrifuged at 500G for 3 min, the pellet was resuspended in the adequate volume of culture medium and seeded in the appropriate number of flasks.

4.1.3 Three-dimensional growth procedure

Thyroid tumor spheroids were produced from BcPAP, CAL62 and FRO82-1 cell lines starting from monolayer cultures, to be used for *in vitro* binding experiments. 90% confluent cells were detached with trypsin / EDTA solution as already seen, then seeded with different densities in a U-bottom ultra-low attachment 96-well plate (see Table 5) bound with a hydrogel layer that inhibits cellular attachment. Each well contained 50, 100, 150 or 300 thousand cells in 200µl of cell culture medium. The plates were stored in an incubator at 37°C and 5% CO_2 atmosphere, and the formation of aggregates and spheroids were monitored for a maximum of seven days via digital microscope (see Table 4).

4.1.4 Characterization of the 3D structures

To count the number of cells that constitutes the 3D structures, the medium was removed from each well and replaced by lysis cold hypotonic buffer (see Table 13) pipetting until the breaking of the aggregates. After 15 min on ice, 1/10 volume of a membrane lysis solution was added, to dissolve the plasma membranes but leave the nuclei intact. The nuclei suspension was electronically counted in a Casy counter (see Table 4). The WST-1 transformation assay, which reflects the cell surface NADH oxidase activity dependent on intracellular availability of NADH, was used to monitor cell metabolism. Absorption was measured at 450nm using the ELISA reader (see Table 4), the measurement in each well was normalized with the number of cells in the spheroids.

4.2 Cell lines characterization

The selected human thyroid carcinoma cell lines CAL62, FRO82-1 and BcPAP, cultured as monolayer and as spheroids, were characterized for protein expression and gene expression of Gal3 and NIS by PCR and western blot (WB) respectively. Furthermore, an eventual mycoplasma contamination was investigated. After the characterization, the cell lines were maintained in culture for no longer than 5 months.

4.2.1 Total RNA extraction and cDNA production

For PCR characterization of the cell lines, total RNA extraction was carried out on 5 million cells resuspending them in a mixture of 1ml TRIzol, 200µl 1-Bromo-3chloropropane and 1µl Yeast RNA (see Table 6), with a reaction time of 5 min at room temperature. After a centrifugation at 21'000G for 15 min at 4°C, the clear part of the supernatant was added to 500µl of isopropanol and left at -20°C overnight to precipitate the RNA. The sample was centrifuged at 21'000G for 20 min at 4°C and the pellet washed with ethanol 75% and dissolved in 20µl DEPC-treated water (see Table 6). Concentration and stability of the RNA solution were determined via NanoDrop (see Table 4) measuring the absorption at 260 and 280nm.

The cDNA was synthetized incubating 1µg RNA, dissolved in 16µl of DEPC-treated water, adding 4µl of iScript cDNA Synthesis Kit (see Table 14) in a cycler system (see Table 4) with the following program: 5 min at 25°C, 20 min at 46°C and 1 min at 95°C.

4.2.2 Preparation of the agarose gel

Agarose gel layers were prepared in order to separate nucleic acids via electrophoresis. Briefly, 1 or 1.5% (w/v) agarose were dissolved in TAE buffer (see Table 13) heating in a microwave oven up to 80°C. During the consequent cooling step, when the temperature of the solution was below 60°C, an ethidium bromide (see Table 6) solution was added to a concentration of 2.5µM. Finally, the solution was left 20 min at room temperature for polymerization in an appropriate mold (see Table 4).

4.2.3 Characterization via PCR

The amplification of the specific sequences of interest, belonging to Gal3 (LGALS3), NIS (SLC5A5) and GAPDH genes, was performed via TAQ Polymerase-mediated PCR (see Table 13) in a thermal cycler system. The reactions were performed in a total volume 25µl containing 1µl of cDNA, 2.5µl of TAQ reaction buffer, 1.5µl of magnesium chloride 25mM, 0.5µl of 10mM dNTP Mix, 0.125µl TAQ DNA Polymerase and 0.5 µl of primers (sense and antisense for each gene as seen in Table 7) in DEPC water with a final concentration 650nM each. The thermal cycle protocol is described in Table 17.

Table 17. *Thermal cycle protocol for PCR amplification.*

Step	Temperature	Duration	Repetitions
Denaturation	95°C	1 min	1
Amplification	95°C 60°C 65°C	30 sec 30 sec 1 min/kbp	40
Finalization	65°C	5 min	1

After the amplification, 8µl of each PCR product was resolved via electrophoresis on a 1% agarose gel in TAE buffer using a voltage of 80V for 1 hour and stained with ethidium bromide. The bands were visualized using the Omega Lum C Imaging System (see Table 4). A densitometric analysis of the signals was performed using the ImageJ (see paragraph 3.10) and normalizing for the GAPDH values.

4.2.4 RT-PCR

For each cell line the expression of Gal3 (LGALS3), NIS (SLC5A5), GAPDH and β-actin (ACTB) genes was evaluated via quantitative RT-PCR. The analysis was performed using a StepOne Real-Time PCR System with SYBR Green Master Mix. The reactions were performed in a total volume 10µl containing 2µl of pre-diluted 1:5 cDNA, 8µl of SYBR Green and primers (sense and antisense each gene as seen in Table 7) concentrated 650 nM each. The reaction was performed according to the manufacturer recommendations and it is described in Table18.

Table 18. *Thermal cycle protocol for RT-PCR.*

Step	Temperature	Duration	Repetitions
Denaturation	50°C 95°C	2 min 3 min	1
Amplification	95°C 65°C	30 sec 20 sec	40
Melting curve	65°C, increasing 0.3°C/sec	100 sec	1

Data was carried out with the $\Delta\Delta C_t$ method, using GAPDH and β-actin as housekeeping genes (Livak and Schmittgen 2001).

4.2.5 Protein extraction

To perform WB analyses, the cytosolic and membrane protein pool was extracted via cell lysis resuspending 5 million cells in 300µl of freshly prepared RIPA buffer (see Table 13). The reaction was carried out on ice for 30 min, vortexing for 30 seconds every 5 minutes. Therefore, the suspension was centrifuged at 20'000G for 10 min at 4°C and the supernatant was collected. The concentration of proteins was determined by a NanoPhotometer (see Table 4) at an absorbance of 280nm using BSA as a standard.

4.2.6 Preparation of polyacrylamide gels

Polyacrylamide (PAM) gels were prepared for the electrophoresis of proteins. The gels were prepared polymerizing a stacking gel solution and a running gel solution in the Mini-PROTEAN® Tetra cell system mold at room temperature. For the gel composition see Table 19.

Table 19. *SDS-PAGE gel composition.*

	Stacking gel	**Running gel**
Water	5.6ml	6ml
1.5M TRIS pH8.8	-	3.75ml
0.5M TRIS pH6.8	2.6ml	-
30% Acrylamide/Bisacrilamide solution	1.66ml	4.95ml
10% (w/v) SDS	100µl	150µl
TEMED	10µl	6µl
10% (w/v) APS	100µl	150µl

The running gel solution was poured in the mold up to 8 cm of height and layered with isopropyl alcohol. After 30 min, the isopropyl alcohol was removed, and the stacking gel solution was added until the upper limit of the mold inserting a comb to shape the wells and let polymerize for further 30 min. The gels were stored wrapped in wet paper at 4°C up to one week.

4.2.7 Characterization via WB

Cell lysates were used for cell characterization via WB. Together with Gal3 and NIS protein expression, also the thyroid transcription factor 1 (TTF1), was evaluated.

After removing the comb, the gel was placed in the electrophoresis chamber pouring in running buffer. Then 20µg of protein extract were diluted to a concentration of 1mg/ml in PBS plus non-reducing protein loading buffer (see Table 13) 4:1 and heated at 90°C for 2 min for protein denaturation. After cooling each sample was loaded in the respective well as well as Full-Range Rainbow protein reference marker (see Table 6), and the run performed at 100V for 90 min. Then, the gel was transferred to the blotting cell onto a PVDF membrane (see Table 5) pretreated in methanol for 5 seconds, transfer buffer was added, and the blotting performed at 100V for 45 min. The membrane was detached from the gel, then blocked in blocking buffer at room temperature for 1 hour and incubated with the primary antibody recognizing each protein (see Table 8) in blocking solution at 4°C overnight. Incubation with secondary antibodies (see Table 9), was performed for 1 hour at room temperature after washing the membrane in PBST. For the detection of Gal3 and TTF1 a colorimetric approach was used by AP-conjugate antibodies, then the bands were visualized incubating the membrane with alkaline phosphatase chromogen for 5 min. The signal corresponding to the NIS was detected using HPR-conjugate antibodies, visualized after 5 min incubation at room temperature with an exposure of 20 min time on a CL-XPosure Film (see Table 5). Results were evaluated via densitometric analysis of the signals using the ImageJ software and normalized with the GAPDH bands.

4.2.8 Mycoplasma contamination assay

RNA extracts from monolayer cells were used to exclude mycoplasma contamination via PCR detection using a LookOut mycoplasma PCR detection kit (see Table 14). Sample solutions and control were prepared as reported by the producer and incubated in the thermocycler system with the protocol showed in Table 20.

Table 20. *Mycoplasma detection thermal cycle protocol.*

Step	Temperature	Duration	Repetitions
Denaturation	94°C	2 min	1
Amplification	95°C	30 sec	40
	55°C	30 sec	
	72°C	40 sec	
Cooling	16°C	-	1

8µl of the samples were loaded in a 1.2% agarose gel and run in TAE buffer at 80V for 45 min. The staining was performed using ethidium bromide and the bands were visualized using the Omega Lum C Imaging System.

4.3 Anti-Gal3 F(ab')$_2$ fragment production

The Anti-Gal3 F(ab')$_2$ fragment (aGal3-(Fab')$_2$) was prepared from a well characterized anti-Gal3 rat mAb M3/38 from Mabtech (Inohara and Raz 1995) via pepsin digestion. The product was purified using a protein G affinity column to remove unreacted mAb and Fc fragments and used afterwards to produce the imaging probes.

4.3.1 Anti-Gal3 mAb digestion

The Pierce F(ab')$_2$ Preparation Kit (see Table 14) was used to produce the aGal3-(Fab')$_2$ via pepsin digestion following the producer instructions with slight modifications. 3 to 6mg of rat mAb to Gal3 in PBS underwent to a pre-conditioning step performing a buffer exchange with 50kDa centrifugal filters (see Table 4) in 0.1M sodium formate at pH2.8 to a concentration of 3mg/ml and incubated for 16 hours at 4°C. This process affects the conformation of the Cγ_2 domain that is not completely reversed on return to a higher pH, and increases its susceptibility to proteolysis (Stewart and Stanworth 1975; Rousseaux, Rousseaux-Prevost, and Bazin 1983). After a second buffer exchange to F(ab')$_2$ preparation kit digestion buffer (20mM sodium acetate, pH4.4), the mAb was incubated for enzymatic digestion with immobilized pepsin (F(ab')$_2$ Preparation Kit), 500U per mg of antibody, for 2 hours at 37°C, under rotation. The product was separated from the pepsin via centrifugation at 5000G for 1 min in a 0.8ml centrifugation column. To maximize the recover, the resin was rinsed and centrifuged 5000G

for 1 min two times with 0.5ml BupH PBS (see Table 6). The fractions were collected together for purification.

4.3.2 Protein G affinity column preparation

To prepare the protein G affinity column, 1ml of wet NHS-Activated Agarose Resin (see Table 6), corresponding to 150mg of dry resin, was added in a 5ml centrifuge column with a fiberglass filter and incubated 1 hour at room temperature, under mixing, in presence of 2.5ml of a 46µM protein G solution in coupling buffer (see Table 13). After the incubation the mixture was centrifuged at 1000G for 1 min and washed three times with 4ml coupling buffer. The agarose resin free sites were blocked by reaction with 2ml quenching buffer (see Table 13), incubating under mixing for 30 min at room temperature. Therefore, the resin was rinsed three times with 4ml BupH PBS (pH 7.0, see Table 13) and stored at 4°C in 3ml BupH PBS + 0.02% (w/v) sodium azide.

4.3.3 aGal3-F(ab')$_2$ fragment purification

The product of the enzymatic digestion was purified from unreacted mAb and Fc fragments using the protein G affinity column. The affinity column was equilibrated with BupH PBS and the sample loaded up to 1.5ml. After 30 min end-over-end mixing at room temperature the aGal3-F(ab')$_2$ was eluted centrifuging at 1000G for 2 min. The mAb and Fc fragments were detached and eluted centrifuging at 1000G for 1 min in presence of 3ml of aGal3-F(ab')$_2$ preparation kit IgG elution buffer three times. Finally, the column was regenerated repeating rinsing and centrifuging steps three times at 1000G for 1 min with 4ml BupH PBS and stored as seen in paragraph 4.3.2.

4.4 Imaging probes production

4.4.1 AlexaFluor488 and Cy5.5 conjugation to aGal3-F(ab')$_2$

Two probes, aGal3-F(ab')$_2$-AlexaFuor488, for fluorescence microscopy, and aGal3-F(ab')$_2$-Cy5.5, for fluorescent molecular tomography (FMT) imaging, were produced by reaction with primary ammines, forming a covalent amide bond with the aGal3-F(ab')$_2$ lysine residues. For

this purpose, I used an AlexaFuor488 TFP ester and a Cy5.5 NHS ester (see Table 6), applying the same protocol for both the reagents. The dyes were dissolved in DMSO (see Table 6) reaching a concentration of 10mg/ml, then added to a solution 2mg/ml (~20µM) of aGal3-F(ab')$_2$ in sodium bicarbonate buffer at pH8.5 for the TFP ester and pH9.0 for the NHS ester, with an aGal-F(ab')$_2$: dye molar ratio of 1:20, and incubated in a thermomixer (see Table 4) at room temperature for 1 hour under 900rpm mixing. In both cases the volume of DMSO added in the reaction mixture was <3% (v/v). The products were purified from unreacted esters washing with PBS (see Table 13) using 30kDa centrifugal units and the degree of labeling (DOL) determined via spectrophotometer using the following equation:

$$DOL = \frac{A_{dye}\varepsilon_{F(ab')_2}}{(A_{280} - A_{dye}C_{280})\varepsilon_{dye}}$$

where A_{dye} and ε_{dye} are respectively the absorbance and the molar extinction coefficient at the absorption maximum wavelength of the dye (495 nm for AlexaFluor488 and 684 nm for Cy5.5), $\varepsilon_{F(ab')_2}$ is the molar extinction coefficient of a F(ab')$_2$ fragment (=140'000$M^{-1}cm^{-1}$), A_{280} is the absorption at 280nm (absorption maximum for proteins) and C_{280} is a correction factor depending on the dye spectral properties.

4.4.2 Conjugation of aGal3-F(ab')$_2$ with DFO

The aGal3-F(ab')$_2$ fragment was functionalized for labeling with ^{89}Zr by conjugation with a p-isothiocanatobenzyl derivative of DFO (DFO-Bz-NCS) (see Table 6). The reaction was performed as reported by Holland et al. (Holland et al. 2010) with slight modifications. A 2mg/ml (~20µM) solution of aGal3-F(ab')$_2$ in in 0.1 M $NaHCO_3$ pH 9.0 was prepared via buffer exchange using a 30kDa centrifugal unit (see Table 5). 1mg of DFO-Bz-NCS was dissolved in DMSO to a concentration of 5mM and a 3-fold molar excess was then added to the aGal3-F(ab')$_2$ solution, followed by incubation under stirring in a reactor at 37°C for 30 min. The product (aGal3-F(ab')$_2$-DFO) was purified from non-conjugated chelator by size exclusion chromatography with a Sephadex G-25 PD-10 (see Table 5) column using acetic acid as elution buffer (see Table 13).

4.4.3 Labeling of aGal3-F(ab')$_2$-DFO with ^{89}Zr

1mCi (=37MBq) of ^{89}Zr-oxalate solution was brought to 100µl with oxalic acid solution and neutralized with 45µl of sodium carbonate solution. After 3 min of incubation at room temperature 150µl of HEPES buffer at pH7.0 (see Table 14) were added, followed by addition of 100µl of aGal3-F(ab')$_2$-DFO 1mg/ml (~10µM) solution in sodium acetate buffer and again 355µl HEPES buffer (pH 7.0), to reach a pH between 7.0 and 7.4. The reaction solution was incubated at 37°C for 30 min. The labelled product (aGal3-F(ab')$_2$-DFO-^{89}Zr) was purified from unchelated ^{89}Zr by Sephadex G-25 PD-10 column with 0.25 M acetic acid + 5g/l gentisic acid buffer (see Table 6).

4.5 Analytical methods

4.5.1 Sodium Dodecyl Sulfate - PolyAcrylamide Gel Electrophoresis (SDS-PAGE)

The purity and integrity of the aGal3-F(ab')$_2$ fragment and the aGal3-F(ab')$_2$-DFO-^{89}Zr tracer were evaluated via SDS-PAGE analysis on a 10% polyacrylamide gel, comparing it with the undigested full anti-Gal3 mAb. 1mg/ml solutions of aGal3-F(ab')$_2$ and mAb were prepared in PBS plus reducing loading buffer (see Table 13) 1:5 and in PBS plus non-reducing loading buffer (see Table 13) 1:4, heated at 90°C for 2 min to denature the proteins. After cooling, added to the PAM gel wells in the electrophoresis chamber with running buffer. Same procedure was operated on 2µCi of aGal3-F(ab')$_2$-DFO-^{89}Zr. The run was performed at 100V for 90 min using a Full-range Rainbow protein marker as reference, followed by staining with Coomassie Brilliant Blue staining solution (see Table 13) for 20 min at room temperature, under gentle mixing. The gel was then rinsed in destaining solution to remove the excess of blue Coomassie for 1 hour and stored in distilled water at 4°C.

Images of the gel were acquired by scanning with an EPSON AL-CX11 scanner (see Table 4), followed by autoradiography analysis performed by incubating the gel over a phosphor imaging plate (see Table 5) for 24h, and reading the signal with imaging plate scanner (see Table 4).

4.5.2 Instant thin layer chromatography (iTLC)

To verify the tracer radiochemical purity 2µl of the sample were spotted at the base of a 10cm-strip of glass microfiber chromatography paper impregnated with silic acid (see Table 5), and eluted with citrate solution at pH5.0 (see Table 13) (R_f F(ab')$_2$-DFO-^{89}Zr = 0.1; R_f free^{89}Zr = 0.9). The activity signal was read by radio-TLC-scanner (see Table 4) and the data was processed using the Bio-Chrom Lite software (see paragraph 3.10).

4.5.3 Size exclusion high performance liquid chromatography (SE-HPLC)

Radio-High Performance Liquid Chromatography (radio-HPLC) analyses of the aGal3-F(ab')$_2$ fragment and derived probes were performed on a Prominence HPLC system (see Table 4) equipped with a silica-based size exclusion column Yarra 3µm SEC3000 (see Table 4). The samples were prepared by diluting probe with PBS to a concentration of 0.2mg/ml (0.07µCi/ml, 1.89 GBq/ml), and then injected in column in a total volume of 50µl. All the runs were carried out in isocratic gradient using PBS buffer pH 7.0 as eluent, at 1 ml/min flow.

The UV/vis profile was acquired via UV/vis detector at 280, 480 for AlexaFluor488 conjugates and 700nm for Cy5.5 conjugates. The radioactive detection was performed by a GABI Star γ-detector. The acquisition and processing of the results were performed using Chromaleon 6.8 chromatography software (see paragraph 3.10).

4.6 Radiometric isotopic dilution assay

The determination of accessible DFO molecules of the aGal3-F(ab')$_2$ was performed via radiometric isotopic dilution assay using a modified version of the protocol described by Holland et al. (Holland et al. 2010). Briefly, the aGal3-F(ab')$_2$-DFO labeling reaction was performed scaling down the reaction reported in paragraph 4.4.3 in order to use 65pmol of radioimmunoconjugate and in presence of a 1:2 serial dilutions of non-radioactive $ZrCl_4$ (see Table 6) from 250 to 0.5pmol. For each reaction the yield was monitored via iTLC run in 50 mM DTPA pH 5. The number of accessible DFO was calculated by non-linear regression analysis, extrapolating the concentration in which only 50% of the conjugate was labeled.

4.7 *In vitro* stability studies on aGal3-F(ab')$_2$-DFO-^{89}Zr

The *in vitro* stability of the radioactive tracer was assessed at different time points in triplicate (*n*=3) via radio-TLC as described by Perk et al. (Perk et al. 2005). Freshly produced and purified aGal3-F(ab')$_2$-DFO-^{89}Zr in acetic acid buffer was stored at 37°C up to 96 hours as well as dilutions 1:10 in human serum, in sodium citrate buffer pH5.5 with 5 g/l of gentisic acid (storage solution) and in a solution 50mM DTPA pH 5. Every 24 hours 2.0 µl of the samples were spotted on a TLC aluminum strip with silica gel 60F$_{154}$ (see Table 5) eluting with a 1:1 mixture 2mM citrate buffer/DTPA 50mM (pH5.0) (Rf tracer = 0.1, Rf free^{89}Zr = 0.9).

4.8 Fluorescence microscopy

4.8.1 Determination of the aGal3-F(ab')$_2$-AlexaFluor488 dissociation constant via flow cytometry

The dissociation constant (K_d) of the aGal3-F(ab')$_2$-AlexaFluor488 conjugate was assessed on BcPAP via flow cytometry. 3x10^5 cells were incubated with different concentrations of aGal3-F(ab')$_2$-DFO-AlexaFluor488, from 5x10^{-8} to 5x10^{-11}M, in PBS / BSA 1% at pH7.4 for 1h on ice with or without a 100-fold excess of unlabeled aGal3-F(ab')$_2$. Then, the cells were washed in FACS buffer (see Table 13) and incubated for 20 min at room temperature in the dark with FACS buffer + propidium iodide (PI). Only PI negative (viable cells) were gated and analyzed using the FACSCalibur instrument (see Table 4). Data was acquired using CellQuest Pro software (see paragraph 3.10). The dissociation constant was calculated plotting the theoretical mean fluorescence intensity (MFI) values versus the fluorescent probe concentration and non-linear regression analysis using the GraphPad Prism 4.0 software.

4.8.2 Fluorescence microscopy on monolayer cells

To confirm the binding *in vitro* on all the selected cell lines, fluorescence microscopy imaging was performed using the aGal3-F(ab')$_2$-AlexaFluor488 fluorescent probe. Trypsinized cells were seeded in 8-well chamber slide (see Table 5) and incubated with growth medium in an incubator until 80% confluence. Afterwards, the growth medium was sucked out and replaced with different working solutions containing each 10µg/ml, 5µg/ml and 2µg/ml of aGal3-F(ab')$_2$-

AlexaFluor488 in growing medium. After 1 hour of incubation at 37°C the cells were washed twice with ice cold PBS and imaged with the Biorevo 9000E microscope (see Table 4) using a Nikon Plan Fluor 20x lens for fluorescence microscopy.

4.8.3 Fluorescence microscopy on cell spheroids

To characterize the time-dependent penetration and binding of the anti-Gal3 antibody fragment at the micro-tumor level, spheroids of all cell lines, prepared as seen in chapter 4.1.2, were incubated in three different working solutions containing respectively 10µg/ml, 5µg/ml and 2µg/ml of the conjugate aGal3-F(ab')$_2$-AlexaFluor488 in growing medium up to 24 hours at 37°C and 5% CO_2 atmosphere. At different time points (1, 2, 5, 8 and 24 hours), spheroids were carefully washed twice with ice cold PBS and imaged with the Biorevo 9000E microscope using a Nikon Plan Fluor 10x and 20x lenses for fluorescence microscopy. These analyses were performed in triplicate (*n*=3).

4.9 *In vitro* binding studies on aGal3-F(ab')$_2$-DFO-^{89}Zr and ^{124}I

4.9.1 Immunoreactivity of aGal3-F(ab')$_2$-DFO-^{89}Zr to cells

The immunoreactivity of ^{89}Zr-DFO-F(ab')$_2$ to Gal3 was assessed on all the cell lines selected for this project using a modified protocol derived from Lindmo et al. (Lindmo et al. 1984). Seven serial dilutions of cells, from $3.0x10^6$ to $1x10^5$, were incubated 1 hour at 0°C in 500µl PBS / BSA 1% in presence of a constant concentration of radiotracer ($1x10^{-8}$M) in triplicate (*n*=3). Non-specific binding was determined incubating the cells in the same conditions by adding a 100-fold excess of non-labeled aGal3-F(ab')$_2$-DFO. Cells were, therefore, centrifuged at 500G for 3 min, the supernatant was removed, the pellet rinsed twice in PBS / BSA 1% and the associated activity counted in a gamma-counter (see Table 4), correcting for the background activity. The immunoreactive fraction was determined by linear regression, plotting (total/bound) activity versus (1/[normalized number of cells]) and calculating the inverse of the intercept value on ordinate axis (1/Y intercept) of the linear regression curve, representing infinite antigen excess. The data were analyzed using Graph Pad Prism Software 4.0.

4.9.2 Saturation binding assay of aGal3-F(ab')$_2$-DFO-^{89}Zr to cells

To determine the dissociation constant (K_d) of the radiotracer, saturation binding studies were performed on BcPAP, FRO82-1 and CAL62, grew as monolayers. 600'000 cells were incubated in seven solutions with different concentrations of aGal3-F(ab')$_2$-DFO-^{89}Zr, from 5x10^{-8} to 5x10^{-11}M, in PBS / BSA 1% (pH7.4) in triplicate (*n*=3). After 2 hours incubation at 0°C, cells were collected, centrifuged at 500G for 3 min to separate the supernatant from the pellet, then rinsed two times with ice cold PBS and counted in a gamma-counter. To determine the nonspecific fraction the same procedure was carried out in parallel adding to each solution a 100-fold molar excess of non-labeled tracer. The specific binding was then assessed subtracting the unspecific binding from the values obtained from total tracer binding on the cells. Data were background corrected, plotted as counts per minute (cpm) versus tracer concentration and analyzed by nonlinear regression method using GraphPad Prism software 4.0 to determine the K_d and B_{max} values.

4.9.3 aGal3-F(ab')$_2$-DFO-^{89}Zr to cells internalization assay

The internalization of the tracer into monolayer cells was evaluated in triplicate (*n*=3) at different time points. After being detached from the flasks, the cells were incubated in V-bottom tubes (1x10^6 cells/tube) in 500µl PBS/BSA 1% for 1 h at 0°C, to ensure a complete stop of the metabolism, and then the radiotracer was added to each well to a concentration of 2x10^{-8}M continuing the incubation at 0°C for another hour. Then, the cells were centrifuged at 500G for 5 min, the supernatant (unbound fraction) was removed and the pellet resuspended in 500µl of the appropriate growth medium, followed by incubation at 37°C, in presence of 5% CO_2. At each defined time point (5, 15, 30, 75, 120, 240 minutes and 24 hours) the cells were centrifuged at 500G for 5 min, the supernatant (released fraction) was collected and the pellet rinsed twice with ice cold growth medium. To detach the tracer bound to the cell membrane (bound fraction), the pellets were further washed twice with an acidic buffer 0.05M NaOAc / 0.15M NaCl at pH 2.0. The activity left in the pellet (internalized tracer) and the other two fractions were measured in a gamma-counter.

4.9.4 Iodine-125 accumulation studies on monolayer cells and spheroids

For accumulation studies, iodine-125 (^{125}I) was used as surrogate of radioiodine species of common use in nuclear medicine (iodine-131, iodine-123), the studies were performed as previously reported by Spitzweg et al. (Spitzweg et al. 1998) with slight modifications.

Monolayer cells were trypsinized and seeded in V bottom tubes ($1x10^6$ cells/tube) in 500µl growth medium containing 2µCi of carrier-free $Na^{125}I$ (see Table 6) and 30µM NaI then incubated for 30 min at 37°C. To determine unspecific binding, control cells were pre-incubated with 300µM of $KClO_4$ dissolved in growth medium for 30 min at 37°C. After the incubation, the cells were centrifuged at 500G for 5 min and 4°C, the supernatant was removed, then the cells were washed three times with 500µl of ice-cold PBS / BSA 1%. The activity bound to the pellets were counted in a gamma-counter.

Cell spheroids, produced as described in the paragraph 4.1.3, were incubated at 37°C for 2 hours with 200µl of growth medium containing 2µCi of carrier-free $Na^{125}I$ and 30µM NaI, while control spheroids were preincubated with 200µl of a $KClO_4$ solution, as seen above. After the incubation, the spheroids were centrifuged and washed as previously described and then the related activity accumulated into the cells counted in a gamma-counter. All the tests were performed in triplicate (*n*=3) and repeated at least three times.

4.9.5 aGal3-F(ab')$_2$-DFO-^{89}Zr accumulation studies on cell monolayer and spheroids

Spheroids of various dimensions deriving from all the cell lines selected for the study, were cultured as described in paragraph 4.1.3, and then cooled on ice for 1 hour to ensure the complete stop of the cellular metabolic processes. The growth medium was carefully removed and the ^{89}Zr-DFO-Fab_2 tracer at a working solution of $1x10^{-8}$ M of in ice cold growth medium was added. To evaluate the unspecific binding an identical solution with a 100-fold excess of non-labeled aGal3-F(ab')$_2$-DFO was applied to the spheroids. After 2 hours of incubation at 37°C degrees, the spheroids were transferred in V-bottom tubes (see Table 5) and separated from supernatant by centrifugation at 500G for 5 min at 4°C, then washed three times with 300µl of ice-cold PBS. Cell associated activity was finally counted by gamma-counter. The tests were performed in triplicate (*n*=3) and repeated at least three times.

4.10 Orthotopic xenograft models establishment

To perform *in vivo* tests, six weeks old female athymic CD1-Foxn1$^{nu/nu}$ nude mice (see Table 16) were used as hosts for establishing thyroid cancer orthotopic models by transplanting the selected human thyroid cancer cells in the thyroid left lobe of the mice as previously described elsewhere (Buther et al. 2012; Sewell, Reeb, and Lin 2013). Before the engraftment, the mice were anesthetized with a two steps procedure: first, they were anesthetized by intraperitoneal injection (i.p.) of a full antagonizing fentanyl/midazolam injection solution (0,04mg/kg fentanyl; 4mg/kg midazolam), then, once each animal showed apparent inertia by striking the legs due to action of the anesthetic, they were maintained in anesthesia with 4% v/v isoflurane with concomitant administration of oxygen. The depth of anesthesia was controlled via detection of the wipe toes reflexes. Reached the surgical tolerance (anesthesia stage III2), the animals were placed supine on the surgical table, heated at 37°C, under the Stemi DV4 stereomicroscope (see Table 4) and injected subcutaneously with analgesic 0.1mL of Rimadyl (50mg/mL Carprofen). A midline cervical incision was made using a scalpel, the two lobes of thyroid gland, which directly cover the trachea laterally, were exposed by retracting the overlying submandibular glands with clamps and longitudinally dissecting the sternohyoid muscle adjacent to the trachea. For intra-thyroid implantation, cells were resuspended in ice cold PBS at a concentration of 1x10^{5}cells/µl, 10µl were drawn into a 10µl Hamilton syringe (see Table 4) tipped with a 27-gauge needle and then carefully injected in the thyroid left lobe. Afterwards, soft tissues and submandibular glandular structures were repositioned and the skin sutured, the animals received a solution of Rimadyl 4,0-5,0 mg/kg diluted 1:10, every 24 h until 72 h as a post-operative analgesic management and were monitored for any surgery or anesthesia-related complications. All experimental protocols were approved by the local authorities (Regierung von Oberbayern, Germany: license: 55.2-1-54-2532-216-15).

4.11 Orthotopic tumors growth monitoring

4.11.1 Tumor growth monitoring via ultrasound (US) scan

For all the cell lines injected the tumor growth was monitored weekly via US scan using the Vevo 2100 Imaging System, equipped with a MS550D transducer (see Table 4) fixed on the support of a rail system, furnished of a 3D motor stage for three-dimensional reconstruction. Mice were anesthetized with 5% v/v isoflurane/O_2 using a Vapor 2000 Dräger Fill system (see Table 4) and then placed supine on a surgical board, heated to 37°C, under a constant flow of isoflurane/O_2 between 2 and 1.5% (v/v) at 600ml/min. The transducer was placed on the neck region, previously soaked with ultrasound-gel, and the ultrasound scan was performed initially in color Doppler mode in order to have the carotid arteries as internal referral. Then, the animals were scanned using the B-Mode with a frame rate of 20Hz until the visualization of the transversal section of the thyroid lobes. The extension of the malignant lesion and its dimension were carefully evaluated moving the transducer on the longitudinal axis, then screens were acquired. For a 3D reconstruction and volume estimation of the tumors a three-dimensional image was acquired and processed using the Vevo LAB software (see paragraph 3.10). When the tumor reached a diameter of 0.5cm with a volume around 60mm^3, mice underwent to FMT imaging.

4.11.2 Fluorescence molecular tomography (FMT) imaging

To verify the neoplastic nature of the mass growing in the left lobe and, at the same time, to confirm the *in vivo* binding of the aGal3-F(ab')$_2$ fragment on tumor expressing Gal3, FMT scan was performed on mice bearing a tumor with a volume ~60mm^3. The imaging was performed using the small-animal imaging system FMT2500 (see Table 4). Briefly, mice were anesthetized under a flux of 5% v/v isoflurane/O_2, then received via catheter 54µg of aGal3-F(ab')$_2$-DFO-^{89}Zr, corresponding to 2nmol of NIR-dye, in a total volume of 200µl by i.v. injection into the tail vein. After 48 hours the mice were asleep in a box filled with 5% v/v isoflurane/O_2 and placed into the FMT system imaging chamber maintaining the anesthesia with a 1.5% v/v isoflurane/O_2 flux. A region of interest (ROI) was drawn via VisEn FMT™2500 software (see

paragraph 3.10) on the preview image to define the cervical region of the animal body. During the scan, near-infrared laser diode, set to 675nm, trans-illuminated the cervical regions and the emission signal was detected via CCD camera placed at the opposite side. Image reconstruction and analysis was performed by VisEn FMT™2500 Software. Approximate ROIs of 100mm^3 were drawn in the neck region encompassing respectively the right and left thyroid lobe. The relative accumulated antibody fragment quantity calculated via software.

4.12 PET/CT imaging

The imaging studies were performed using the Inveon small animal PET/CT scanner (see Table 4).

For each tumor cell line (BcPAP, CAL62 and FRO82-1) two groups of mice consisting in 10 animals (*n*=10) underwent PET/CT imaging after the injection of iodine-124 (^{124}I), as surrogate of radioiodine species used in nuclear medicine, and aGal3-F(ab')$_2$-DFO-^{89}Zr, respectively. The animals were positioned in the field of view (FOV) of the device under a constant flux of 1.5% v/v isoflurane/O_2 and, after a 10 min CT acquisition, a 30 min PET static acquisition was performed in the range of 425-650keV. Images were reconstructed using OSEM3D/MAP algorithm. Data were normalized and corrected for randoms, dead time and decay with no correction for attenuation or scatter.

4.12.1 PET/CT imaging of orthotopic tumor using aGal3-F(ab')$_2$-DFO-^{89}Zr

In vivo characterization of malignant versus normal thyroids was performed via immunoPET targeting Gal3 on three groups of mice (*n*=10 each) bearing BcPAP, CAL62 and FRO82-1 tumors. An additional group of healthy animals (*n*=10) was studied as a control. Each mouse was injected via catheter with 2.2 ± 0.2MBq (~7.4µgl) of aGal3-F(ab')$_2$-DFO-^{89}Zr in 250µl sodium acetate buffer (pH 5.5) in the tail vein. 48 hours after tracer injection, mice were anesthetized and imaged as already described. After the reconstruction, the PET/CT co-registered images were adjusted and a maximum intensity projection (MIP) performed using the Inveon Research Workplace software (see paragraph 3.10).

4.12.2 ^{124}I PET/CT imaging of orthotopic tumors

Three groups of mice (*n*=3) bearing respectively BcPAP, CAL62 and FRO82-1 tumors, were injected via catheter in the tail vein with 1.10 ± 0.01MBq of ^{124}I in 300µl of saline solution (NaCl 0.9% w/v). One group of healthy mice (*n*=3) was used as a control injecting the same activity. One hour after the injection the animal were anesthetized and imaged via PET/CT as already reported. The images were then adjusted using the Inveon Research Workplace software and MIP of co-registered PET/CT images were performed.

4.12.3 Tracer accumulation studies

The *in vivo* tumor uptake of aGal3-F(ab')$_2$-DFO-^{89}Zr was assessed via image-based quantification using the Inveon Research Workplace software. An approximate ROI was drawn encompassing the left side of the thyroid, including the whole tumor, and a smaller volume was selected setting a 50% threshold. The injected dose per gram percentage (%ID/g) was calculated with the following formula:

$$\%ID/g_{tumor} = \frac{A_{tumor}}{A_{tot} w_{tumor}} * 100$$

where A_{tumor} is the activity in each ROI (MBq), w_{tumor} is the weight of the tumor (g) measured post-mortem, and A_{tot} is the injected activity corrected for the decay. A dosimetric study was performed on one group of mice analyzing data of 30 min static acquisition acquired at 12, 24, 48 and 70 hours using OLINDA/EXM as described elsewhere (Stabin, Sparks, and Crowe 2005).

4.13 Ex vivo studies

4.13.1 Biodistribution analysis of ^{124}I and aGal3-F(ab')$_2$-DFO-^{89}Zr

After the PET/CT imaging sessions all animals were anesthetized, sacrificed and dissected. Tumors, blood and tissues (heart, lungs, liver, pancreas, spleen, stomach, kidneys, intestines, bladder, muscles, bones, brain and thyroid right lobe) were weighted and the associated activity was counted in a gamma-counter. The uptake was expressed as %ID/g using the following formula:

$$\%ID/g = \frac{C_{tissue}}{w_{tissue}(\bar{C}_{1\%std} * 100)} * 100$$

were C_{tissue} and w_{tissue} are respectively the count rates (cpm) and the weight (g) associated to the tumor or tissue; the results were then normalized by the total injected activity extrapolated counting five 1%-injected activity standards. To calculate the volume and compare it with the data obtained by US scan, tumors were measured using a calliper using the formula $Volume = \frac{4}{3}\pi r^3$, where r is the radius of the tumor. *In vivo* and *ex vivo* accumulation data were compared for correlation analysis. The right thyroid served as internal control.

4.13.2 Histology and immunohistochemistry

Histological and immunohistochemical analyses were performed by two independent pathologists, A. Bartolazzi (Pathology Research Laboratory, Sant'Andrea University Hospital) and K. Steiger (Institute of Pathology, Klinikum rechts der Isar). Excised tumors and thyroid right lobes were fixed in 10% neutral-buffered formalin solution for 48 hours, then dehydrated in standard conditions and embedded in paraffin. For histology and immunohistochemistry serial sections 3µm-thin were cut using a HM355S rotary microtome (see Table 4) and deparaffinized using a deparaffinizing xylene solution. Histology was performed treating the sections with Eosin and Mayer's Haemalaun according to a standard protocol. For immunohistochemistry deparaffinized tissues were pretreated first with citrate buffer pH 6.0 for 20 min for Gal3 or 30 min for NIS for antigen retrieval, then treated with 3% hydrogen peroxide and incubated with 3% goat serum, for peroxidase blocking and unspecific binding respectively. After pretreatments, immunohistochemical analysis were performed in a BondMax RXm autostainer using anti-Gal3 or anti-NIS primary antibodies (see Table 10). For the NIS staining the application of a secondary anti-rabbit antibody with a polymer refine detection kit was necessary. The antibody detection was visualized using diaminobenzidine (DAB, see Table 6), and the signal visualized as a dark brown precipitate. The healthy thyroid right lobes were used as a control. All slides were scanned with an Aperio AT2 (see Table 4) and evaluated with the Imagescope Software.

4.13.3 In vivo stability of aGal3-F(ab')$_2$-DFO-^{89}Zr

After biodistribution, the extraction of the activity was performed on tumor, blood and selected tissues (liver, kidneys and muscle). The blood was centrifuged at 1000G for 15 min to separate the blood cells from plasma, the two fractions were collected separately and counted in the gamma-counter. Organs and tumors were frozen in liquid nitrogen, then underwent to homogenization using the Ultra-Turrax system (see Table 4) with glass balls, the obtained samples were resuspended in 500µl PBS and centrifuged at 14'000G for 10 min to separate cells and particulate from the tracer. Plasma, tumors and organs extracts were spotted on an aluminum strip with silica gel 60F_{154} to perform a radio-TLC running with a 50mM DTPA solution (see section 4.7) and 20µl were loaded on a 10% polyacrylamide gel to perform an SDS-PAGE analysis as reported in paragraph 4.5.1. The activity from TLC and SDS-PAGE was visualized via autoradiography after 3-days incubation over a phosphor imaging plate.

4.14 Statistics

All the data is presented as mean ± standard deviations (SD). Statistical analyses are performed via GraphPad Prism 4.0 software using Student's t-test for unpaired data. Two-sided significance levels were calculated and $P<0.05$ $P<0.01$ values were considered statistically significant.

5 **RESULTS**

5.1 Production of TC cell spheroids

The development of the spheroids, structures comparable to microtumors was followed via imaging using digital microscope up to one week. The aim was to assess the time needed for obtaining a complete microtumors formation and to find out any difference due to the type of cells or the number of cells seeded. As expected, the generation of spheroids took more than 48 hours (Phung et al. 2011), independently from their size (Figure 6).

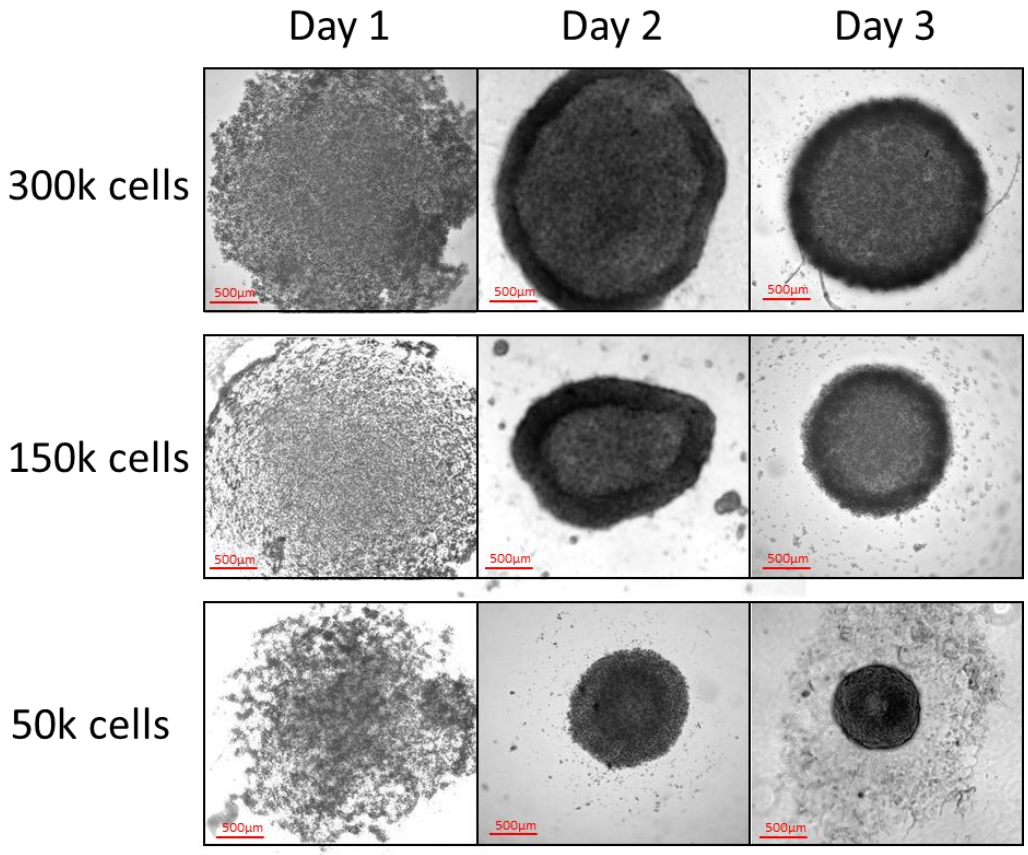

Figure 6. Development of BcPAP spheroids as representative data.
During the formation of BcPAP and CAL62 spheroids, it was possible to identify three different stages: from seeding up to 24 hours, the cells slowly accumulate at the bottom of the U-shaped well, forming aggregates; from 24 to 48 hours, a center of aggregation is visible with a significant difference between outer and inner part; from 48 hours, the spheroids became compact, showing in some cases necrosis in the inner part.

Both CAL62 and BcPAP needed three days to form a complete spheroid, while FRO82-1 can only form soft aggregates (Figure 7).

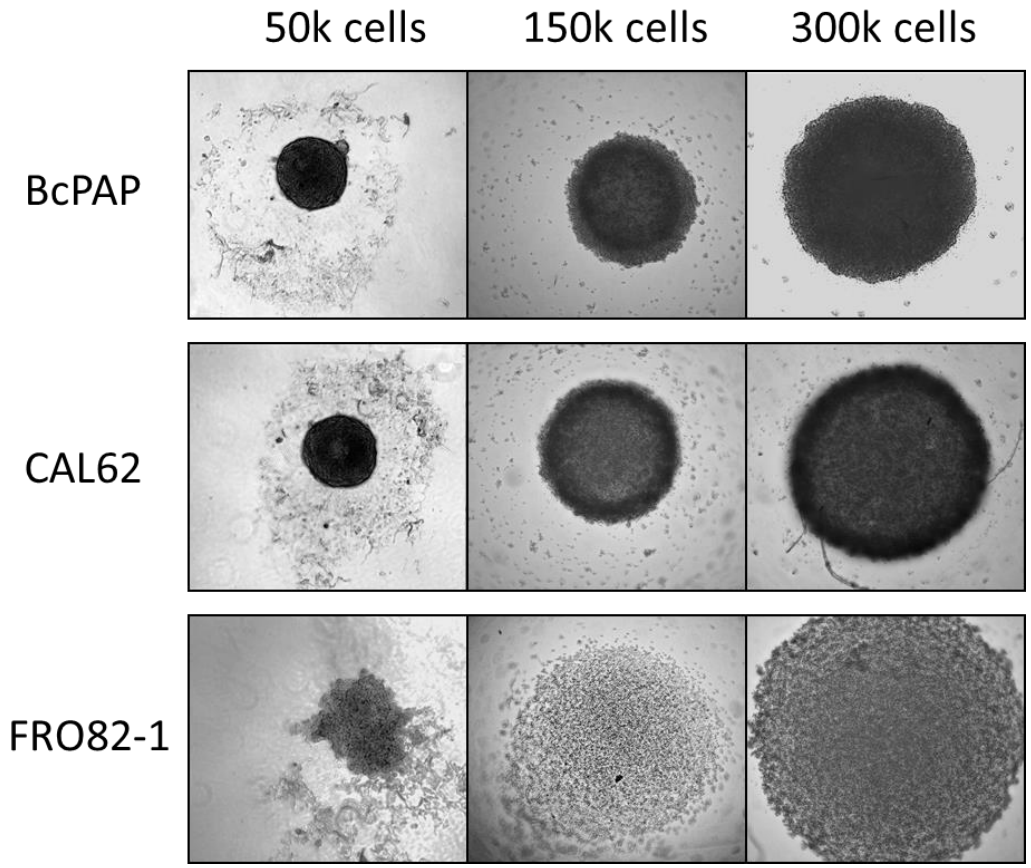

Figure 7. TC cell spheroids and aggregates of different size.
Three-dimensional structures obtained from BcPAP, CAL62 and FRO82-1 after 72 hours from seeding.

When subjected to mechanical solicitation by mixing and pipetting, CAL62 spheroids revealed to be more compact than BcPAP spheroids, but presented an increased incidence of necrotic areas due to a reduced diffusion of nutrients and oxygen from the medium to the inner part of the microtumor.

WST-1 transformation assays were performed on the three-dimensional structures to evaluate the metabolism of their cells, measuring the optical density (OD) of formazan dye formed at 450nm for 180 min (Figure 8). Results indicated that FRO82-1, that does not produce spheroids, are much more proliferative than the other cell lines, suggesting that the more malignant cell type has a higher glucose and lactate metabolism. For BcPAP and FRO82-1, the spheroids/aggregates made seeding 300’000 cells/well showed a decreased proliferation caused by a quick consumption of nutrient by the elevate number of cells. Due to this reason,

in the successive experiments, 3D cultures were produced seeding a maximum of 150'000 cells/well.

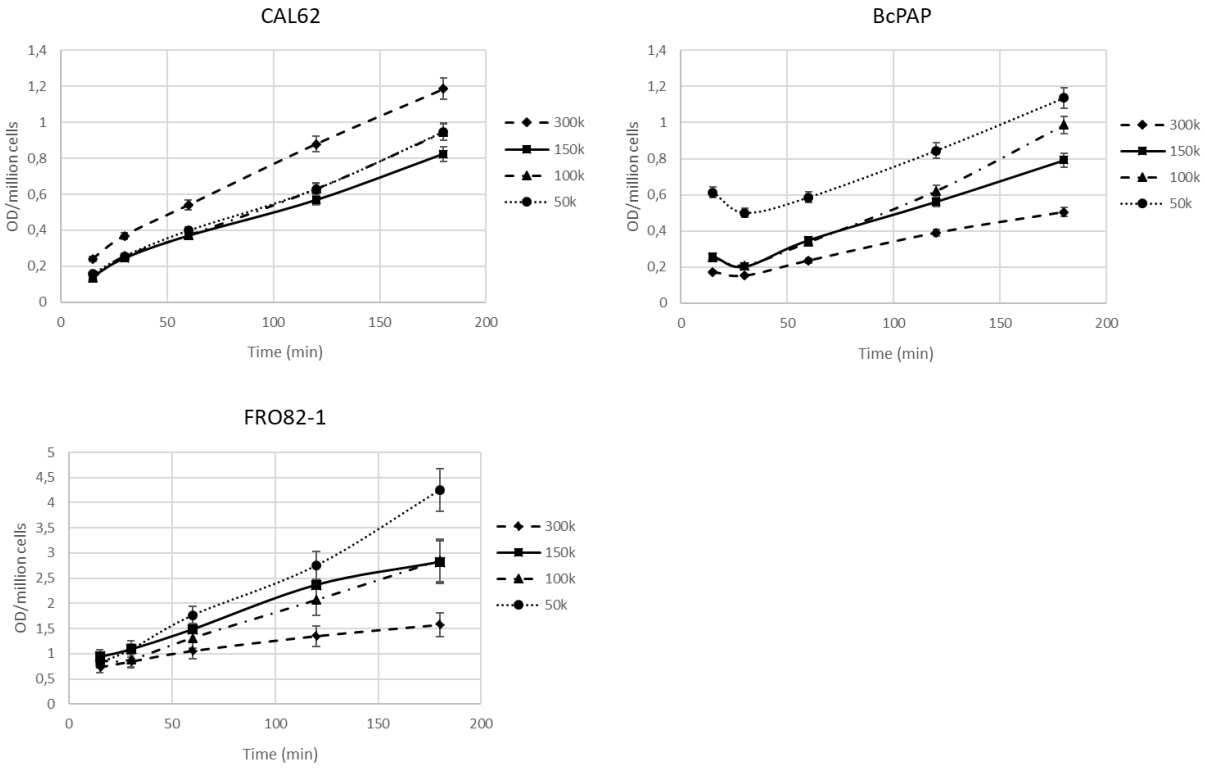

Figure 8. WST-1 assay results for three-dimensional cell cultures.
WST-1 assay shows that spheroids (CAL62 and BcPAP) have a lower proliferation than aggregates (FRO82-1). Cultures obtained seeding 150'000 or 100'000 cells presented a similar proliferation index.

5.2 Characterization of TC cell lines

The characterization of the selected TC cell lines via WB and PCR was performed to assess and compare the expression of Gal3 and NIS in a controllable *in vitro* system, for both monolayer and three-dimensional cultures, and to evaluate the degree of dedifferentiation by TTF-1 expression (Choi et al. 2005). In all the analyses the GAPDH protein and gene expressions were used as internal standard.

WB on the cell lysates presented weak TTF-1 double bands at 40 kDa, confirming a non-complete loss of the thyrocyte phenotype (Figure 9A). As already reported, the differentiated TC cell line BcPAP present expression of TTF-1 (Lopez-Campistrous et al. 2016) as well as the anaplastic cell line CAL62. TTF-1 bands of FRO82-1, although present, are very weak,

confirming a greater degree of dedifferentiation, which is correlating to the increased metabolism measured during 3D cell culture and *in vivo* due to the fast growing rate (see section 5.10).

The expression of Gal3, revealed by a band at 31 kDa, was positive for all 2D and 3D tumor cell lysates (Figure 9A). The relative signal density for spheroids lysates showed an increase of ~38% comparing with the monolayer cells (Figure 9B, left).

Bands at 68 kDa confirmed the expression of NIS, although weaker in comparison to the Gal3 bands, the relative signal density was stronger for the FRO82-1 and BcPAP lysates than for CAL62 cells, with minimal differences between 2D and 3D cultures (Figure 9B, right).

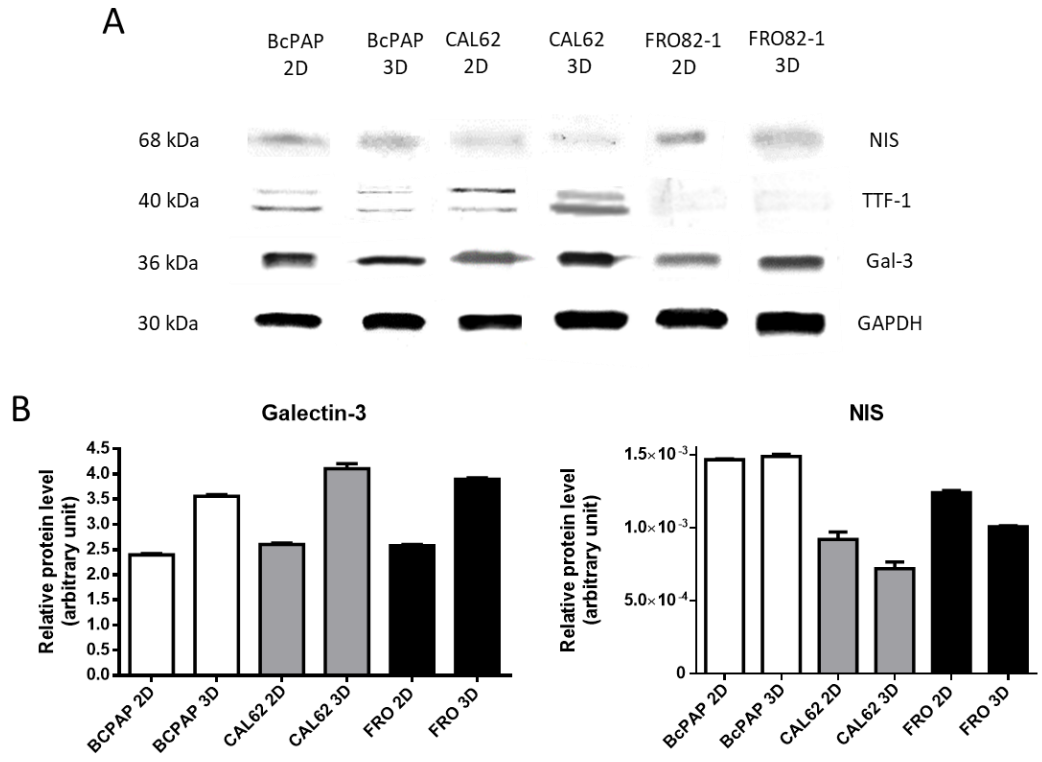

Figure 9. 2D and 3D cell cultures characterization via WB.

(A) Bands separation of cell lysates and (B) results obtained via densitometric analysis of bands correlated to Gal3 and NIS expression using the software imageJ. Data were normalized for the value of GAPDH.

cDNA oligomers from TC cells and healthy thyrocytes, cloned from RNA specific sequences from Gal3 and NIS genes, were amplified via PCR and run on 1% agarose gel (southern blot).

The resulting bands and the subsequent densitometric analysis confirmed the enhanced mRNA encoding for Gal3 expression in TC cells, that is almost absent in healthy thyroid tissues (Figure 10A), with an upregulation in the spheroids (Figure 10B, left).

The expression of NIS resulted considerably reduced if compared with thyrocytes, presenting negligible variances between monolayers and spheroids (Figure 10B, right).

Gal3 and NIS mRNA expression in 2D and 3D cell cultures were also evaluated via RT-PCR confirming the induction of high level of Gal3 expression in thyroid carcinoma cells compared to normal human thyrocytes (Figure 10C, left). Conversely, NIS expression was detectable only in the RNA deriving from normal human thyrocytes (Figure 10C, right).

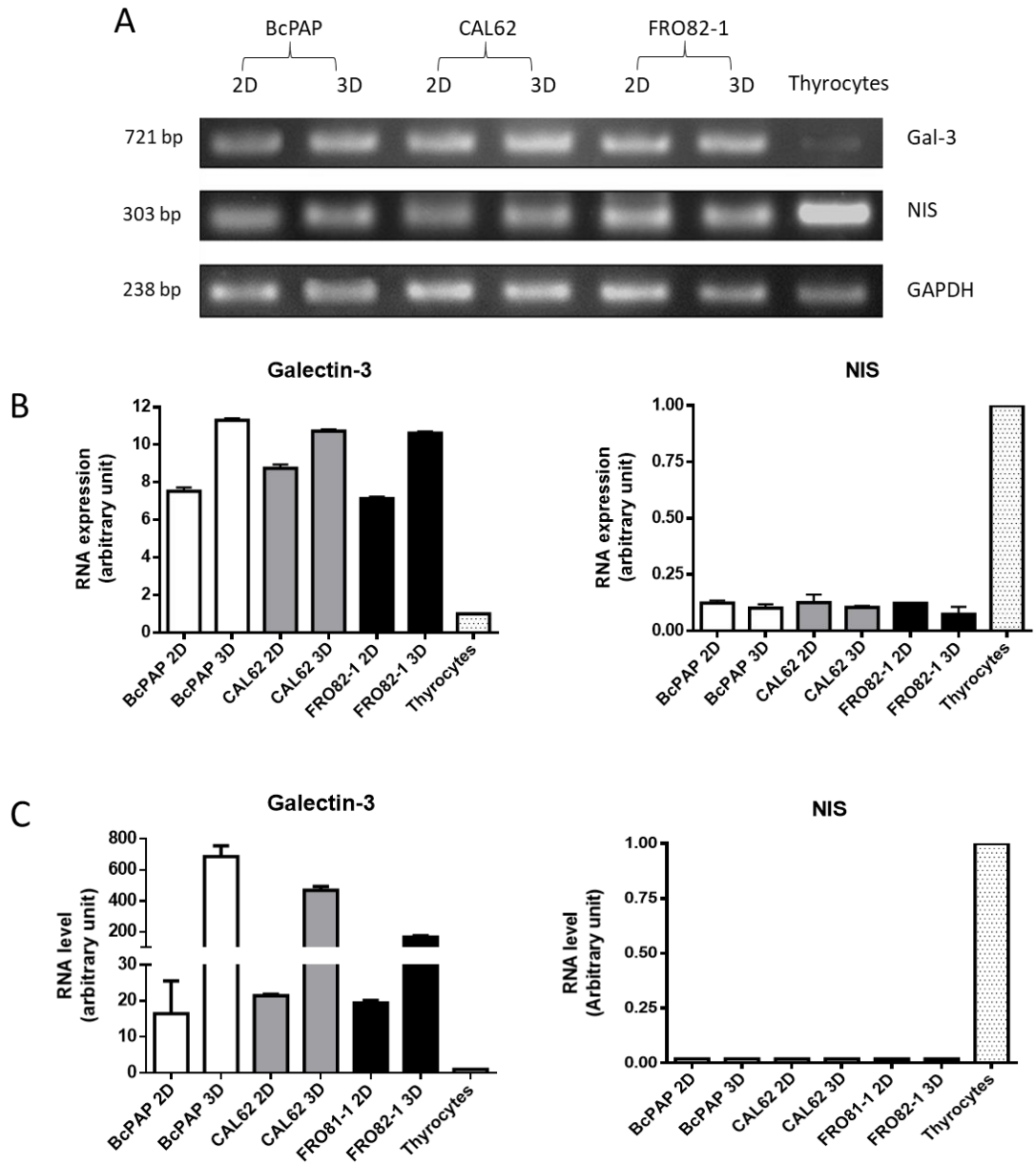

Figure 10. 2D and 3D cell cultures characterization via PCR and RT-PCR.

(A) Electrophoretic separation of cDNA encoding for Gal3 and NIS. (B) Results of the densitometric analysis normalized for the value of GAPDH. (C) Data from RT-PCR analyzed using the $\Delta\Delta C_t$ method, using GAPDH as a control gene, and normalizing with the gene expression of thyrocytes.

5.3 Production of the anti-Gal3 F(ab')$_2$ fragment

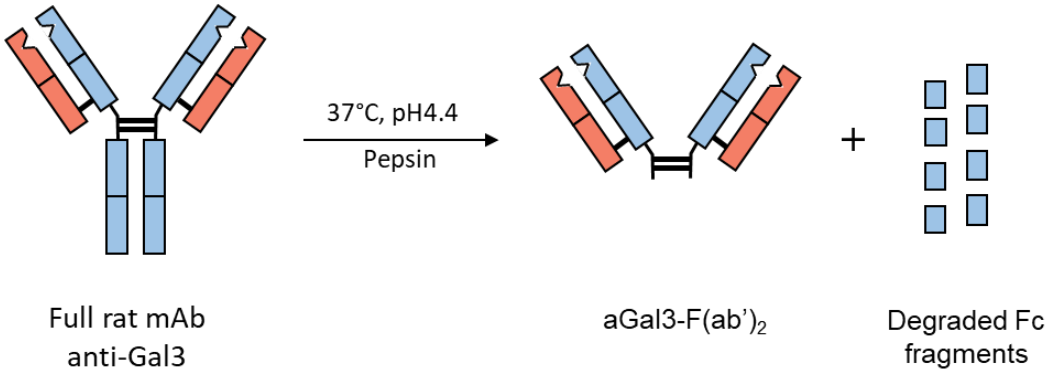

Figure 11. Scheme of production of the aGal3-F(ab')$_2$.

For the production of a F(ab')$_2$ fragment to Gal-3, a rat anti-Gal3 mAb (clone M3/38) was digested with immobilized pepsin in 20 mM sodium acetate (pH 4.4) at 37°C (Figure 11). To investigate in which conditions it is possible to achieve the best yield, the reaction was performed with or without pre-conditioning of the mAb in sodium formate buffer at pH 2.8, as suggested by Stewart and Stanworth (Stewart and Stanworth 1975), before starting the incubation with pepsin for 2 or 4 hours. Quality controls conducted via SE-HPLC showed best results with pre-conditioning step followed by an incubation of 2 hours (Figure 12A). This result shows that preconditioning step is crucial to obtain the digest already after 2 hours of incubation.

The aGal3-F(ab')$_2$ purified via affinity chromatography using a protein G column was analyzed via SDS-PAGE in non-reducing conditions, showing a band at ~120 kDa attributable to F(ab')$_2$ fragments, and in reducing conditions, showing one strong band at ~20 kDa due to light chains and shortened heavy chains (Figure 12B). SE-HPLC chromatograms showed a shift of the main peak from 7.8 min for full mAb to 8.2 min for the aGal3-F(ab')$_2$. The unpurified product presents a peak shoulder at 9.7 min due to Fc fragments that is completely absent after the purification (Figure 12C).

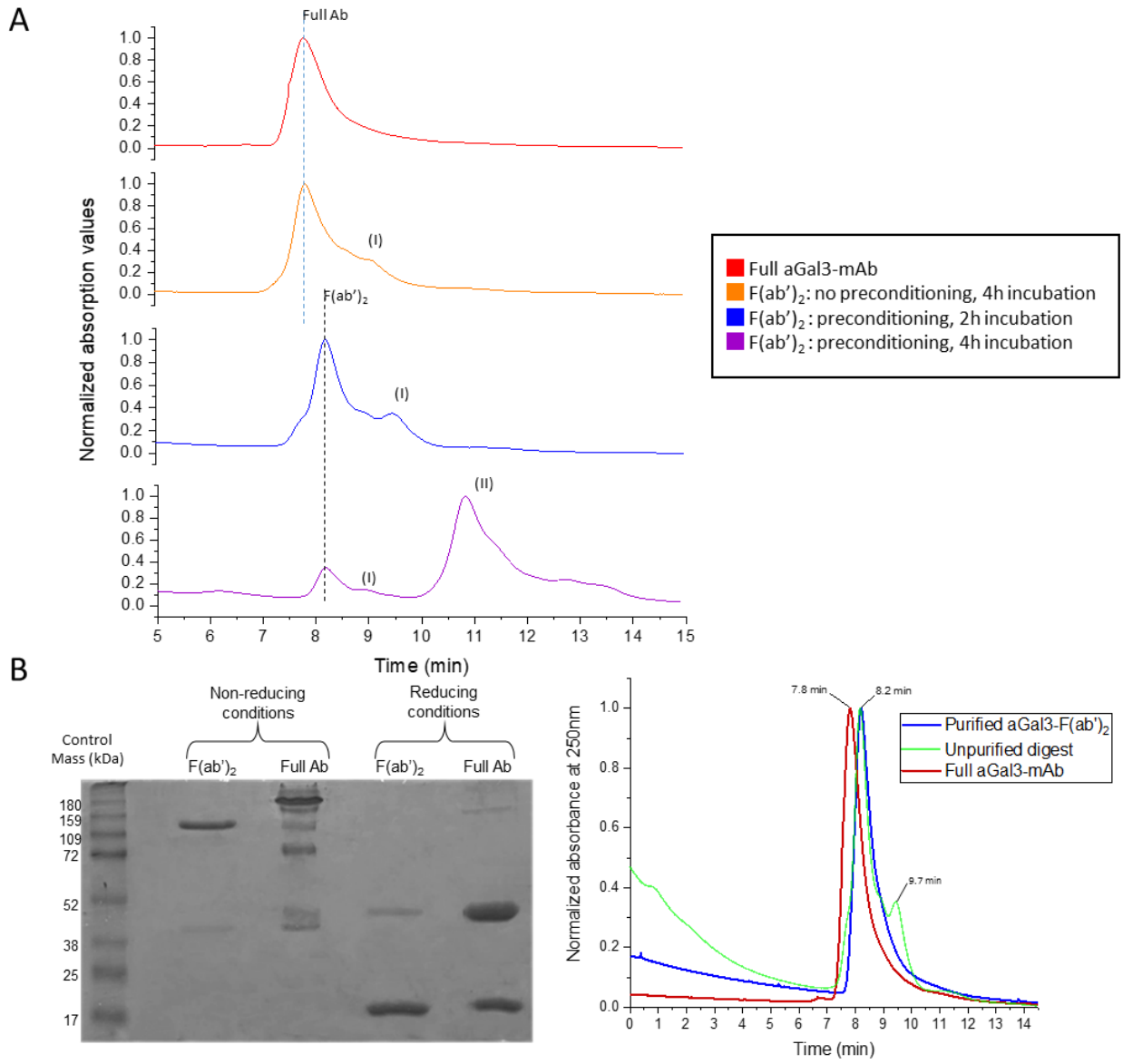

Figure 12. Quality control of the aGal3-F(ab')$_2$ production.

(A) SE-HPLC UV-chromatograms at 280nm of the digests produced in different conditions. Peaks with retention times >9 min are due to Fc fragments or to the complete degradation of the mAb. (B) SDS-PAGE in non-reducing and reducing conditions followed by Coomassie blue staining of the purified aGal3-F(ab')$_2$. (C) Comparison between the SE-HPLC UV-profiles of the purified product with a sample of unpurified reacted mixture. For all the analyses a sample with full aGal3-mAb was injected as control.

5.4 Anti-Gal3 immuno-imaging probes production

5.4.1 Production of fluorescent imaging probes

To perform fluorescence microscopy and FMT imaging, two different probes were produced conjugating the aGal3-F(ab)$_2$ with AlexaFluor488 and Cy5.5 respectively (Figure 13A).

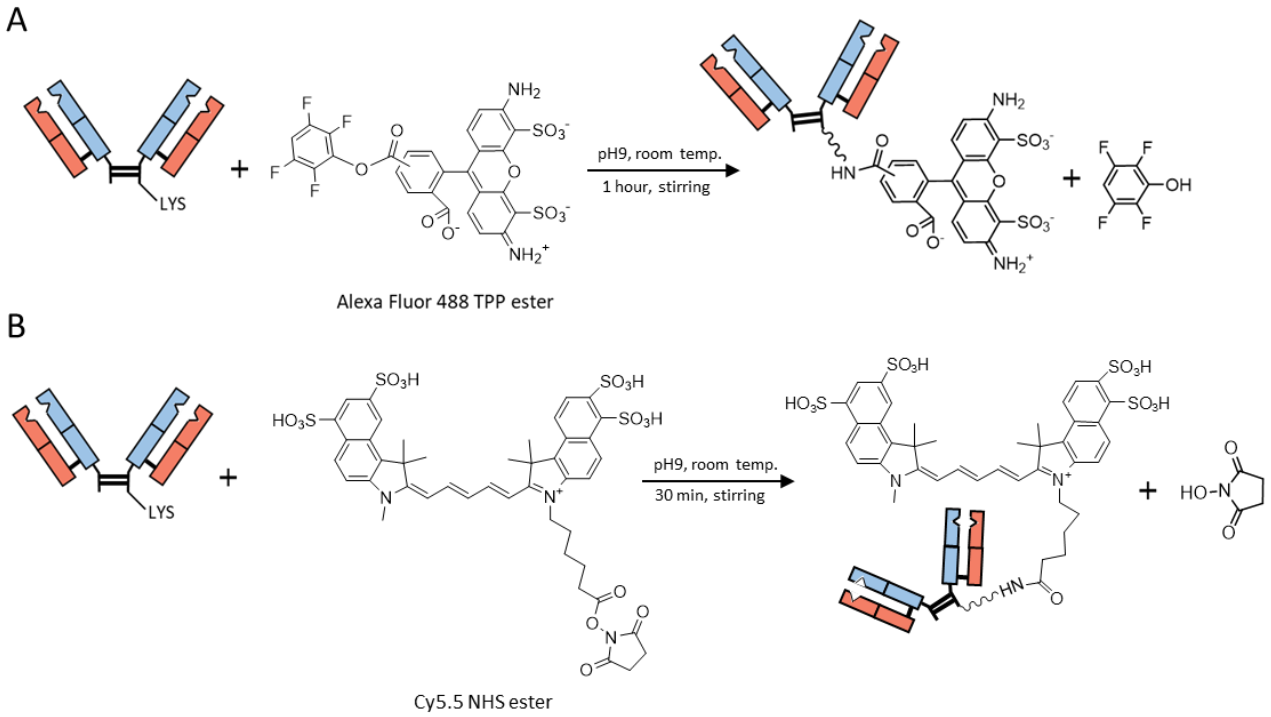

Figure 13. Schemes of the fluorescent probes production.
Summary schemes of the aGal3-F(ab')$_2$ conjugations with (A) AlexaFluor488 and (B) Cy5.5. The dye esters react at slight basic pH with primary amino-groups present on the surface of the antibody fragment.

The products were purified via filtration with a 30 kDa membrane vivaspin, capable to remove all the non-reacted fluorescent dye (mass <<30kDa). The obtained samples were analyzed via spectrophotometer revealing a DOL of 5.0±0.1 and 3.6±0.1, for aGal3-F(ab')$_2$-AF488 and aGal3-F(ab')$_2$-Cy5.5 respectively. Quality controls performed via SE-HPLC confirmed the coherence of the probes fluorescence peak and the UV peak of aGal3-F(ab')$_2$, and no degradation of the samples (Figure 14).

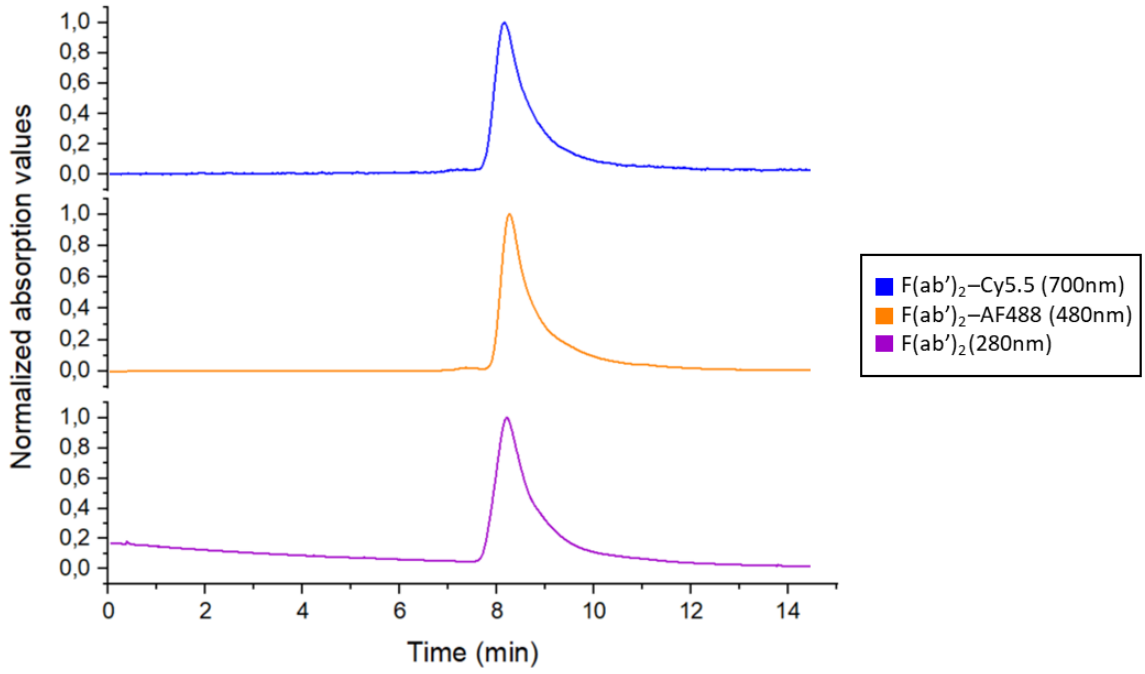

Figure 14. Quality controls on aGal3-F(ab')$_2$-Cy5.5 and aGal3-F(ab')$_2$-AF488.
SE-HPLC chromatograms taken at different wavelength of the aGal3-F(ab')$_2$ and its dye-conjugate derivatives show stability of the products and no significant changes in the size.

5.5 Production of the aGal3-F(ab')$_2$-DFO-^{89}Zr radiotracer

The production of the radiotracer for PET-imaging was performed in two steps as reported by Holland et al. (Holland et al. 2010) with slight modifications. As a first step, the aGal3-F(ab')$_2$ was conjugated with DFO by reaction of a primary amine of the protein (lysine residue) with DFO-Bz-NCS, forming a thioamide bond. The product (aGal3-F(ab')$_2$-DFO) was successively purified via chromatography using a size exclusion PD-10 column. Finally, the aGal3-F(ab')$_2$-DFO conjugate was labeled with the radionuclide ^{89}Zr via transchelation from an ^{89}Zr-oxalate complex. To remove radionuclide excess, the reaction product underwent a second purification via PD-10 column. The schematic overview of the procedure is illustrated in Figure 15.

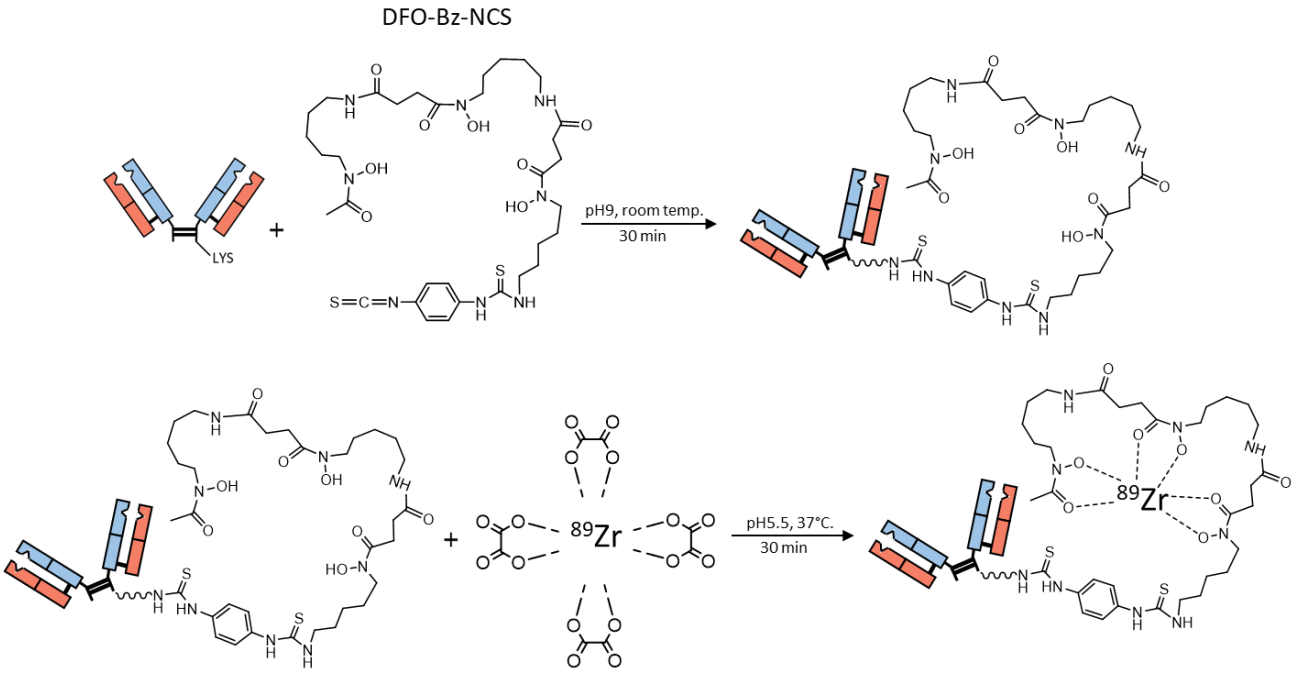

Figure 15. Overview of the aGal3-F(ab')$_2$-DFO-^{89}Zr production.

During the first step (above), DFO-Bz-NCS reacts with a lysine residue of the antibody fragment at basic pH forming a thioamide covalent bond. In the second step (below), after the neutralization of the ^{89}Zr-oxalate solution, the conjugate (aGal3-F(ab')$_2$-DFO) is labeled with the radionuclide in mild conditions of pH and temperature.

The number of accessible DFO molecules conjugated with the aGal3-F(ab')$_2$ were assessed via radiometric isotopic dilution assay as indicated by Holland et al. (Holland et al. 2010) after the conjugation step. Non-linear regression analysis outcomes revealed an average of 1.3±0.2 accessible chelates per antibody fragment (Figure 16A).

The final product was analyzed via radio-iTLC and run in citrate buffer before and after the purification, showing an elevate incorporation of the radionuclide (radiolabeling yield of 96±1%) and a radiochemical purity of 98.5±0.5% (Figure 16B) with a calculated specific activity of 29.6 ± 2.0GBq/µmol.

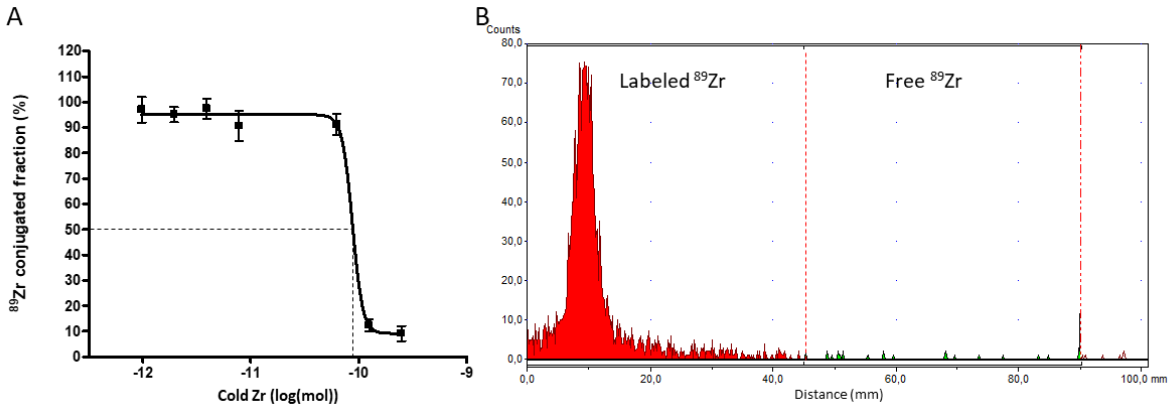

Figure 16. Control tests performed during the production of the aGal3-F(ab')$_2$-DFO-^{89}Zr radiotracer.

(A) Resulting plot of the radiometric isotopic dilution assay performed on aGal3-F(ab')$_2$-DFO. (B) iTLC profile of purified aGal3-F(ab')$_2$-DFO-^{89}Zr, presenting a peak at Rf = 0.1, as expected for the incorporated ^{89}Zr, corresponding to the 98.5% of the total measured activity.

Further analyses, to verify correspondence with the mass of the unlabeled aGal3-F(ab')$_2$ and tracer integrity, were performed via SDS-PAGE followed by an autoradiography and via SE-HPLC (Figure 17A and 17B).

The aGal3-F(ab')$_2$-DFO-^{89}Zr probe showed high stability up to 4 days at 37°C in human serum and in sodium citrate buffer pH 5.5 with 5g/l of gentisic acid (storage solution), indicating a product suitable for *in vivo* studies. Transchelation occurs in excess of DTPA (50mM), with a constant loss of ^{89}Zr up to 70% circa at the end of the investigated time window (Figure 17C).

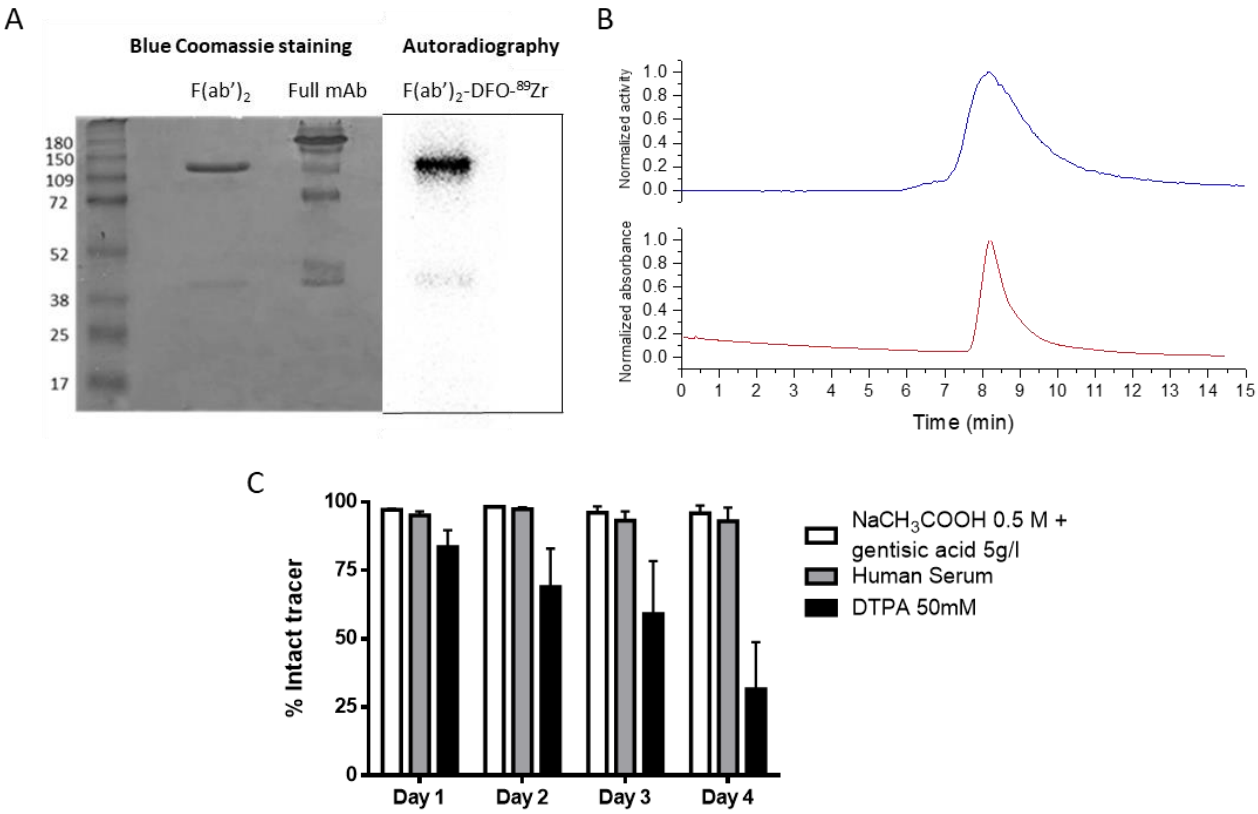

Figure 17. Characterization of the aGal3-F(ab')$_2$-DFO-^{89}Zr radiotracer.

(A) SDS-PAGE runs of the anti-Gal3 F(ab')$_2$ fragment and the radiotracer, using the full mAb as a control, performed in non-reducing conditions. Both the analytes showed a band at 120kDa indicated a non-degraded product, and a weak band (<2% of the total signal) at 45kDa for degraded chains. (B) Association between the radioactivity profile of aGal3-F(ab')$_2$-DFO-^{89}Zr (above) and the UV chromatogram at 250 nm (below) of aGal3-F(ab')$_2$ obtained via SE-HPLC, both showed a peak at 8.2 min. (C) Stability of the radiotracer in different storage solutions. Data are obtained via iTLC performed at different time points on silica gel strips, eluting with DTPA 50mM, and presented as mean±SD. Analysis were repeated at least three times in triplicate.

5.5 Fluorescence microscopy studies

The binding of the antibody fragment on the selected cell lines and corresponding spheroids was evaluated via fluorescence microscopy. In particular, the interaction with the spheroids was investigated to characterize the penetration of the probe in the inner layers.

5.5.1 Determination of the dissociation constant of aGal3-F(ab')$_2$-AlexaFluor488

As a preliminary step for fluorescence microscopy studies, the K_d of the aGal3-F(ab')$_2$-AlexaFluor488 conjugate was determined on the thyroid cancer cell line BcPAP via FACS analysis. A constant number of cells were incubated in different concentration of tracer (from $5x10^{-8}$ to $5x10^{-11}$M) for one hour and then analyzed. To calculate and subtract the unspecific signal, the tests were repeated with an excess of unlabeled aGal3-F(ab')$_2$.

The K_d value equal to 12±1nM, extrapolated via non-linear regression curve of the mean fluorescence intensity (see Figure 18) and compared to the dissociation constant of the aGal3-mAb, indicates a minimum loss of binding affinity (D'Alessandria et al. 2016).

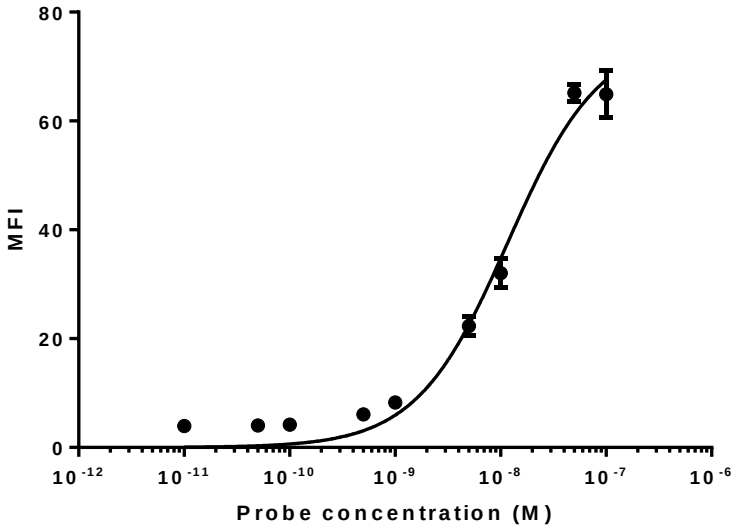

Figure 18. Binding affinity of the aGal3-F(ab')$_2$-AlexaFluor488 to BcPAP.
Affinity assay plotted as MFI values, subtracted from the unspecific binding, on logarithm of the aGal3-F(ab')$_2$ concentration. Results presented as a mean±SD, of three repetitions.

5.5.2 Fluorescence microscopy tests on monolayer cultures

Fluorescence microscopy studies were performed using a Biorevo BZ-9000 microscope with 20x and 40x magnification lenses after 1 hour of incubation with different concentration of fluorescent probe at room temperature. The best images were obtained incubating in 5µg/ml, presenting an intense signal with a low background.

For all the cell lines considered, the fluorescent emission is detectable on the membrane, but also in the cytoplasm (Figure 19A), indicating an internalization of the protein (see paragraph

5.6.3). The signal found on the membrane is inhomogeneous, organized in areas that presents high expression visualized as spots (Figure 19B), this can be a consequence of the Gal3 polymerization as well as its secretion/uptake mechanism and interaction with extracellular proteins (Baptiste et al. 2007).

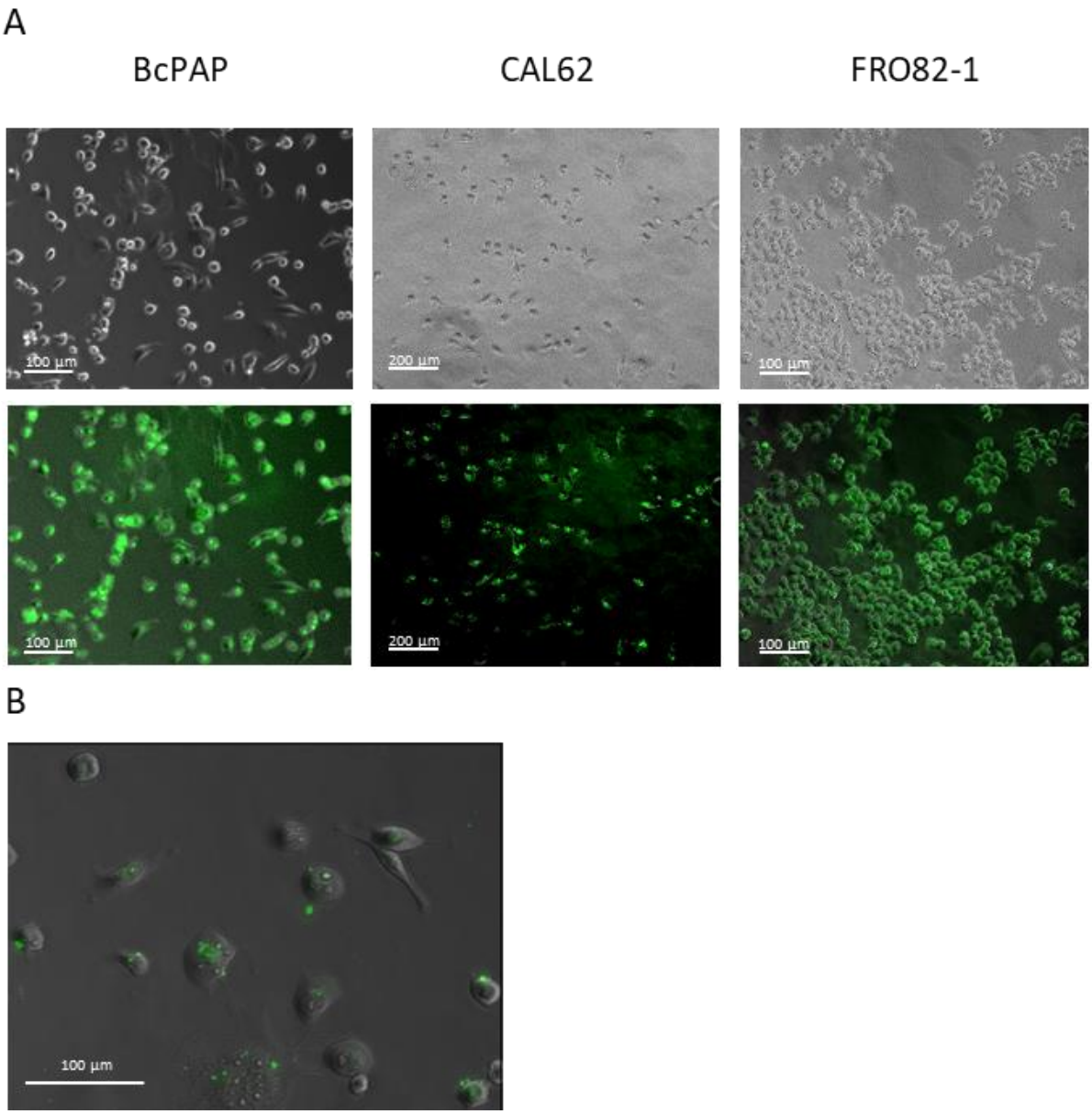

Figure 19. Imaging of the monolayer cell cultures via fluorescence microscopy.
(A) Images of the monolayer cell cultures after 1 hour of incubation in PBS 5 µg/ml aGal3-F(ab')$_2$-AlexaFluor488. Pictures are captured by contrast phase (above), and the overlay with the fluorescence signal (below). (B) Focus of the fluorescence signal structured in high expression spots on BcPAP cells. The pictures were taken with 20x and 40x lenses, with an acquisition time of 1/125 sec for the fluorescence.

5.5.3 Fluorescence microscopy tests on 3D cultures

The transportation of a drug is considered to be a combination of diffusion and convection mechanisms (Thurber, Schmidt, and Wittrup 2008). While the diffusion depends from Bownian motion, intrinsically random, the convection is correlated to the interstitial fluid pressure. In contrast to healthy tissues, the tumor scarce draining from lymph vessels, the high permeability of blood vessels and the high cell density lead to an increased interstitial fluid pressure that cause a convection limited to the tumor edges.

These reasons give the rationale for the use of spheroids in *in vitro* tests, which permit a correct study of the aGal3-F(ab')$_2$ penetration in tumor-like structures giving preliminary results to consider the use of a drug *in viv*o.

The dense BcPAP spheroids, produced as seen in paragraph 4.1.3, were incubated in PBS with aGal3-F(ab')$_2$-AlexaFluor488 at 37°C and analyzed by fluorescence microscopy at 1, 2, 5 hours (Figure 20A). For spheroids with a diameter about 1mm the images showed a quick complete penetration in the inner layers after 5 hours of incubation, indicating that, in absence of necrosis, the distribution of the aGal3-F(ab')$_2$ is not limited to the edges of the microtumor. The dynamic of antibody fragment penetration is mostly guided by the aforementioned transportation processes, but the phenomena of Gal3 internalization and externalization may contribute to an active improved tumor perfusion.

The signal visualized after 24 hours of incubation was stronger for more compact spheroids (BcPAP and CAL62) than for cell aggregates (FRO82-1) (Figure 20B). The cell lines forming compact spheroids showed a higher signal from the extracellular matrix, hence resulting in a total enhanced brightness of the microtumor. A marked reduction of the fluorescent signal was observed for the inner area of large CAL62 spheroids with a diameter >1mm, this can be attributed to the necrosis, as evidenced by histological staining (caspase-3, data not shown).

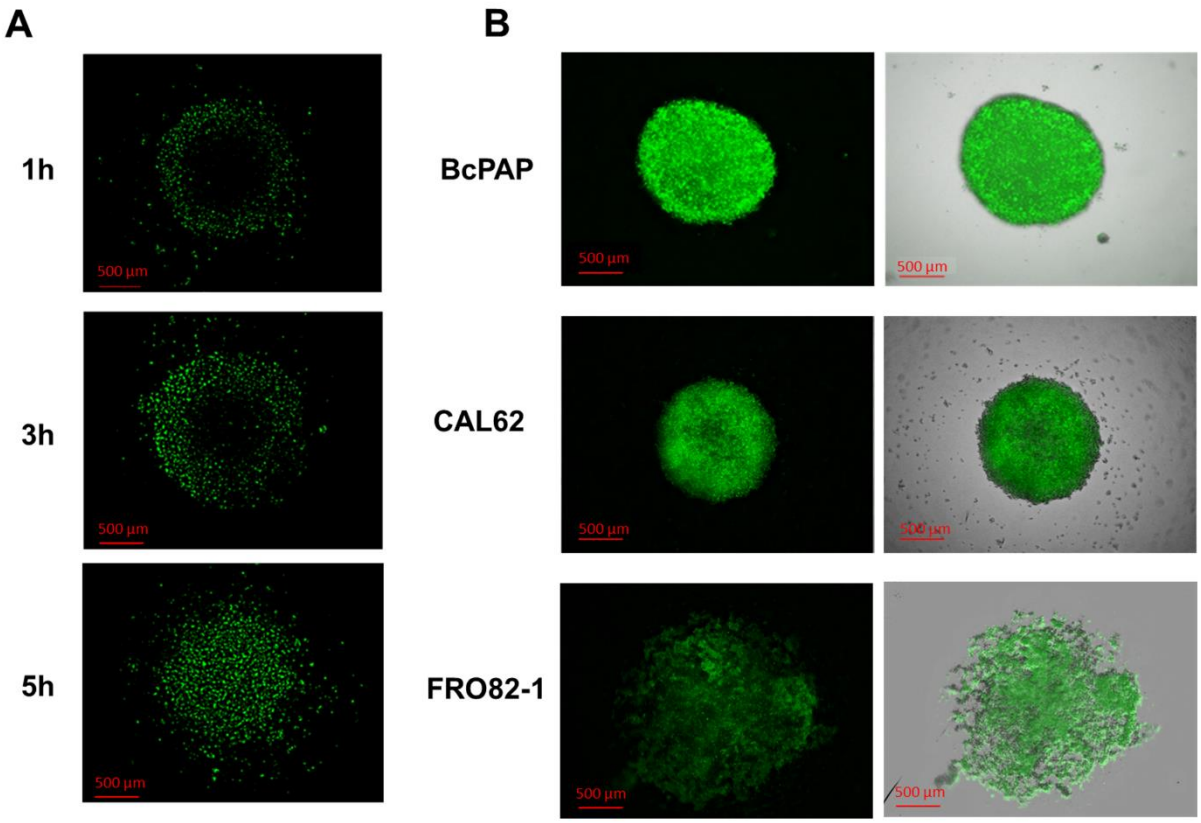

Figure 20. Fluorescence microscopy of aGal3-F(ab')$_2$-AlexaFluor488 binding tests on 3D cultures.

(A) Time dependent penetration of aGal3-F(ab')$_2$-AlexaFluor488 into BcPAP tumor spheroids during 5 hours of incubation. (B) Fluorescence (left) and overlay confocal plus fluorescence microscopy (right) images of BcPAP, CAL62 and FRO82-1 spheroids acquired after 24 hours of incubation with 5µg/ml F(ab')$_2$-AlexaFluor488. CAL62 tumor cells formed compact spheroids, with a central necrotic area. Images were captured using a Biorevo 9000E (Keyence) digital microscope equipped with a Nikon Plan Fluor 10x lens.

5.6 *In vitro* studies of aGal3-F(ab')$_2$-DFO-^{89}Zr on TC cell and comparison with ^{124}I

5.6.1 Assessment of the aGal3-F(ab')$_2$-DFO-^{89}Zr immunoreactive fraction

Modifications of the antibody structure due to peptide digestion and conjugation can determine a reduction of the binding properties, even when the binding site is not directly involved in the processes, because of steric hindrances and changes in the three-dimensional arrangement (Kukis et al. 1995). Lindmo immunoreactive test determines the fraction of antibody specifically bound to the antigen *in vitro* in conditions representing infinite antigen excess and can be used to assess changes in the binding affinity after the modification of an antibody.

For the test, a constant concentration of radiotracer was incubated with an increasing number of cells with or without the presence of non-labeled aGal3-F(ab')$_2$-DFO to estimate the non-specific binding.

The immunoreactivity of the full aGal3-mAb was previously assessed by D'Alessandria et al. and it revealed to be 75% (D'Alessandria et al. 2016). aGal3-F(ab')$_2$-DFO-^{89}Zr showed an immunoreactivity of 75±2% (Figure 21), confirming that the pepsin digestion and the procedures for labeling did not affect the binding specificity.

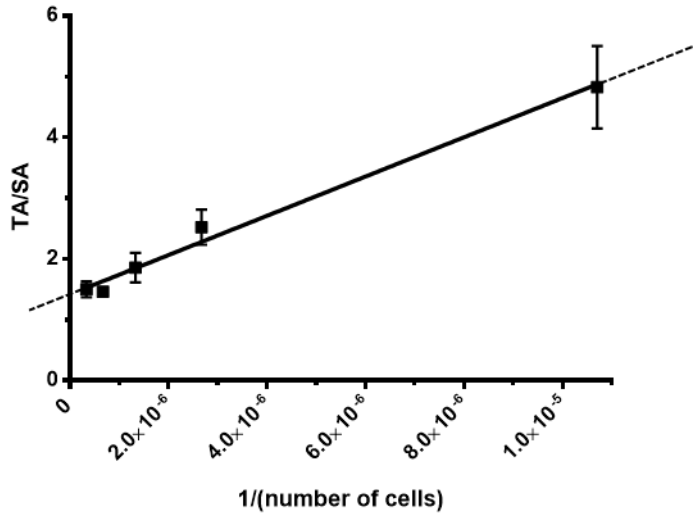

Figure 21. Determination of the immunoreactive fraction of aGal3-F(ab')$_2$-DFO-^{89}Zr.
The immunoreactivity of the radiotracer was calculated plotting a double inverse graph (total/bound) activity versus (1/[normalized number of cells]), the value of the immunoreactive fraction was determined by the linear regression curve intercept on ordinate axis (1/Y intercept). The data, presented as mean±SD, was collected repeating the measurement three times each cell line.

5.6.2 Binding affinity of aGal3-F(ab')$_2$-DFO-^{89}Zr on TC cell lines

The dissociation constant (K_d) is the most indicative parameter to describe the quality the antigen targeting of an antibody, taking into account also the conditions of equilibrium.

The K_d of the radiotracer was determined via binding affinity saturation assay on selected cell lines. A constant number of cells was incubated with an increasing concentration of aGal3 F(ab')$_2$-DFO-^{89}Zr reaching the saturation of the blinding sites and the total bound activity was measured via gamma-counter. To calculate the specific bound activity, an assay in presence

of a 100-fold excess of non-labeled aGal3-F(ab')$_2$-DFO was performed. The results were plotted in a graph of the activity (CPM) versus the concentration of the tracer, extrapolating the K_d value as EC50 with a non-linear regression curve (Figure 22). The aGal3-F(ab')$_2$-DFO-^{89}Zr radiotracer revealed a K_d in the subnanomolar range of 0.39±0.02nM.

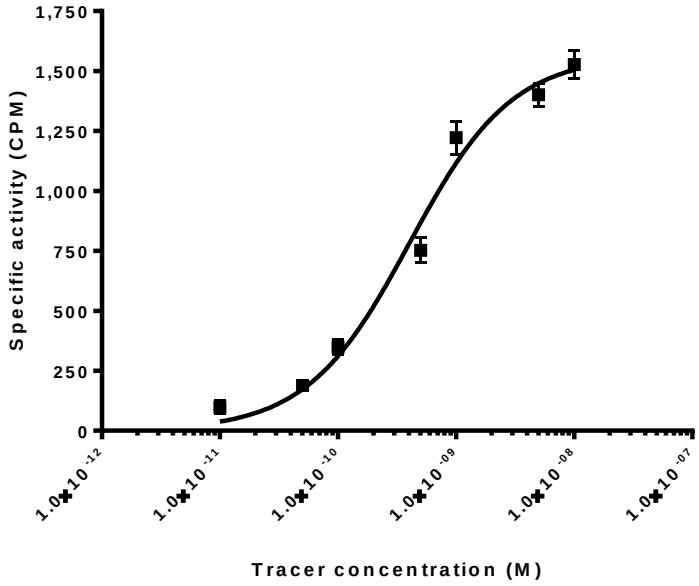

Figure 22. Determination of the K_d of aGal3-F(ab')$_2$-DFO-^{89}Zr on TC cells.
Representative graph of the binding affinity test of ^{89}Zr-Df-aGal3-F(ab')$_2$ on monolayer TC cells. The K_d values were determined by non-linear regression analysis plotting the concentration of radiotracer versus the specific activity. The data, presented as mean±SD, was collected repeating the measurement three times each cell line.

5.6.3 Internalization in TC cell lines of aGal3-F(ab')$_2$-DFO-^{89}Zr

Fluorescence microscopy studies already suggested the internalization of the aGal3-F(ab')$_2$ (paragraph 5.5.2). The occurrence of endocytic processes plays a key role for diagnostic imaging, increasing the half-life of the tracer in the target compartments and then leading to a more accurate and high contrast imaging.

To evaluate the internalization of the radiotracer in thyroid cancer cells, detached BcPAP cells were incubated with a constant concentration of aGal3-F(ab')$_2$-DFO-^{89}Zr for one hour on ice, to allow the binding on the membrane. Then, after removing the excess of tracer, the incubation was resumed at 37°C, measuring the activity internalized, secreted and bound to membrane

at different time points. The results showed a constant decrease of radiotracer bound to the membrane reaching a plateau after the first 120 min. To this trend corresponds an increase of the internalized fraction, up to 70% of the total activity, and a secretion in the surrounding medium (up to 20% of the total activity), as explained by the uptake and secretion mechanism involving Gal3 (Baptiste et al. 2007). It is demonstrated that Gal3 is constantly secreted, externalized and re-internalized with the function of modulator of cellular adhesion, with an enhancement of this process in detached cells. It is reasonable to assume that *in vivo* the secretion mechanism is partially inhibited by adhesion, and, as shown via fluorescence microscopy (paragraph 5.5.3), Gal3 is mostly secreted in the extracellular matrix, where it is uptaken by other TC cells.

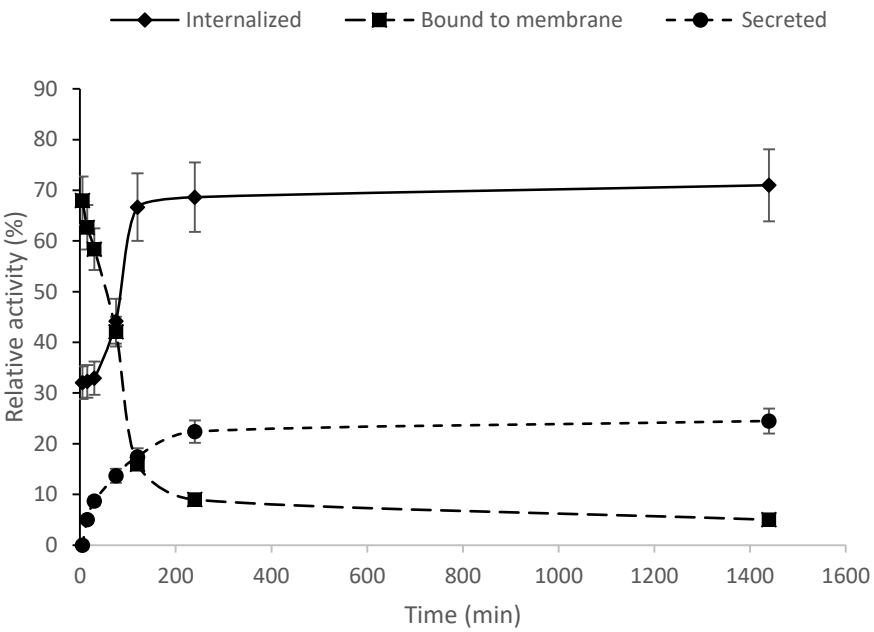

Figure 23. Evaluation of the aGal3-F(ab')$_2$-DFO-^{89}Zr internalization in TC cells.
Internalization and secretion of aGal3-F(ab')$_2$-DFO-^{89}Zr in the representative TC cell line BcPAP. The relative activity corresponds to the activity in the different fractions as a percentage of their sum. The data, presented as mean±SD, was collected repeating the measurement three times.

5.6.4 aGal3-F(ab')$_2$-DFO-^{89}Zr and radioiodine accumulation studies in TC cells

Further accumulation studies were performed on 2D and 3D cells as a crucial part of the preparation for *in vivo* tests. In particular, to perform an evaluation of residual NIS-mediated

uptake in TC cells and, on the other hand, to assess any trend in accumulation of aGal3-F(ab')$_2$-DFO-^{89}Zr on spheroids.

The ^{125}I specific uptake in monolayer cultures and tumor spheroids was measured as established by Spitzweg et al. (Spitzweg et al. 1998), incubating the cells with 2µCi of Na^{125}I (Figure 21A). It revealed to be strongly dependent on the differential NIS expression already evidenced via western blot and PCR analysis (section 5.2). The PTC cell line BcPAP showed the highest uptake for monolayers. Among dedifferentiated TC cells, while CAL62 presented an expected lower accumulation, FRO62-1 exhibited the highest signal among 3D cultures, probably due to a wider surface in direct contact with the medium. A specular Iodine-125 accumulation was measured on tumor spheroids (Figure 21B).

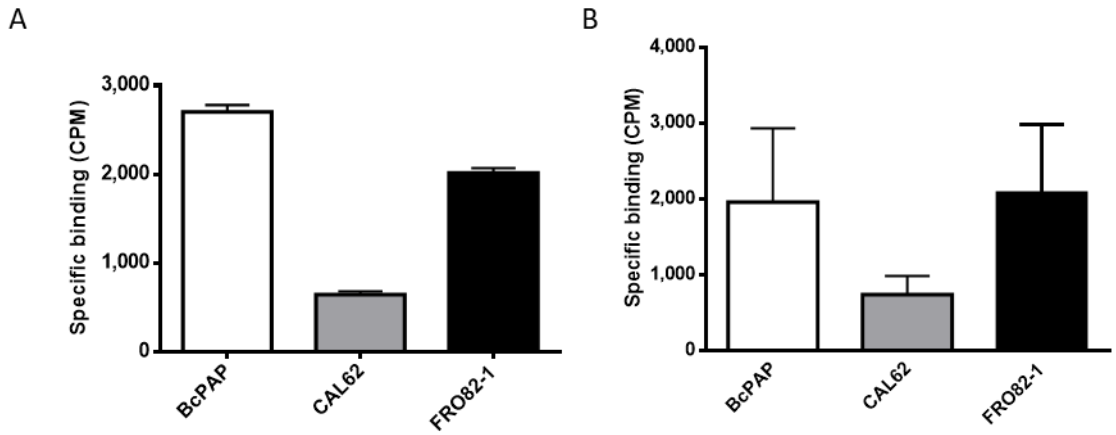

Figure 24. Accumulation studies of ^{125}I on TC cells.

Plots of the activity associated to each cell line obtained incubating with 2 µCi Na^{125}I monolayer (A) and 3D (B) cell cultures for 30 min at 37°C. Spheroids and aggregates were obtained seeding 150'000 cells/well. All the measurements are presented as mean±SD of three repetitions.

Further experiments on ^{89}Zr-DFO-aGal3-F(ab')$_2$ accumulation on TC cells confirmed the affinity and specificity, showing a size-dependent binding to tumor spheroids. The signal associated to FRO82-1, that exhibit also the quickest growth (see section 5.8), was consistently higher than the other cell lines (Figure 22A). A lower signal was measured for dense spheroids, due to a slower diffusion of the tracer inside the microtumor and to the presence of necrotic areas in the inner layers (Figure 22B).

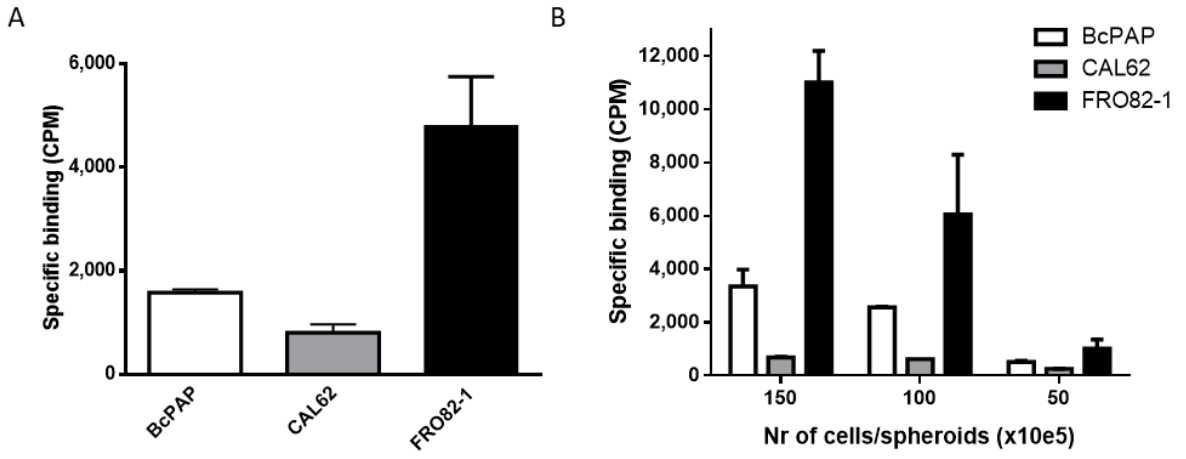

Figure 25. Accumulation studies of aGal3-F(ab')$_2$-DFO-^{89}Zr on TC cells.

In vitro assessment of the accumulation of aGal3-F(ab')$_2$-DFO-^{89}Zr on monolayer (A) and 3D (B) cell cultures. The cells were incubated with 1x10^{-8} M tracer for 2 hours on ice. All the measurements are presented as mean±SD of three repetitions.

5.7 Workflow for the *in vivo* immuno-PET imaging of TCs

The *in vitro* characterization of aGal3-F(ab')$_2$-DFO-^{89}Zr radiotracer revealed that the radiotracer possesses binding affinity and specificity for Gal3, accumulation studies showed an elevated and size-dependent uptake of the radioactive probe in microtumors, confirming our initial thesis. This data proved the suitability of the aGal3-F(ab')$_2$ derivative for *in vivo* studies on animal models.

Figure 26 shows the experimental set up for the validation of our method in pre-clinical tests. As a first stage orthotopic xenograft models, for each selected TC cell line, were established on CD1-Foxn1$^{nu/nu}$ nude mice (see section 5.7). The tumor cells were transplanted into the left thyroid lobe (D-x), and the growth was monitored until a diameter of half centimeter, considering this moment the day 0 (D0). For each cell line, 10 mice were placed in the group I, for the testing of aGal3-F(ab')$_2$-DFO-^{89}Z, and 3 mice in the group II, for a head to head comparison of the radiotracer with radioiodine (^{124}I) PET imaging. Mice of the group I were injected with aGal3-F(ab')$_2$-Cy5.5 already on D0, to verify the expression of Gal3 in the tumor via FMT 48 hours later (D+2). Seven days after D0 (D+7), mice underwent injection of aGal3-

F(ab')$_2$-DFO-^{89}Zr radiotracer with consequential PET/CT imaging after 48 hours (D+9), then they were sacrificed for biodistribution, *in vivo* stability and immunohistochemical studies.

The mice belonging to the group II did not undergo to FMT imaging, but were injected with radioiodine on D+7 and were scanned one hour post injection via PET/CT. As the animals from group I, they were killed for *ex vivo* studies.

For each group of animals, a subgroup of healthy animals was tested as a control.

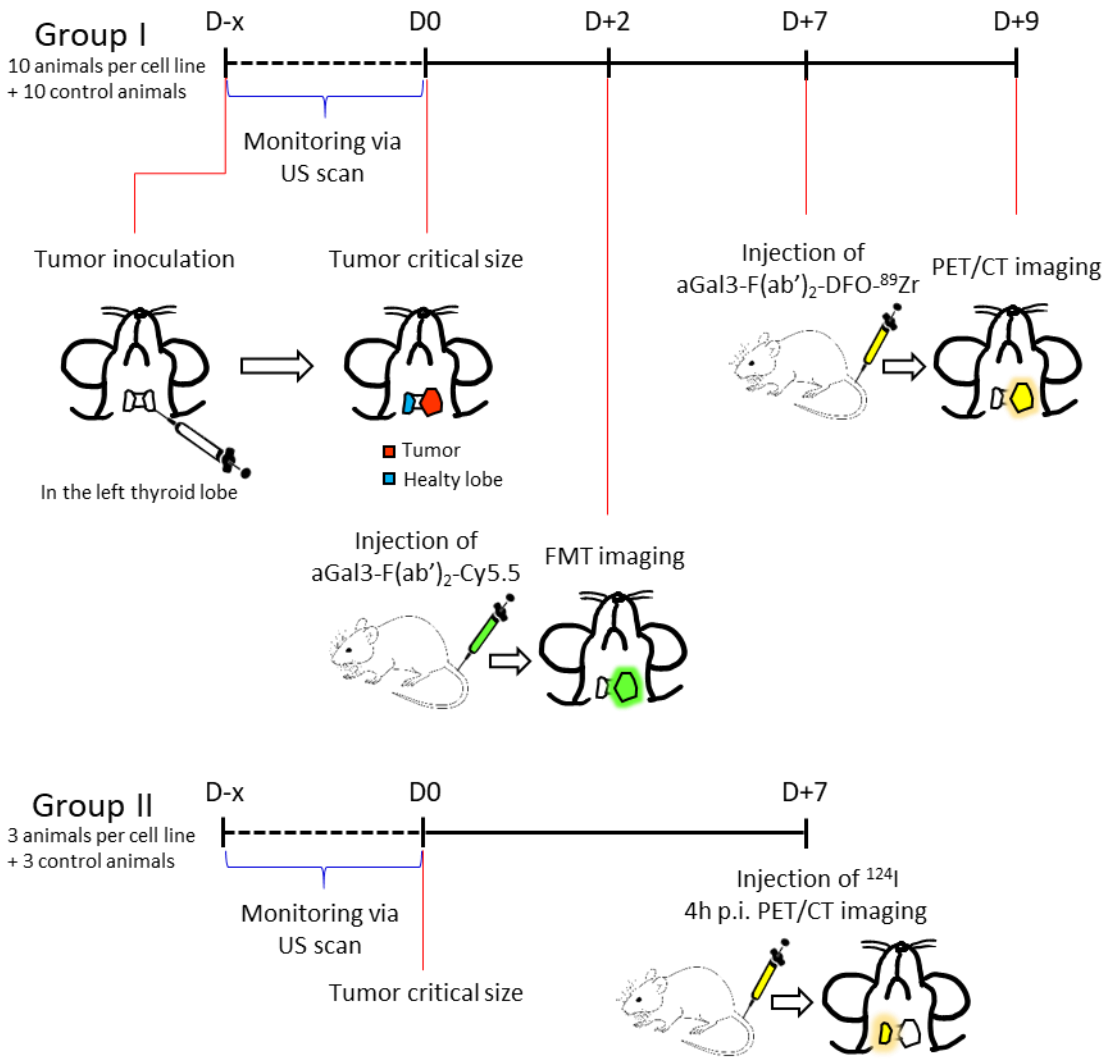

Figure 26. Workflow for the *in vivo* experiments and head to head comparison with radioiodine PET imaging.

5.7 Establishment of the TC orthotopic xenograft model

Pre-clinical tests on animals are a crucial stage in the pharmaceutical development, being a gateway for the first-in-man studies. For this reason, reliable outcomes are necessary to define characteristic, behavior and potential of a drug *in vivo*. These results can be reached only with

adequate animal models that closely reproduce the conditions of the disease in human patients. Therefore, establish a novel thyroid tumor orthotopic xenograft model, providing the injection of cancer cells in the appropriate anatomical site of the animal, is preferred to the use of a conventional murine xenograft test (e.g. subcutaneous) that can be less accurate in mimicking of the disease (Bibby 2004). Furthermore, this kind of model permits an injection of TC cells limited to a partial area of the correspondent organ, in this case only in the left thyroid lobe, that allowed the use of the right lobe as an internal standard.

All the models were established using 6 weeks old CD1-Foxn1$^{nu/nu}$ mice, which present an abnormal hair growth which makes the identification and the palpation of a tumor in the neck region simple. The implantation of the tumors was performed, in all the cases, as described by Buther et al. (Buther et al. 2012) and it is illustrated in Figure 27.

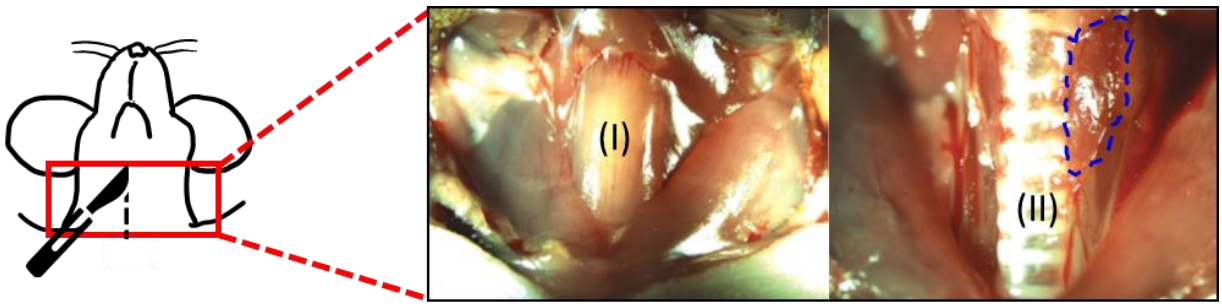

Figure 27. Surgery on mice for the establishment of orthotopic xenograft models. Surgery operated on CD1-Foxn1$^{nu/nu}$ nude mice for the implantation of an orthotopic thyroid cancer tumor in the left thyroid lobe. After a midline cervical incision, the sternohyoid muscle (I) is exposed and dissected uncovering the trachea (II). Hence, an injection of 50'000 TC cells is performed in the thyroid left lobe (in the blue circle). Then soft tissues were repositioned and the skin sutured. The figure is modified from Kim et al. (Kim et al. 2005).

Mice well tolerated the orthotopic implantation of cancer cells, without any complication related to surgery or anesthesia. The tumor growth was followed weekly via US imaging, all the lines exhibited high tumorigenicity (>90%).

5.8 Follow-up of the tumor growth via US imaging

Mice bearing orthotopic TCs underwent US scan on a weekly basis to monitor the tumor growth. Sedated animals were placed supine on a surgery platform warmed up to 37°C, and the MS550D Transducer gently blocked on the neck region to obtain an imaging of the

transverse plane. The thyroid region was individuated using the carotid arteries as referral, highlighting them via color Doppler mode (Figure 28A).

The tumors were visualized as a hypoechoic and poorly vascularized area within the left thyroid, usually expanding in the direction of the fatty tissues of the neck, and finally surrounding the trachea (Figure 28B).

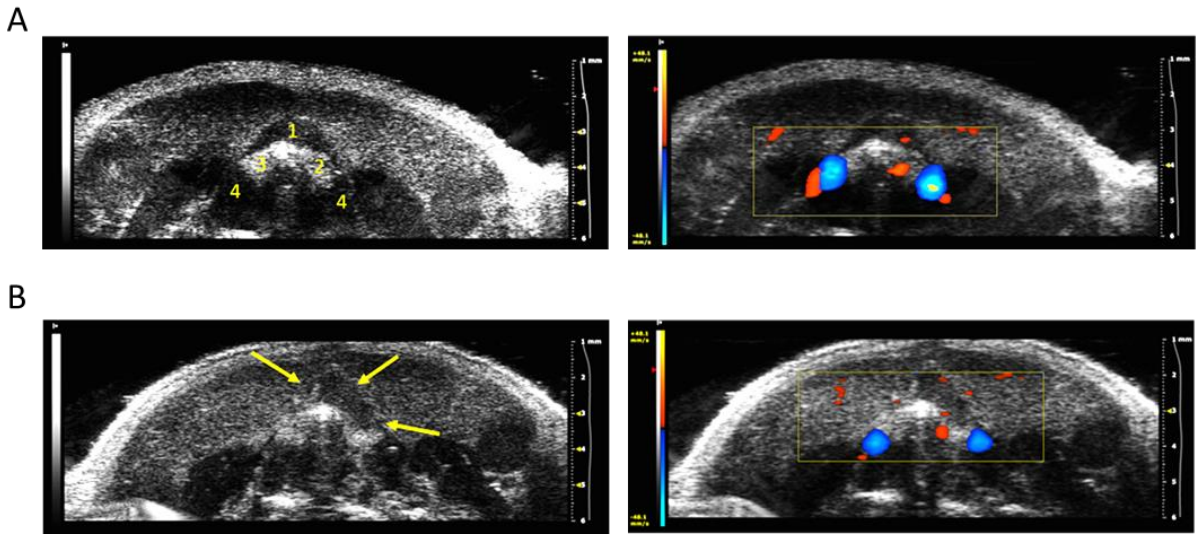

Figure 28. Orthotopic tumor growth monitoring via ultrasound imaging.
(A) B-mode (left) and Doppler mode (right) ultrasound scans of the neck region of a CD1-Foxn1$^{nu/nu}$ mouse. The sternohyoid muscle (1) appear as a dark region over the thyroid left (2) and right (3) lobes that are visualized as hyperechoic areas. The carotid arteries (4) activity can be enhanced via Doppler mode and allows correct finding of the thyroid. (B) B-mode and Doppler mode of a CD1-Foxn1$^{nu/nu}$ mouse bearing a BcPAP thyroid cancer as representative images. The presence of the tumor, growing from the thyroid lobe to the surrounding fatty tissues is evidenced by yellow arrows. The Doppler mode evidenced lack of vascularization, indicating possibility of necrosis in the inner areas of the lesion.

The presence of a motor connected to the transducer, capable to move it through cranial/ direction, permitted a 3D reconstruction of the tumors via Vevo LAB (Visualsonics) software. Volume estimations were carried out from the 3D reconstructions, drawing a ROI around the tumor borders on each slice.

FRO82-1, CAL62 and BcPAP showed different tumor growing rate reaching the critical diameter of 0.5 cm and a volume >60 mm^3 in 4, 5 and 6 weeks after cell injection, respectively (Figure 29).

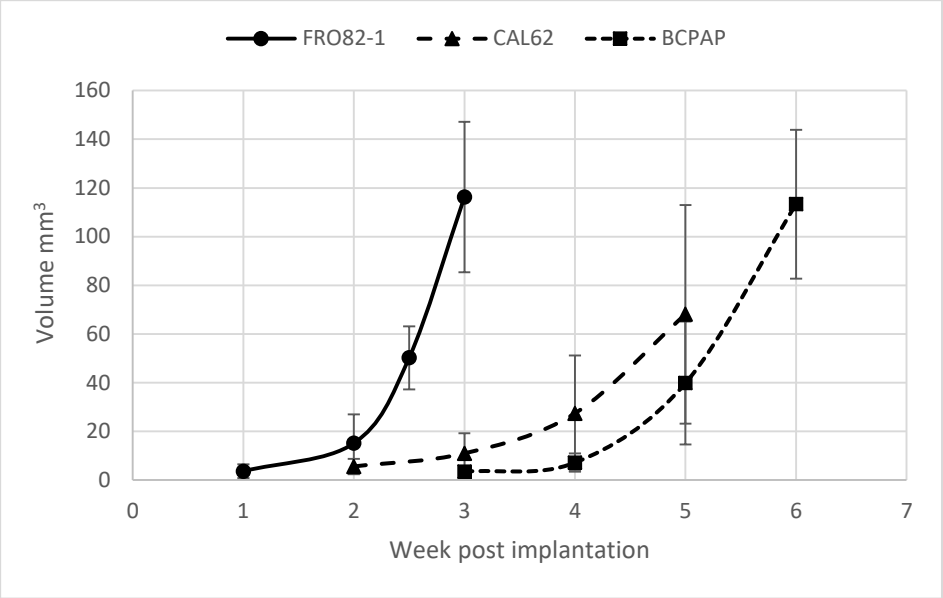

Figure 29. Growth rate of the different thyroid tumors.
This plot reports the volumes of the orthotopically implanted thyroid tumors at different time points during the growth monitoring, calculated *in vivo* via ultrasound 3D reconstruction. Data are presented as mean±SD.

5.9 Imaging of the lesions via FMT scan

The use of *in vivo* FMT imaging on group I mice had a dual purpose. On one hand, it was performed to confirm the *in vivo* binding and specificity of the aGal3-F(ab')$_2$ derivative. On the other hand, to verify the expression of Gal3 in the lesion visualized via US scan together with an evaluation of size and position.

The tests were performed injecting via catheter in the tail vein of the animals 54µg of aGal3-F(ab')$_2$-Cy5.5, corresponding to 2 nmol of NIR-dye, and performing an FMT scan in the neck region 48 hours post injection. The signal was collected via CCD camera and modeled as a 3D image by the VisEn FMT™2500 Software. Images showed, for all the cell lines considered, a specific signal from tumors already outlined by US screening in the left thyroid lobe area (Figure 30A).

Differences of the Cy5.5-conjugate accumulation in the left and right thyroid lobe areas were evaluated drawing ROIs in the corresponding regions of the neck, calculating it via software after calibration. The total accumulated conjugate in the area of the tumor (thyroid left lobe) was consistently higher than the signal in the area of the healthy thyroid lobe (Figure 30B).

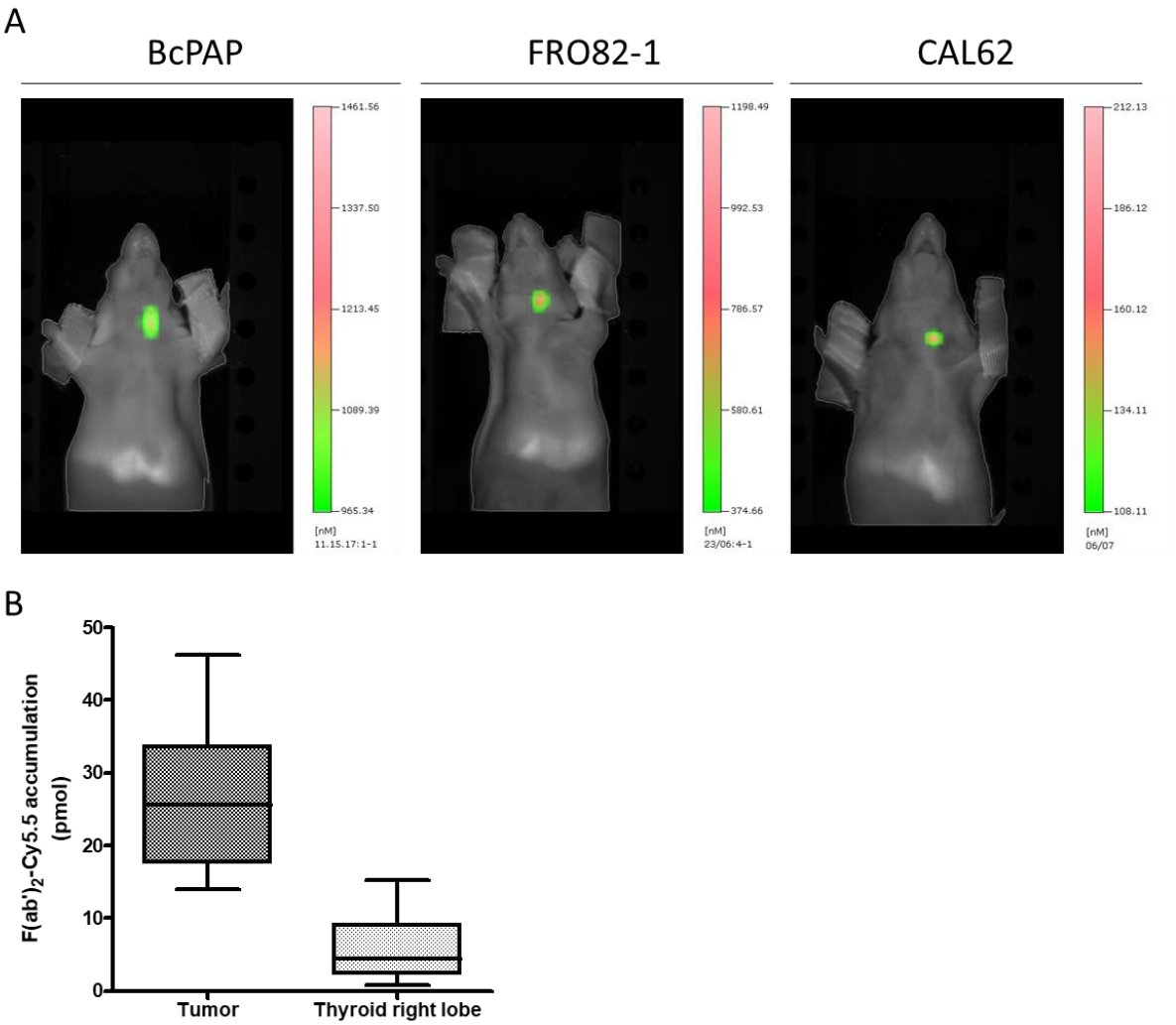

Figure 30. FMT scan of mice transplanted with different cell lines.

(A) Representative pictures obtained via FMT scan 48 hours p.i. of aGal3-F(ab')$_2$-Cy5.5 on mice bearing orthotopic thyroid tumors exceeding 60 mm^3 of volume. For all the tumors, the position and size were further confirmed at anatomical analysis (see section 5.10). (B) The graph shows the difference in total accumulated amount of aGal3-F(ab')$_2$-Cy5.5 between the tumor bearing left lobe and the thyroid right lobe after 48 hours from the injection.

5.10 Immuno-PET imaging of orthotopic tumors with aGal3-F(ab')$_2$-DFO-^{89}Zr

In vitro tests showed that the aGal3-F(ab')$_2$-DFO-^{89}Zr radiotracer possess excellent affinity, specificity and stability. To further confirm the potency of the immune-PET imaging for thyroid cancer diagnosis the tracer was tested *in vivo* on the animals belonging to the group I. Control mice (bearing no tumors) and mice bearing orthotopic tumors were injected with aGal3-F(ab')$_2$-DFO-^{89}Zr five days after the FMT scans. Then, mice underwent PET/CT scan 48 hours post injection and the images were reconstructed using the using OSEM3D/MAP algorithm.

For all the tumor type implanted, static PET/CT scans modeled as MIP images, shown in figure 30A, revealed low background and high contrast, with a clear accumulation in the neck region that is not present in the control subgroup, indicating the position of the tumor. A rapid blood clearance with accumulation in liver followed by excretion via urinary system (kidneys and bladder), was noticed for all the subgroups and represents the expected elimination pathway of an antibody-based radiotracer.

Focusing on the neck region, for a more accurate investigation of tumor-bearing mice, it is possible to observe how the PET-signal indicates a clear uptake of aGal3-F(ab')$_2$-DFO-^{89}Zr in the cancer-infiltrated left thyroid lobe and lymph nodes, while any signal is detected in the contralateral right normal thyroid lobe. Figure 31B, showing a comparison of the PET/CT and FMT scans with anatomical analysis during necropsy, definitively confirms those data, showing high contrast due to no uptake in healthy tissues of the neck as, for example, the right side of the mouse trachea where the right lobe of the thyroid is located. The organ exposure calculated for the kidneys as organ presenting the higher accumulation of the tracer, resulted in an organ dose of 0.01 mSv/MBq, against an approximate effective total body dose of 0.061 mSv/MBq.

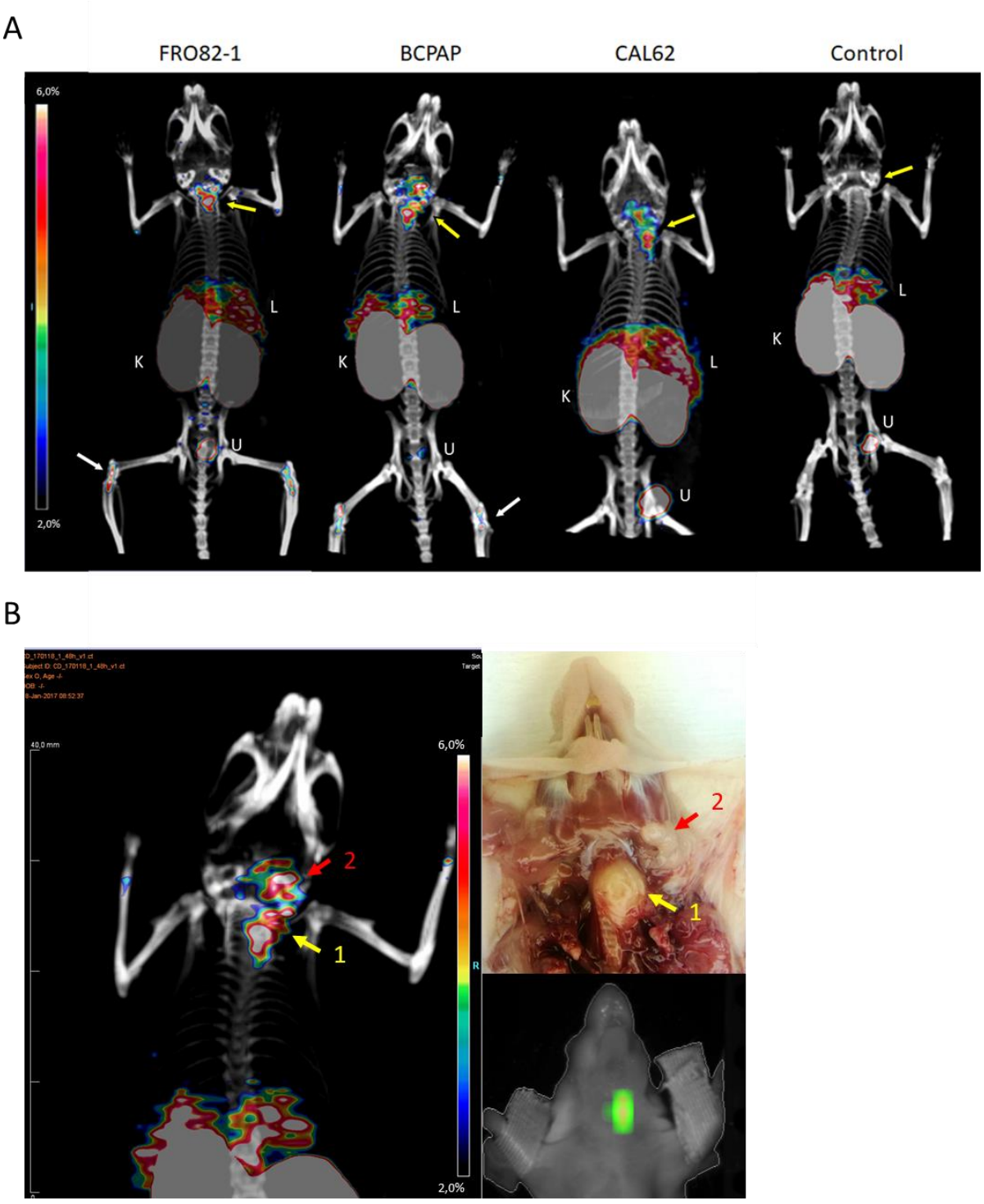

Figure 31. PET/CT imaging of mice bearing TCs with aGal3-F(ab')$_2$-DFO-^{89}Zr.

(A) Representative PET/CT images, visualized as MIP, obtained 48 hours post injection of aGal3-F(ab')$_2$-DFO-^{89}Zr (2.2MBq ca.) on group I mice. Yellow arrows show the signal in the neck region, due to the presence of TC. It is possible to notice the accumulation of the radiotracer in liver (L), kidneys (K), bladder (due to urine, U). Scalebar: 2-6% ID/g.

(B) FMT and PET/CT *in vivo* scans of a mouse bearing BcPAP TC compared with the findings during the anatomical study at necropsy on the same animal. These pictures demonstrate the

correspondence between the signals obtained using different imaging techniques and the real position and size of the principal tumor mass (1) and of tumor infiltrating the fatty tissues (2).

5.11 Head to head comparison of ^{124}I PET/CT versus Immuno-PET Imaging of Orthotopic Tumors

After investigating the accuracy and specificity of the developed imaging strategy, the method was compared with ^{124}I PET/CT imaging, using it as a surrogate of the gold standard methodology for thyroid related diseases (radioiodine scintigraphy). Mice belonging to group II, with tumors exceeded a volume of 60mm^3, were injected with 1.1MBq of ^{124}I and imaged after one hour. Control mice showed a clear accumulation of radioiodine in both thyroid lobes, as expected for a healthy thyroid gland expressing the NIS transporter. Mice bearing orthotopic tumors presented a strong accumulation of radioiodine only in the right thyroid lobe, showing a reduced uptake in the left lobe bearing the tumor, with a decreasing signal BcPAP>FRO82-1>CAL62, respectively (Figure 32). In some animals the enlargement of thyroid lobe during TC orthotopic inoculation induced extravasation of medium containing cancer cells, which infiltrated neck fatty tissues. Those cells were not visualized via ^{124}I PET/CT, but were highlighted using aGal3-F(ab')$_2$-DFO-^{89}Zr.

In principle radioiodine imaging do not allow imaging of TC cells with reduced capability of to accumulate radioiodine, resulting not specific for TC diagnosis (see paragraph 1.2.5). Differently, the immune-PET scan with aGal3-F(ab')$_2$-DFO-^{89}Zr showed a specific and sensitive visualization of the thyroid tumors.

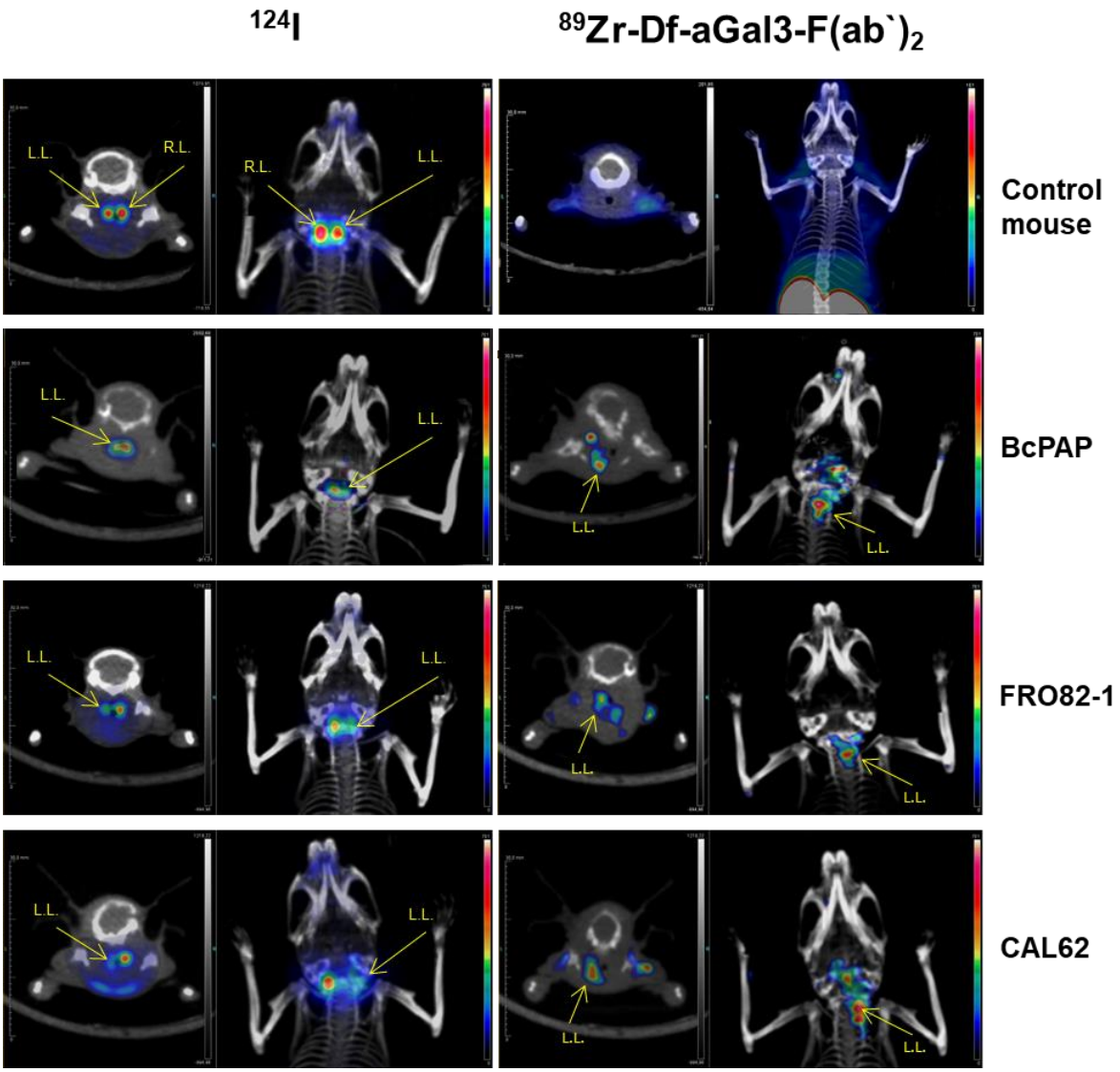

Figure 32. PET/CT imaging with ^{124}I and with aGal3-F(ab')$_2$-DFO-^{89}Zr in comparison.
Head to head comparison of the PET/CT imaging on mice bearing orthotopic TC and control animals operated after 1 hour post injection of ^{124}I and 48 hours post injection of aGal3-F(ab')$_2$-DFO-^{89}Zr. Each row shows the axial static PET/CT scan intersecting the middle of the thyroid, and the MIP image. L.L= left lobe; R.L= right lobe.

5.12 Tracers accumulation analysis via biodistribution

After PET/CT scan, mice were immediately sacrificed and selected organs were excised, weighted and the accumulated activity was measured using a gamma-counter. The accumulation of the tracer was calculated as injected dose per gram percentage (%ID/g). The analysis of the mice at necropsy allowed the identification of the position and size of the tumors.

Mice from group I, injected with circa 2.2MBq of aGal3-F(ab')$_2$-DFO-^{89}Zr, revealed an accumulation in the tumor of 4.0±0.7, 5.5±1.5 and 3.5±0.9%ID/g for BcPAP, FRO82-1 and CAL62 respectively, in contrast to the healthy right thyroid lobes presenting an uptake of 1.3±0.3%ID/g (Figure 33A). The tumor to right thyroid lobe ratio, calculated for each tumor versus the corresponding right lobe, exhibited values between 3 and 5 for all the cell lines (see Figure 33B). An accumulation considerably higher than the background (blood: 0.18±0.02%ID/g; muscle: 0.34±0.02%ID/g) was measured for liver and spleen, 3.8±0.3 and 4.1±0.3%ID/g respectively, and is associated to the ^{89}Zr residualization after catabolism of the radiotracer (Anderson et al. 1992). High levels of accumulation in the kidneys (77±15%ID/g) and in the bladder (2.1±0.1%ID/g) are directly correlated to the tracer excretion by urinary tract, as seen also for the full aGal3-mAb (D'Alessandria et al. 2016). Presence of an ^{89}Zr little accumulation in bones and joints (1.5±0.1%ID/g) highlight the good stability in *in vivo* conditions of the labeled tracer (Abou, Ku, and Smith-Jones 2011; Holland et al. 2010). Figure 33B reports the tumor to organ ratios, showing values >1 for all the organs considered except for kidneys, where the accumulation is preponderant.

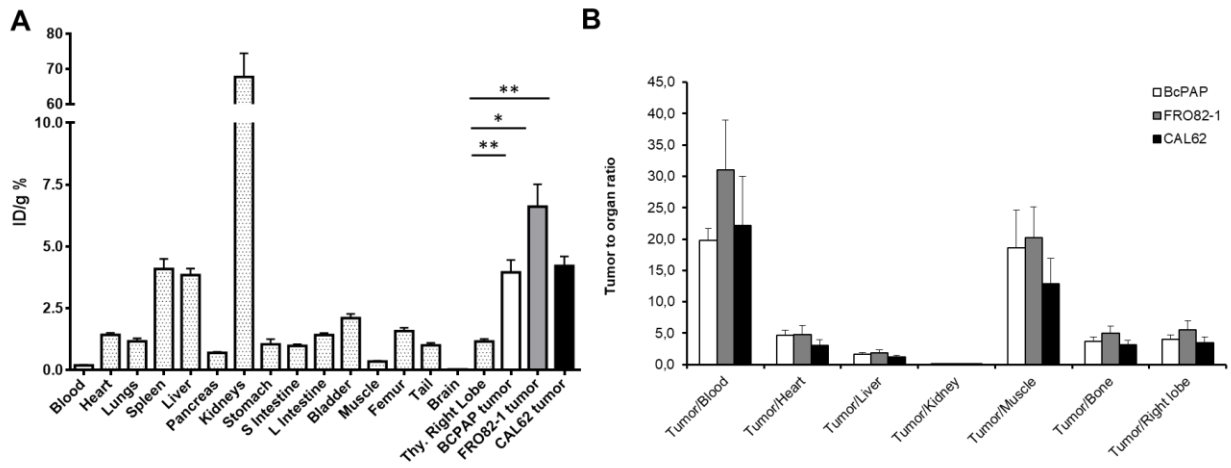

Figure 33. Biodistribution of aGal3-F(ab')$_2$-DFO-^{89}Zr.

(A) Biodistribution analysis performed on mice injected with aGal3-F(ab')$_2$-DFO-^{89}Zr (n=10/tumor type). The differences between accumulation in tumors and in the normal thyroid, considered as organ with background signal, are statistically relevant (*p=<0.01 for FRO82-1, **p<0.05 for BcPAP and CAL62). (B) Plot of the calculated tumor to organ ratios for accumulated activity after 48 hours from injection. Data are shown as mean±SD.

As expected and already visualized via PET/CT imaging, radioiodine accumulates in large amount in the healthy tissues of the normal thyroid right lobe (Figure 34A), revealing an accumulation of 42.4±5.6%ID/g after 1 hour from i.v. injection. Conversely, the uptake in the left lobe bearing TC results extremely low, as a result of the reduction of NIS tumor expression. The PTC cell line BcPAP revealed an accumulation of 6.6±2.0%ID/g, while the ATC cell lines FRO82-1 and CAL62 show accumulations of 2.7±1.1 and 1.7±0.1%ID/g respectively.

The tumor to organ ^{124}I accumulation ratios are reported in Figure 34B, showing a very low tumor/right thyroid lobe (0.16±0.02, 0.06±0.01 and 0.04±0.01 for BcPAP, FRO82-1 and CAL62 respectively), although a ratio >1 with other organs, confirming a reduced, but not completely absent NIS expression.

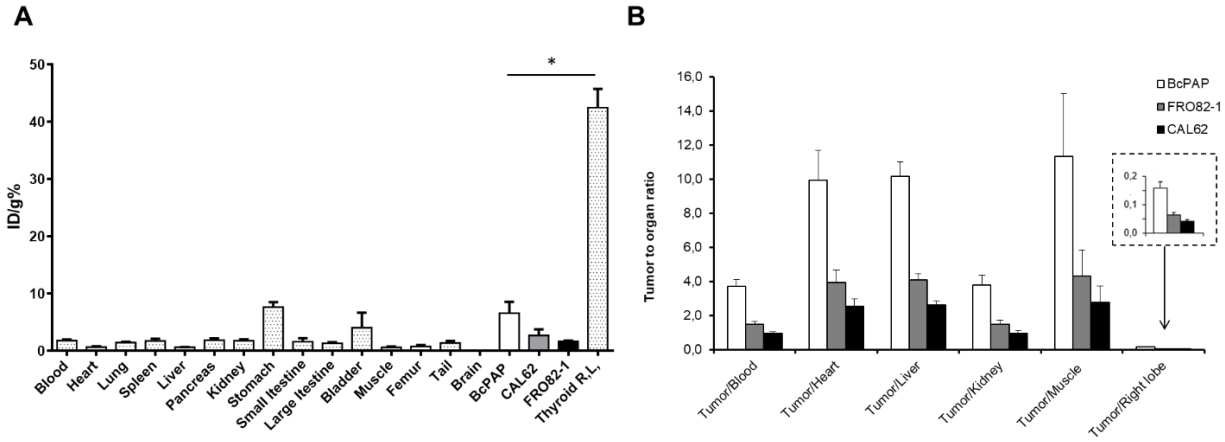

Figure 34. Biodistribution of radioiodine (^{124}I).

(A) Biodistribution analysis on mice (n=5/tumor type) injected with ^{124}I, as surrogate of radioiodine, performed 1 hour after the injection. The low NIS expression led to a decreased activity accumulation in the tumors. The differences between tumors and healthy thyroid are statistically significant (*p=<0.01). (B) Tumor-to-organ ratio values were calculated from gamma-counter measurements of selected organs. Data are shown as mean±SD.

5.13 Correlation of *in vivo* measurements with *ex vivo* data

The predictability of the immuno-PET imaging outcomes was evaluated by *in vivo* versus *ex vivo* aGal3-F(ab')$_2$-DFO^{-8}9Zr tumor accumulation analysis. Among the animal group I, all the subjects presenting no necrotic areas were considered for the correlation (n=24). The image-derived uptake was calculated using Inveon Research Workplace software manually drawing

a ROI on the left side of the trachea encompassing the tumor signal setting a 50% threshold. The ex vivo accumulation data were obtained from biodistribution studies.

The correlation was assessed by plotting the data of ex *vivo v*ersus *in vivo a*ccumulation (Figure 35), and calculating a linear correlation curve resulting in a R^2=0.69.

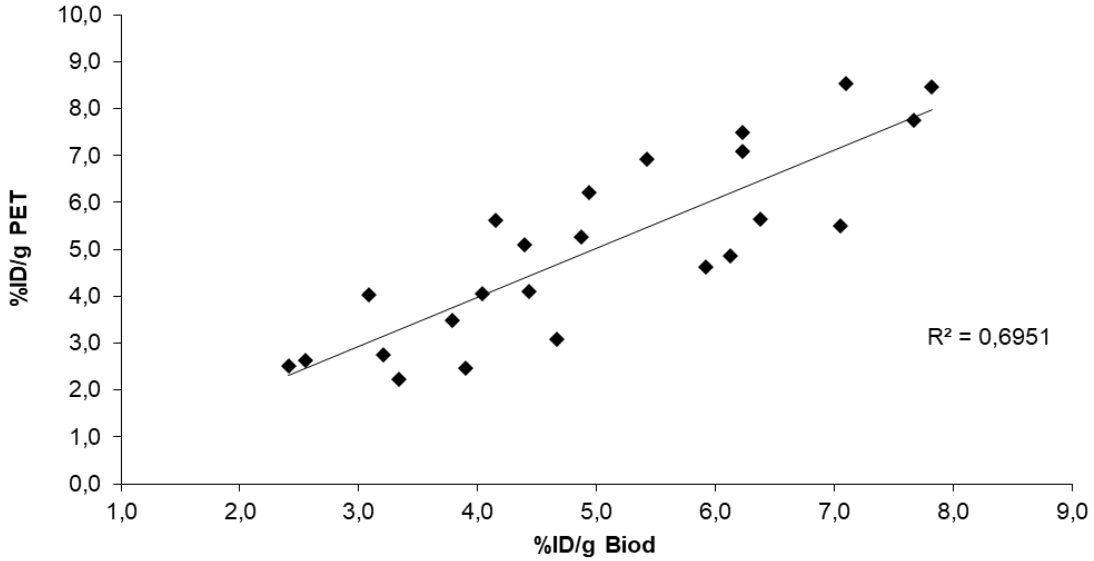

Figure 35. *In vivo* versus *ex vivo* accumulation analysis of aGal3-F(ab')$_2$-DFO-^{89}Zr.

5.14 Histological and immunohistochemical studies

Immunohistochemical analyses were performed independently by Prof. Dr. Armando Bartolazzi (St. Andrea University Hospital, Rome) and Dr. Katja Steiger (Klinikum Rechts der Isar bei der TUM, Munich).

Hematoxylin and eosin stain was performed on slices of entire thyroid glands bearing cancer, it confirmed the enlargement of the left lobe with infiltration of cancer cells, causing the loss of the typical sponge-like morphology of the healthy parenchyma (Figure 36).

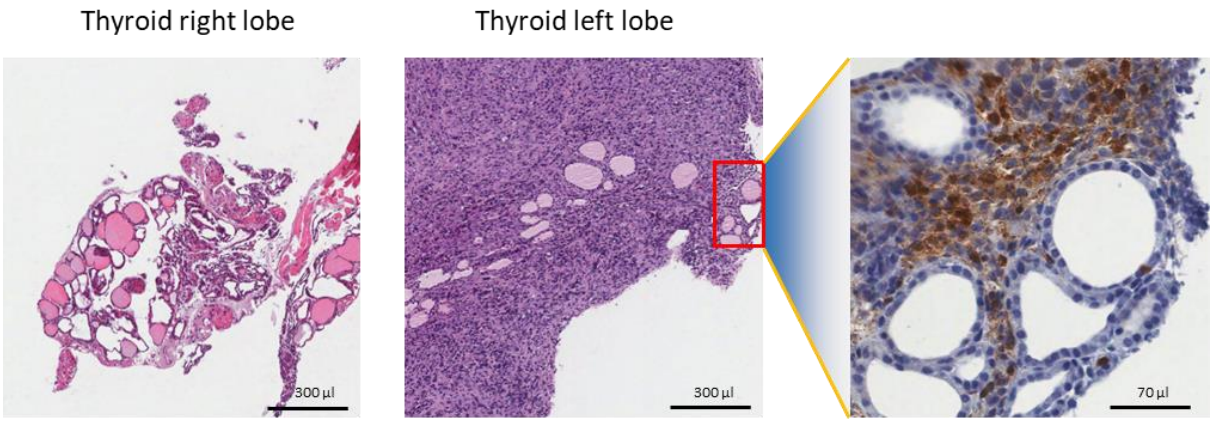

Figure 36. Histological exam of a thyroid bearing tumor on the left lobe.
Hematoxylin and eosin stain of a thyroid bearing BcPAP tumor as representative data. The right lobe presents the typical sponge-like structure characterized by the presence of numerous follicles. The left lobe, bearing the tumor, shows enlargement with a loss of the typical thyroid structure and minimal presence of the residual normal parenchyma. The stain for Gal3 displays TC cells (see also Figure 34B) infiltrating the healthy tissues (left).

The immunostaining for NIS expression confirmed our findings, showing a stronger signal in the DTC cell line BcPAP and a weaker signal for ATC cell lines FRO82-1 and a CAL62 (Figure 37A middle insert). Contrariwise, high expression of NIS was evidenced in the contralateral healthy right thyroid lobe (Figure 37A, right insert).

As expected, the Gal-3 expression was found both in the cytoplasm of the thyroid cancer cells and in the extracellular matrix of the diseased left thyroid (Figure 37B, middle insert), with a weaker staining for CAL62 when compared with BCPAP and CAL62 tumors, as it was already proved by the *in vivo* analysis. In the healthy right thyroid lobe and in the normal residual parenchyma of the left lobe, Gal-3 staining resulted to be very weak or undetectable (Figure 37B, right panel).

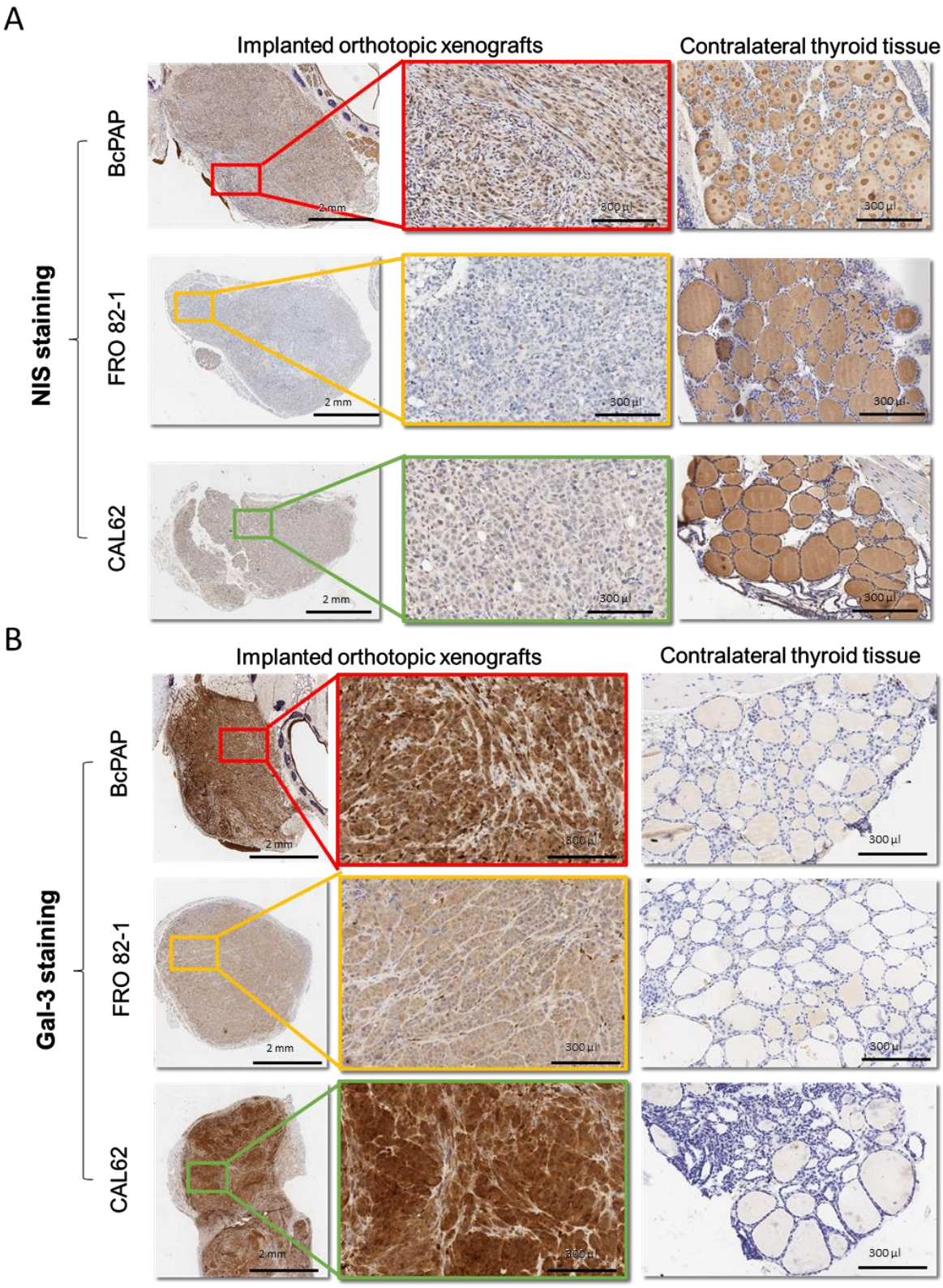

Figure 37. Immunohistochemical analysis for NIS and Gal3 expression.

Thyroid lobes were excised after the mice necropsy and tissue sections stained using HRP-conjugated anti-NIS and anti-Gal3 antibodies. (A) The panel reports the results for the NIS stain, showing a weak signal from BcPAP and undetectable levels for the other DTC cell lines, while the healthy lobes presented high expression. (B) The lower panel reports the Gal3

staining, all the tumor cell lines showed expression with slight differences, while normal lobes did not present any visible coloration.

5.15 Stability *in vivo* of aGal3-F(ab')$_2$-DFO-^{89}Zr

To evaluate presence of free ^{89}Zr in the tissues, the excised organs were homogenized and activity extracted from cells and particulate by spinning at 14'000G for 10 min. Blood was centrifuged after coagulation to separate the serum. From all the samples 5 to 10 µl were spotted on silica strip and run in 50mM DTPA.

Results evidenced that all the activity is bounded to the chelator DFO. Smears obtained for kidney and liver suggest a degradation of the product without release of ^{89}Zr.

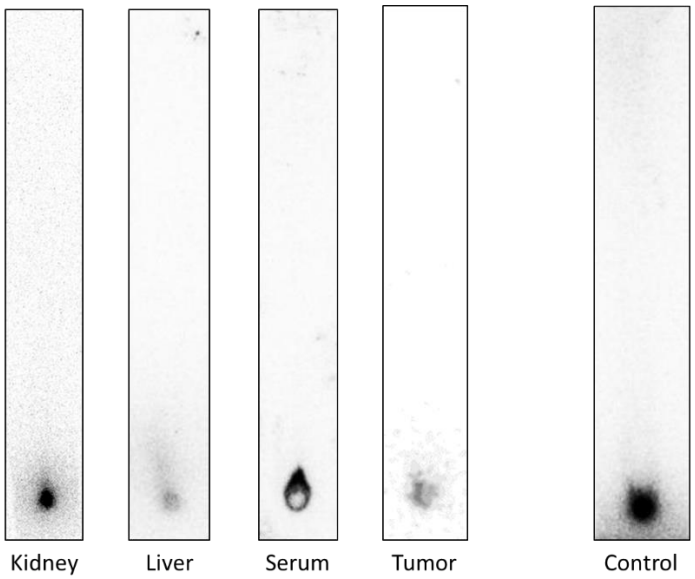

Figure 38. *Ex vivo* TLC run on organ extracts.

TLC run performed on Organ extracted activity spotting 5-10 µl of homogenized on aluminum strip with silica gel 60F_{154} and running with a 50mM DTPA. Images are obtained via autoradiography on after the incubation with a phosphor image plate for 74 hours.

6 **DISCUSSION**

6.1 Designing of a novel methodology for TC diagnosis

The diagnosis of TC is a challenging process, often failing in the discrimination between the big majority of benign nodules and the relatively small number of malignancies. This results in overdiagnosis, overtreatment and excessive long follow up of the patients with aggressive TC type, which consequentially lead to incorrect patient management, unnecessary invasive treatments and low cost-effectiveness (Wang et al. 2015; Lubitz et al. 2014; Tuttle 2018).

The cause of the problems afflicting the TC diagnosis is easily found in the lack of specificity of the technologies and methods used. As already discussed in section 1.2, imaging techniques used in the clinical practice, such as US scan or radioiodine scintigraphy, considered to be the nuclear medicine gold standard procedure for thyroid diseases diagnosis, provide unspecific morphological and physiological information. Fine-needle-aspiration-biopsy (FNAB) represents a technology which has substantially improved the preoperative characterization of thyroid nodules, but this method fails to provide a definitive diagnosis in ~30% of the cases (Baloch et al. 1998). Ultrasonography (thyroid ECO-scan) correctly drives FNAB procedures towards suspicious thyroid nodules, allowing the evaluation of their structure, size and vascularization, but this method alone does not provide biological information. Since, currently, an imaging agent with high and specific uptake in malignant lesions is lacking, it is often not possible to exclude a malignant nodule by imaging and FNAB, especially in patients with multinodular goiter. This uncertainty results in a large number of diagnostic thyroidectomies for benign thyroid diseases, with malignant versus benign nodules ratio of 1:15 in Germany, 1:7 in Italy and 1:5 in England (Rosato et al. 2004; Bergenfelz et al. 2008). While the problem of overdiagnosis can be handled, but not solved, with new classifications of thyroid neoplasms, it would be preferable if clinically insignificant tumors could be diagnosed prior to surgery.

The individuation of a specific biomarker for TC, like Gal3, which expression was demonstrated to be restricted to thyroid lesions, and absent in the normal parenchyma (Bartolazzi et al. 2001; Bartolazzi, Orlandi, et al. 2008), suggested us to use it as a target for developing a sensitive

and high-resolution technique, based on immuno-PET/CT. Such a new imaging approach could “kill two birds with one stone”. In fact, on one side, the specific targeting can differentiate malignant from benign nodules, even in presence of multinodularity, avoiding repetition of invasive procedures for the patient (e.g. FNAB) and, on the other side, localize the exact position and morphology of the lesion for a pre-surgical evaluation, with a resolution suitable also for MPTC.

To date, the clinical use of PET/CT for TC patients is mostly limited to ^{131}I, ^{124}I and [^{18}F]-FDG imaging for the detection of body metastases (Giraudet and Taieb 2017; Basu et al. 2011). The immuno-PET approach for TC diagnosis was only slightly investigated before. In a study from 2007 by Fortin et al. a chimeric mAb against the variant v6 of the membrane glycoprotein CD44 (CD44v6) was labeled via iodination using ^{124}I and used to image TC in mice injected with anaplastic KAT-4 cells in flanks and arms. Despite the high K_d and tumor accumulation of the obtained probe, low stability led to deiodination *in vivo* with consequent strong background in the thyroid glands. Furthermore, CD44v6 is generally higher expressed by DTC, but the expression in ATC is reported in a few cases only (Fortin et al. 2007; Gasbarri et al. 1999). Recently, the platelet-derived growth factor receptor alpha (PDGFRα) was demonstrated to be linked to dedifferentiation and metastatic disease in PTC (Lopez-Campistrous et al. 2016). Wagner et al. developed a radiotracer based on a mAb anti PDGFRα labeled with ^{64}Cu via DOTA conjugation (Wagner et al. 2018). This radio-immunocomplex showed high uptake in BcPAP tumors implanted in the flank of NSG mice but revealed accumulation also in bone marrow and spleen. Moreover, there are no studies that confirm high expression of PDGFRα in ATC. The same limitation affects the trivalent bispecific immunotracer directed to the carcinoembryonic antigen (CEA) and HSG peptide (IMP288) engineered for TC pre-targeting by Bodet-Milin et al.. The use of ^{68}Ga-labeled IMP288 is limited since CEA is well-known to be a valid biomarker only for MTC (Cimitan et al. 1979; Bodet-Milin et al. 2016).

Proof of concept studies for the use of an immuno-radiotracer direct to Gal3 were conducted in last years from our group (Bartolazzi, D'Alessandria, et al. 2008; D'Alessandria et al. 2016). In 2008, a first work was carried out on mice bearing ARO ATC inoculated subcutaneously into

the flank, injected with 4MBq of ^{99m}Tc-labeled anti-Gal3 mAb M3/38 and imaged using a high-resolution mini gamma camera. Despite the low tumor to background signal ratio, the tracer exhibited specificity *in vivo* for ATC, encouraging the imaging with a more sensitive imaging modality. Therefore, the second and wider study investigated the possibility to image the TC with a probe based on the same antibody labeled with the positron emitter ^{89}Zr and using a PET/CT scanner. The imaging was performed on mice bearing different type of TC inoculated subcutaneously into the flank after 72 hours from the i.v. injection of 1.5 MBq tracer. The uptake revealed to be specific and high for TCs, and associated to a good image contrast. mAbs are normally associated to a long residence time in the blood pool and subjected to unspecific uptake in different body compartments (e.g. liver), these factors lead to a long time interval necessary to achieve a high contrast imaging. Besides this, the tracer was tested on monolayer cell cultures and in subcutaneous xenograft animals, models that are far away from reproducing the disease conditions in human patients.

In the present work, I aimed to move further in the direction of clinical translation, overwhelming the problematics due to the use of a full size mAb and *in vivo*/*in vitro* poorly representative models. To do this, a new radiotracer has been designed starting from an antibody fragment and tested *in vitro* on cellular spheroids that reproduce the microtumor environment and *in vivo* on orthotopic xenograft animals.

6.2 Development of the immuno-radiotracer anti Gal3

Once an IgG antibody is naturally produced, the presence of the ~50 kDa Fc domain (see Figure 4) does not affect its binding properties with the antigen, determined by the antigen binding site. Nevertheless, it reduces the rate of passive diffusion and convective transport, prolonging the biological half-life, making the antibody susceptible to unspecific binding with Fc-gamma-receptors, present on many immune cells (Ryman and Meibohm 2017). Literature reports several advantageous features for F(ab')$_2$ antibody fragments. They are characterized by a much shorter residence time in any body compartment when compared to the full weight antibody, with a shorter uptake in liver even if compared with smaller fragments, an unimpaired immunoreactivity and a K_d similar to the antibody from which they derive (Covell et al. 1986).

For this reason, an aGal3-F(ab')$_2$ was chosen in this study as a base for the tracer development. The aGal3-F(ab')$_2$ was produced from the M3/38 aGal3-mAb by cleavage of the Fc domain via reaction with the digestive enzyme pepsin. This reaction, described for the first time in 1960 on rabbit IgG mAb (Nisonoff et al. 1960), was adapted for a rat IgG2a mAb according to Stewart and Stanworth protocol (Stewart and Stanworth 1975), adding a pre-incubation step at pH 2.8. As a result, the aGal3-F(ab')$_2$ batch was obtained with minimum quantities of unreacted mAb and degraded product (see figure 12), easy to purify by affinity column and filtration membrane (see paragraph 4.3.3).

The choice of the suitable radionuclide for radiolabeling is strongly dependent on the circulation half-lives of the carrier. For mAb and F(ab')$_2$ fragments long-life PET-radionuclides, such as ^{124}I, ^{64}Cu or ^{89}Zr are recommended (Boswell and Brechbiel 2007). This recommendation is further supported by previous studies, reporting that a radiolabeled F(ab')$_2$ reach an optimal tumor-background ratio between 24 and 48 hours after i.v. injection (Yusufi et al. 2017; Wong et al. 2011). Considering the Gal3 cycle (Figure 5), it was possible to predict the internalization of the tracer (further confirmed in paragraph 5.6.3). In the light of this, since radiohalogens are released by cells after catabolism while radiometals are subjected to residualization, the latter were preferred for radiolabeling. Among ^{89}Zr and ^{64}Cu the first one was chosen for the more suitable half-life and the possibility of chelation with a routine bifunctional chelator already in use in the clinical practice, DFO. The aGal3-F(ab')$_2$ was conjugated with DFO-Bz-NCS and labeled with ^{89}Zr following the procedure described by Holland et al. (Holland et al. 2010) and purified obtaining a F(ab')$_2$ to DFO ratio of 1:1 and elevate radiochemical purity (see Figure 16).

Retained pharmacokinetics, binding affinity for antigen and stability are crucial criteria for pre-clinical test and clinical translation of a tracer (Heskamp et al. 2017), but the modification by cleavage of the native antibody structure, together with conjugation and radiolabeling reactions and large variation of pH (from 2.8 to 9) during these steps, can degrade or denature the protein. Consequently, tests to assess the binding properties of the aGal3-F(ab')$_2$-DFO-^{89}Zr tracer were performed on TC cells, confirming the preserved antibody immunoreactivity and

similar value of K_d (<1nM). Moreover, freshly prepared tracer revealed an intact structure, with solid stability *in vitro* over 4 days in human serum and the storage buffer (see Figure 17). It has been reported that uncomplexed ^{89}Zr in the body accumulates in the bones, especially in the joints, resulting in a reduction of the tumor to background ratio and unspecific signals (Meijs et al. 1997; Abou, Ku, and Smith-Jones 2011). *Ex vivo* stability studies on organs and tumor reported no release of ^{89}Zr from the radio-immunocomplex, while imaging and biodistribution studies detected slight accumulation in the bones (1.5±0.1 %ID/g), with maximum pick in the joints (scapula and knee) that did not interfere with the visualization of the tumor (see Figure 31 and Figure 32).

According to the previously reported externalization and internalization mechanism of Gal3 (Thery et al. 2001; Baptiste et al. 2007), *in vitro* internalization studies demonstrated that once the tracer is bound to cell surface expressed Gal3, the activity is mostly taken up into cells (~65%) or released in the surrounding medium (~20%), while only a small part (<10%) is still confined on the membrane. This revealed a quick Gal3 turnover, possibly enhanced by performing the experiment in non-adherent cells (Baptiste et al. 2007). As previously mentioned, the internalization of aGal3-F(ab')$_2$-DFO-^{89}Zr bounded to Gal3 on the cell surface leads to ^{89}Zr accumulation and residualization by cellular metabolization, this results in a prolonged incorporation, ideal for long-time imaging of tumors to reach high contrast.

6.3 Testing the aGal3 tracer in appropriate *in vitro* and *in vivo* models

In vitro characterization is a critical step for the development of a radiotracer intended to be translated into clinical practice. To accelerate this process, a model that can mimic the conditions of the disease in the human body must be chosen. In fact, *in vivo* tumors present characteristics that can be reproduced only using a three-dimensional model, that takes into account cell to cell interactions and reproduce the conditions of distance from blood vessels as well as microenvironment. These factors affect, in different extent, the penetration of the tracer into the tumor, for example, increasing the interstitial fluid pressure and slowing down diffusion and convection phenomena, together with the cellular gene expression and the metabolic profiles (Minchinton and Tannock 2006; Zhou et al. 2013).

The binding and penetration characteristics of our tracer were evaluated using tumor three-dimensional cultures that formed spheroids (BcPAP and CAL62) and aggregates (FRO82-1). As extensively described in literature, these structures displays many features of the tumor microenvironment and mimic the non-vascular region of tumors, helping in the prediction of *in vivo* results, especially for molecules involved in the cell adhesion as Gal3 (Singh et al. 2015; Fortunati et al. 2004; Phung et al. 2011). As a first step, the differences between monolayer and three-dimensional grown TC cells were assessed via WB and qPCR analyses. Cells were controlled for Gal3 expression, showing an increase of about 35% in the spheroids, this can be explained by the role of this protein as binding partner of cell adhesion molecules (CAMs), as integrins and cadherins, and to the Gal3 upregulation occurrence in hypoxic and nutrient deprived environment, as in the inner layer of a spheroid (Xin, Dong, and Guo 2015; Fortuna-Costa et al. 2014; Ikemori et al. 2014). On the other side, the expression of NIS revealed to be low in all the cases, without any relevant alteration of the expression. Fluorescence microscopy using aGal3-F(ab')$_2$-AlexaFluor488 on monolayer cells and spheroids was performed to evaluate and to predict the penetration of the F(ab')$_2$ in diverse areas of the tumor. The results showed a quicker penetration if compared with other probes (Beltran Hernandez et al. 2019; Ballangrud et al. 2001; Thurber, Schmidt, and Wittrup 2008), possibly because of presence of a high concentration of Gal3 in the inter-cellular space. Furthermore, binding tests on spheroids were performed also with the radiolabeled compound, showing a strong dependence of the on the size. Considering the uptake and the long biological half-life of a F(ab')$_2$ fragment in the body, that allows the penetration in the inner layers of the tumor, high contrast between tumor and healthy tissues was predicted at 48 hours post injection.

As discussed above for *in vitro* experiments, also *in vivo* tests require the use of appropriate animal models. In fact, the common subcutaneous xenograft does not reproduce the microenvironment of the human cancer primary site. To address this issue, in the last years an orthotopic transplantation of tumor cells to the appropriate anatomical site has been established (Bibby 2004). Different studies confirmed that this kind of models can better recapitulate the disease features and predict its progression in human patients (Yamada and

Cukierman 2007; Phung et al. 2011). An orthotopic xenograft model for TC was first reported by Kim et al. for ATC and consequently extended to other cell lines, showing greats results in the estimation of tumorigenicity and angiogenesis, as well as in the study of metastatic processes and evaluation of the radiotherapy (Kim et al. 2005; Morrison et al. 2015; Nucera et al. 2009; Tran Cao et al. 2010; Ahn et al. 2008). In this study all the experiments *in vivo* were performed on mice bearing an orthotopic TC in the left lobe, which allowed us to use the right lobe as an internal control. All the cell lines exhibited high tumorigenicity, and the growth was followed weekly via US scan. As reported in clinical practice, the TCs were visualized as hypoechoic spots growing in the thyroid lobe and occasionally invading the trachea, as showed by necropsy (Pappalardo et al. 2016; Haugen et al. 2016). ATC showed a faster growth, especially for FRO82-1, if compared with the PTC cell line. FMT imaging injecting a Cy5.5 conjugate of the aGal3-F(ab')$_2$ served as a confirmation for the Gal3 expression and of the position of the tumor visualized via US. Additionally, it aided as a proof of concept for the use of specific probes conjugated to NIR-dye (700-900 nm) for image-guided surgery (see paragraph 6.5).

6.4 PET/CT imaging using aGal3-F(ab')$_2$-DFO-^{89}Zr and comparison with ^{124}I

In vivo immuno-PET/CT imaging with aGal3-F(ab')$_2$-DFO-^{89}Zr, performed at 48 hours after i.v. injection, showed an excellent image contrast with a signal restricted to the thyroid lobe bearing the orthotopic tumor. The registered uptake was considerably high if compared with right thyroid lobe, considered as background organ, that showed only minimal or no radioiodine uptake. Since the M3/38 antibody has been demonstrated to recognize an amino-terminal common epitope of human and mouse Gal3, this effect is not due to interspecies differences. Vice versa, normal thyroid tissues displayed a strong and specific radioiodine accumulation, with moderated (BcPAP) to strong (FRO82-1 and CAL62) reduction in TC. Once again this remark that the use of the gold standard technique for thyroid imaging, radioiodine scintigraphy, is not suitable for nodules characterization, but must be limited to metastasis research in DTC cases (Santhanam, Solnes, and Rowe 2017).

Comparing with the images obtained from the previous anti-Gal3 mAb based radio-immunocomplex, tested via subcutaneous xenograft model by our group (D'Alessandria et al. 2016), aGal3-F(ab')$_2$-DFO-^{89}Zr presented faster clearance, high contrast image and lower accumulation in the liver. On contrast, since the novel radiotracer possesses a molecular radius more close to the kidney filtration cutoff, the accumulation in the kidneys appear enhanced and the maximum uptake values is slightly reduced (Schmidt and Wittrup 2009). At any rate, the distance between the natural site of TC development and kidneys permit a high contrast imaging of the area of interest.

The predictability of the immuno-PET/CT method was assessed correlating image-derived uptake calculation and *ex vivo* accumulation analysis expressed as %ID/g (R^2=0.69). The discrepancy among *in vivo* and *ex vivo* tumor uptake might be explained by partial volume effect in the image-derived uptake calculations, that lead to underestimation of the accumulation in small or heterogeneous target regions. The final immunohistochemical analysis, performed on both healthy and diseased thyroid lobes derived sections confirmed the Gal3 expression, the low NIS expression for BcPAP and background NIS staining for FRO82-1 and CAL62.

6.5 Translation in human patients

Within the contest of the implementation in the clinical practice, this work certainly moved forward in the aspects connected with the experimentation in reliable models and the associated prediction of the outcomes. Nevertheless, the clinical translation of a nuclear medicine imaging strategy requires, to ensure a safe use, the minimization of immunogenicity and radiation burden, that can be controlled acting on the chemical properties of the radiotracer and on size and distribution of the used antibody fragment. Therefore, the future steps in view of a translation in the clinical practice must be moved considering these factors.

The use of a stable radiotracer ensures a minimum release of radionuclide in non-target tissues and in excretion pathways. Differently to what reported in precedent studies (Perk et al. 2005; Dijkers et al. 2009; Heskamp et al. 2010), in our work the PET images didn't show elevate accumulation of free ^{89}Zr in bones and joints due to the use of DFO as a chelator, confirming

the good data from stability *in vitro*. Nevertheless, the use of a more suitable chelator for ^{89}Zr need to be further explored. Extensive literature reports the preference of acyclic chelators with hydroxamate groups for complexing zirconium. Among those, octadentate ligands as DFO*, CP256, DFO-Sq and HOPO showed higher stability and lower bone uptake than DFO, but *in vivo* studies over extended periods of time have not quantified this (Heskamp et al. 2017; Deri et al. 2015; Vugts et al. 2017; Ma et al. 2015). Recently some studies have shown great results for complexation of ^{89}Zr with fusarine C and DOTA that revealed to be suitable alternative for DFO in terms of stability *in vivo*. The use is, anyway, limited for heat resistant biomolecules since these chelators require a radiolabeling procedure carried out at elevate temperature (Zhai et al. 2015; Pandya et al. 2017).

Considering tracer distribution data, a bigger limitation for the clinical approach is represented by the high uptake in kidneys (77±15%ID/g) for a prolonged time. The dose to kidneys is just one sixtieth of the total body dose, but it can have still harmful effects on this organ when ^{89}Zr-labelled tracers are injected in patients. Good results are obtained for radiolabeled F(ab')$_2$ fragments by co-administration of cationic amino acids solutions, as D- and L- isomers of lysine, or basic polypeptides, as poly-L-lysine (Behr, Goldenberg, and Becker 1998). To control the plasma residence, PEGylation, performed modifying the antibody fragment by conjugation of a polyethylene glycol chain, and PASylation, performed by fusion of a Pro-Ser-Ala polypeptide via genetic engineering with gene cassette, have demonstrated to drastically prolong the blood half-life and, in some cases the to decrease the binding affinity (Rashidian et al. 2017; Schlapschy et al. 2013).

Xenogenic antibodies are characterized by a high immunological risk, in the body they can cause an unwanted humoral or cellular immune response that is manifested, in the case of immuno-PET methods, in the production of antibodies directed against the radiotracer, with an impairment of the patient safety and modification of the pharmacokinetic. Recombinant antibody constructs can lower the risk of immune reactions. Once identified the epitope, in fact, it is possible to engineer part of the antibody to obtain, as a first step, a human-animal chimera with humanized constant region, achieving the diminution of the anti-antibodies response. As

a second step, the synthesis of a complete humanized product by insertion of the specific complementarity determining region (CDR) in a human antibody fragment scaffold, would lead to a considerably decreased immunogenicity (Bruggemann et al. 1989; Harding et al. 2010; Ahmadzadeh et al. 2014).

Another opportunity given by genetic engineering is the design of smaller probes with retained binding affinity. In fact, when the hypervariable region is individuated and characterized, this can be engineered into the scaffold of antibody-derived constructs as Fab, nanobodies or scFv. Changing the size of the carrier protein with smaller biomolecules modifies its biological half-life, increasing the clearance and reaching the maximum uptake peak in the tumor at earlier time points, this can reduce the patient exposure to radioactivity and hospitalization time.

6.6 Conclusions and outlooks

With this work I aimed to develop a non-invasive method based on PET-imaging for the identification and discrimination of malignant thyroid nodules using as reliable biomarker Gal3. This can be possible designing a radio-probe able to provide morphological details, overcoming the lacking in specificity of other imaging strategies and the limitations in terms of delayed clearance and image contrast that are typical using a full size mAb. As a result, the novel radiotracer developed, aGal3-F(ab')$_2$-DFO-^{89}Zr, revealed high affinity and immunoreactivity on TC cells expressing Gal3 and good stability *in vivo*. It permitted, for the first time, the *in vivo* PET imaging of malignant thyroid cells implanted into their anatomical origin equivalent within the host animal, making considerable steps forward for the translation of the new imaging method in clinical application. These results were observed *in vivo* using orthotopic tumors derived from different type of TC cells.

Moving another step forward in the direction of the clinic implementation of the actual paradigm in thyroid imaging, taking into account the considerations expressed in paragraph 6.5, new tracers for the TC diagnosis were designed in cooperation with Prof. Arne Skerra from TUM School of Life Sciences in Weihenstephan. The variable domain of the M3/38 antibody was characterized and then genetically engineered in a human Fab scaffold, obtaining chimeric and humanized variants, which were modified to bear a PASylated chain bringing a specific site for

DFO conjugation and radiolabeled with ^{89}Zr. These new tracers, designed to present an enhanced clearance and reduced immunogenicity, are currently under preclinical validation using the same *in vivo* and *in vitro* models developed in this work.

The successful use of FTM imaging to monitor the orthotopic tumor growth suggested the possibility for performing image-guided surgery of thyroid nodules using an anti-Gal3 immuno-probe conjugated with a clinical approved NIR-dye (700-900nm). In the last years, in fact, the rise of robotic surgery introduced the opportunity for *in vivo* intraoperative optical imaging, leading to a dramatic increase of proof of concept clinical trials with NIR-dye. Only a small group of the contrast agents under investigation has obtained full clinical approval by FDA or EMEA, these has been tested as non-targeted probes and consequentially their use is restricted to few organs and specific type of lesions (Li et al. 2012; Kahramangil and Berber 2017; Vahrmeijer et al. 2013). For this purpose, the design of a probe able to minimize immunogenicity must be performed together with an improvement of the technology for conjugation of the currently approved NIR-dyes.

Looking at the outlooks from another perspective, the high uptake of aGal3-F(ab')$_2$-DFO-^{89}Zr coupled to the low accumulation in healthy tissues indicates that Gal3 is a promising target for radionuclide therapy, especially in radioiodine negative or refractory ATC. In this context a targeted alpha-therapy (TAT) approach is preferable, consisting in the radiolabeling of aGal3-F(ab')$_2$ with an α-emitter radionuclide (Marcu, Bezak, and Allen 2018). Among these, ^{213}Bi and ^{225}Ac showed high stability when complexed with the bifunctional variants of DTPA and DOTA (Morgenstern, Bruchertseifer, and Apostolidis 2012).

To conclude, the immuno-PET targeting of Gal3, compared to other PET approaches, appears to be a specific, reliable and promising diagnostic method for *in vivo* detection and biological characterization of malignant tumors growing into thyroid glands. Due to the superior technical characteristics of the PET technology when compared with other imaging modalities, the method proposed might improve and innovate thyroid cancer diagnostics. Furthermore, it might help in making decisions on the most appropriate therapeutic intervention and follow up

strategies (Sun, DeMonner, and Davis 2013; Tufano, Noureldine, and Angelos 2015), reducing unnecessary surgery and social costs (Yeh et al. 2015).

7 **REFERENCES**

Abou, D. S., T. Ku, and P. M. Smith-Jones. 2011. 'In vivo biodistribution and accumulation of 89Zr in mice', *Nucl Med Biol*, 38: 675-81.

Adeniran, A. J., Z. Zhu, M. Gandhi, D. L. Steward, J. P. Fidler, T. J. Giordano, P. W. Biddinger, and Y. E. Nikiforov. 2006. 'Correlation between genetic alterations and microscopic features, clinical manifestations, and prognostic characteristics of thyroid papillary carcinomas', *Am J Surg Pathol*, 30: 216-22.

Ahmadzadeh, V., S. Farajnia, M. A. Feizi, and R. A. Nejad. 2014. 'Antibody humanization methods for development of therapeutic applications', *Monoclon Antib Immunodiagn Immunother*, 33: 67-73.

Ahn, S. H., Y. Henderson, Y. Kang, C. Chattopadhyay, P. Holton, M. Wang, K. Briggs, and G. L. Clayman. 2008. 'An orthotopic model of papillary thyroid carcinoma in athymic nude mice', *Arch Otolaryngol Head Neck Surg*, 134: 190-7.

Akahani, S., P. Nangia-Makker, H. Inohara, H. R. Kim, and A. Raz. 1997. 'Galectin-3: a novel antiapoptotic molecule with a functional BH1 (NWGR) domain of Bcl-2 family', *Cancer Res*, 57: 5272-6.

Ambrosini, V., J. J. Morigi, C. Nanni, P. Castellucci, and S. Fanti. 2015. 'Current status of PET imaging of neuroendocrine tumours ([18F]FDOPA, [68Ga]tracers, [11C]/[18F]-HTP)', *Q J Nucl Med Mol Imaging*, 59: 58-69.

Anbar, M., S. Guttmann, and Z. Lewitus. 1960. 'The accumulation of fluoroborate ions in thyroid glands of rats', *Endocrinology*, 66: 888-90.

Anderson, C. J., J. M. Connett, S. W. Schwarz, P. A. Rocque, L. W. Guo, G. W. Philpott, K. R. Zinn, C. F. Meares, and M. J. Welch. 1992. 'Copper-64-labeled antibodies for PET imaging', *J Nucl Med*, 33: 1685-91.

Bailly, C., P. F. Clery, A. Faivre-Chauvet, M. Bourgeois, F. Guerard, F. Haddad, J. Barbet, M. Cherel, F. Kraeber-Bodere, T. Carlier, and C. Bodet-Milin. 2016. 'Immuno-PET for Clinical Theranostic Approaches', *Int J Mol Sci*, 18.

Bale, W. F., M. A. Contreras, and E. D. Grady. 1980. 'Factors influencing localization of labeled antibodies in tumors', *Cancer Res*, 40: 2965-72.

Ballangrud, A. M., W. H. Yang, D. E. Charlton, M. R. McDevitt, K. A. Hamacher, K. S. Panageas, D. Ma, N. H. Bander, D. A. Scheinberg, and G. Sgouros. 2001. 'Response of LNCaP spheroids after treatment with an alpha-particle emitter (213Bi)-labeled anti-prostate-specific membrane antigen antibody (J591)', *Cancer Res*, 61: 2008-14.

Baloch, Z. W., M. J. Sack, G. H. Yu, V. A. Livolsi, and P. K. Gupta. 1998. 'Fine-needle aspiration of thyroid: an institutional experience', *Thyroid*, 8: 565-9.

Baptiste, T. A., A. James, M. Saria, and J. Ochieng. 2007. 'Mechano-transduction mediated secretion and uptake of galectin-3 in breast carcinoma cells: implications in the extracellular functions of the lectin', *Exp Cell Res*, 313: 652-64.

Barbosa, F. G., M. A. Queiroz, R. F. Nunes, J. F. G. Marin, C. A. Buchpiguel, and G. G. Cerri. 2018. 'Clinical perspectives of PSMA PET/MRI for prostate cancer', *Clinics (Sao Paulo)*, 73: e586s.

Bartolazzi, A., C. D'Alessandria, M. G. Parisella, A. Signore, F. Del Prete, L. Lavra, S. Braesch-Andersen, R. Massari, C. Trotta, A. Soluri, S. Sciacchitano, and F. Scopinaro. 2008. 'Thyroid cancer imaging in vivo by targeting the anti-apoptotic molecule galectin-3', *PLoS One*, 3: e3768.

Bartolazzi, A., A. Gasbarri, M. Papotti, G. Bussolati, T. Lucante, A. Khan, H. Inohara, F. Marandino, F. Orlandi, F. Nardi, A. Vecchione, R. Tecce, O. Larsson, and Group Thyroid Cancer Study. 2001. 'Application of an immunodiagnostic method for improving preoperative diagnosis of nodular thyroid lesions', *Lancet*, 357: 1644-50.

Bartolazzi, A., F. Orlandi, E. Saggiorato, M. Volante, F. Arecco, R. Rossetto, N. Palestini, E. Ghigo, M. Papotti, G. Bussolati, M. P. Martegani, F. Pantellini, A. Carpi, M. R. Giovagnoli, S. Monti, V. Toscano, S. Sciacchitano, G. M. Pennelli, C. Mian, M. R. Pelizzo, M. Rugge, G. Troncone, L. Palombini, G. Chiappetta, G. Botti, A. Vecchione, R. Bellocco, and Group Italian Thyroid Cancer Study. 2008. 'Galectin-3-expression

analysis in the surgical selection of follicular thyroid nodules with indeterminate fine-needle aspiration cytology: a prospective multicentre study', *Lancet Oncol*, 9: 543-9.

Basolo, F., L. Torregrossa, R. Giannini, M. Miccoli, C. Lupi, E. Sensi, P. Berti, R. Elisei, P. Vitti, A. Baggiani, and P. Miccoli. 2010. 'Correlation between the BRAF V600E mutation and tumor invasiveness in papillary thyroid carcinomas smaller than 20 millimeters: analysis of 1060 cases', *J Clin Endocrinol Metab*, 95: 4197-205.

Basu, S., M. Urhan, J. Rosenbaum, and A. Alavi. 2011. 'PET and PET/CT in the management of thyroid cancer', *Methods Mol Biol*, 727: 205-24.

Behr, T. M., D. M. Goldenberg, and W. Becker. 1998. 'Reducing the renal uptake of radiolabeled antibody fragments and peptides for diagnosis and therapy: present status, future prospects and limitations', *Eur J Nucl Med*, 25: 201-12.

Belfiore, A., D. Giuffrida, G. L. La Rosa, O. Ippolito, G. Russo, A. Fiumara, R. Vigneri, and S. Filetti. 1989. 'High frequency of cancer in cold thyroid nodules occurring at young age', *Acta Endocrinol (Copenh)*, 121: 197-202.

Beltran Hernandez, I., R. Rompen, R. Rossin, K. T. Xenaki, E. A. Katrukha, K. Nicolay, P. van Bergen En Henegouwen, H. Grull, and S. Oliveira. 2019. 'Imaging of Tumor Spheroids, Dual-Isotope SPECT, and Autoradiographic Analysis to Assess the Tumor Uptake and Distribution of Different Nanobodies', *Mol Imaging Biol*.

Bergenfelz, A., S. Jansson, A. Kristoffersson, H. Martensson, E. Reihner, G. Wallin, and I. Lausen. 2008. 'Complications to thyroid surgery: results as reported in a database from a multicenter audit comprising 3,660 patients', *Langenbecks Arch Surg*, 393: 667-73.

Beuthien-Baumann, B., A. Strumpf, J. Zessin, J. Bredow, and J. Kotzerke. 2007. 'Diagnostic impact of PET with 18F-FDG, 18F-DOPA and 3-O-methyl-6-[18F]fluoro-DOPA in recurrent or metastatic medullary thyroid carcinoma', *Eur J Nucl Med Mol Imaging*, 34: 1604-9.

Bibbins-Domingo, K., D. C. Grossman, S. J. Curry, M. J. Barry, K. W. Davidson, C. A. Doubeni, J. W. Epling, Jr., A. R. Kemper, A. H. Krist, A. E. Kurth, C. S. Landefeld, C. M. Mangione, M. G. Phipps, M. Silverstein, M. A. Simon, A. L. Siu, and C. W. Tseng. 2017. 'Screening for Thyroid Cancer: US Preventive Services Task Force Recommendation Statement', *JAMA*, 317: 1882-87.

Bibby, M. C. 2004. 'Orthotopic models of cancer for preclinical drug evaluation: advantages and disadvantages', *Eur J Cancer*, 40: 852-7.

Blomberg, M., U. Feldt-Rasmussen, K. K. Andersen, and S. K. Kjaer. 2012. 'Thyroid cancer in Denmark 1943-2008, before and after iodine supplementation', *Int J Cancer*, 131: 2360-6.

Bodet-Milin, C., A. Faivre-Chauvet, T. Carlier, A. Rauscher, M. Bourgeois, E. Cerato, V. Rohmer, O. Couturier, D. Drui, D. M. Goldenberg, R. M. Sharkey, J. Barbet, and F. Kraeber-Bodere. 2016. 'Immuno-PET Using Anticarcinoembryonic Antigen Bispecific Antibody and 68Ga-Labeled Peptide in Metastatic Medullary Thyroid Carcinoma: Clinical Optimization of the Pretargeting Parameters in a First-in-Human Trial', *J Nucl Med*, 57: 1505-11.

Boelaert, K., J. Horacek, R. L. Holder, J. C. Watkinson, M. C. Sheppard, and J. A. Franklyn. 2006. 'Serum thyrotropin concentration as a novel predictor of malignancy in thyroid nodules investigated by fine-needle aspiration', *J Clin Endocrinol Metab*, 91: 4295-301.

Boelaert, K., and C. J. McCabe. 2011. 'Thyroid cancer: finding the malignant thyroid nodule in the haystack', *Nat Rev Endocrinol*, 7: 563-4.

Bogsrud, T. V., D. Karantanis, M. A. Nathan, B. P. Mullan, G. A. Wiseman, J. L. Kasperbauer, C. C. Reading, I. D. Hay, and V. J. Lowe. 2008. '18F-FDG PET in the management of patients with anaplastic thyroid carcinoma', *Thyroid*, 18: 713-9.

Boswell, C. A., and M. W. Brechbiel. 2007. 'Development of radioimmunotherapeutic and diagnostic antibodies: an inside-out view', *Nucl Med Biol*, 34: 757-78.

Boy, C., T. Poeppel, J. Kotzerke, B. J. Krause, H. Amthauer, R. P. Baum, I. Buchmann, S. Ezziddin, D. Fuhrer, M. Gabriel, T. Kuwert, H. Lahner, T. Lauenstein, H. R. Maecke, J. Nagarajah, F. Rosch, K. Scheidhauer, M. Schmidt, M. A. Walter, and A. Bockisch. 2018. '[Somatostatin receptor PET/CT (SSTR-PET/CT)]', *Nuklearmedizin*, 57: 4-17.

Bruggemann, M., G. Winter, H. Waldmann, and M. S. Neuberger. 1989. 'The immunogenicity of chimeric antibodies', *J Exp Med*, 170: 2153-7.

Buscombe, J. R. 2007. 'Radionuclides in the management of thyroid cancer', *Cancer Imaging*, 7: 202-9.

Buther, K., M. G. Compeer, J. G. De Mey, O. Schober, M. Schafers, C. Bremer, B. Riemann, and C. Holtke. 2012. 'Assessment of endothelin-A receptor expression in subcutaneous and orthotopic thyroid carcinoma xenografts in vivo employing optical imaging methods', *Endocrinology*, 153: 2907-18.

Caobelli, F., A. Chiaravalloti, L. Evangelista, G. Saladini, O. Schillaci, M. Vadrucci, F. Scalorbi, D. Donner, P. Alongi, and Aimn Working Group Young. 2018. 'Predictive and prognostic value of 18F-DOPA PET/CT in patients affected by recurrent medullary carcinoma of the thyroid', *Ann Nucl Med*, 32: 7-15.

Cases, J. A., and M. I. Surks. 2000. 'The changing role of scintigraphy in the evaluation of thyroid nodules', *Semin Nucl Med*, 30: 81-7.

Cazzato, R. L., J. Garnon, B. Shaygi, G. Koch, G. Tsoumakidou, J. Caudrelier, P. Addeo, P. Bachellier, I. J. Namer, and A. Gangi. 2018. 'PET/CT-guided interventions: Indications, advantages, disadvantages and the state of the art', *Minim Invasive Ther Allied Technol*, 27: 27-32.

Cecchinelli, B., L. Lavra, C. Rinaldo, S. Iacovelli, A. Gurtner, A. Gasbarri, A. Ulivieri, F. Del Prete, M. Trovato, G. Piaggio, A. Bartolazzi, S. Soddu, and S. Sciacchitano. 2006. 'Repression of the antiapoptotic molecule galectin-3 by homeodomain-interacting protein kinase 2-activated p53 is required for p53-induced apoptosis', *Mol Cell Biol*, 26: 4746-57.

Chakravarty, D., E. Santos, M. Ryder, J. A. Knauf, X. H. Liao, B. L. West, G. Bollag, R. Kolesnick, T. H. Thin, N. Rosen, P. Zanzonico, S. M. Larson, S. Refetoff, R. Ghossein, and J. A. Fagin. 2011. 'Small-molecule MAPK inhibitors restore radioiodine incorporation in mouse thyroid cancers with conditional BRAF activation', *J Clin Invest*, 121: 4700-11.

Chen, J. J., N. D. LaFrance, M. D. Allo, D. S. Cooper, and P. W. Ladenson. 1988. 'Single photon emission computed tomography of the thyroid', *J Clin Endocrinol Metab*, 66: 1240-6.

Chen, W., G. Li, M. Parsons, H. Zhuang, and A. Alavi. 2007. 'Clinical Significance of Incidental Focal Versus Diffuse Thyroid Uptake on FDG-PET Imaging', *PET Clin*, 2: 321-9.

Choi, Y. L., M. K. Kim, J. W. Suh, J. Han, J. H. Kim, J. H. Yang, and S. J. Nam. 2005. 'Immunoexpression of HBME-1, high molecular weight cytokeratin, cytokeratin 19, thyroid transcription factor-1, and E-cadherin in thyroid carcinomas', *J Korean Med Sci*, 20: 853-9.

Cimitan, M., B. Busnardo, M. E. Girelli, D. Casara, and G. P. Zanatta. 1979. 'Carcinoembryonic antigen in thyroid cancer', *J Endocrinol Invest*, 2: 241-4.

Clark, Orlo H., Quan-Yang Duh, Electron Kebebew, Jessica E. Gosnell, and Wen T. Shen. 2016. *Textbook of endocrine surgery 3rd edition* (Elsevier Saunders: Philadelphia, PA).

Cooper, D. S., G. M. Doherty, B. R. Haugen, R. T. Kloos, S. L. Lee, S. J. Mandel, E. L. Mazzaferri, B. McIver, F. Pacini, M. Schlumberger, S. I. Sherman, D. L. Steward, and R. M. Tuttle. 2009. 'Revised American Thyroid Association management guidelines for patients with thyroid nodules and differentiated thyroid cancer', *Thyroid*, 19: 1167-214.

Cooper, D. S., G. M. Doherty, B. R. Haugen, R. T. Kloos, S. L. Lee, S. J. Mandel, E. L. Mazzaferri, B. McIver, S. I. Sherman, R. M. Tuttle, and Taskforce American Thyroid Association Guidelines. 2006. 'Management guidelines for patients with thyroid nodules and differentiated thyroid cancer', *Thyroid*, 16: 109-42.

Covell, D. G., J. Barbet, O. D. Holton, C. D. Black, R. J. Parker, and J. N. Weinstein. 1986. 'Pharmacokinetics of monoclonal immunoglobulin G1, F(ab')2, and Fab' in mice', *Cancer Res*, 46: 3969-78.

D'Alessandria, C., S. Braesch-Andersen, K. Bejo, S. Reder, B. Blechert, M. Schwaiger, and A. Bartolazzi. 2016. 'Noninvasive In Vivo Imaging and Biologic Characterization of Thyroid Tumors by ImmunoPET Targeting of Galectin-3', *Cancer Res*, 76: 3583-92.

Dagher, S. F., J. L. Wang, and R. J. Patterson. 1995. 'Identification of galectin-3 as a factor in pre-mRNA splicing', *Proc Natl Acad Sci U S A*, 92: 1213-7.

Dal Maso, L., C. Bosetti, C. La Vecchia, and S. Franceschi. 2009. 'Risk factors for thyroid cancer: an epidemiological review focused on nutritional factors', *Cancer Causes Control*, 20: 75-86.

Dal Maso, L., A. Tavilla, F. Pacini, D. Serraino, B. A. C. van Dijk, M. D. Chirlaque, R. Capocaccia, N. Larranaga, M. Colonna, D. Agius, E. Ardanaz, J. Rubio-Casadevall, A. Kowalska, S. Virdone, S. Mallone, H. Amash, R. De Angelis, and Eurocare- Working Group. 2017. 'Survival of 86,690 patients with thyroid cancer: A population-based study in 29 European countries from EUROCARE-5', *Eur J Cancer*, 77: 140-52.

Danese, D., S. Sciacchitano, A. Farsetti, M. Andreoli, and A. Pontecorvi. 1998. 'Diagnostic accuracy of conventional versus sonography-guided fine-needle aspiration biopsy of thyroid nodules', *Thyroid*, 8: 15-21.

Davies, L., and H. G. Welch. 2006. 'Increasing incidence of thyroid cancer in the United States, 1973-2002', *JAMA*, 295: 2164-7.

Deri, M. A., S. Ponnala, P. Kozlowski, B. P. Burton-Pye, H. T. Cicek, C. Hu, J. S. Lewis, and L. C. Francesconi. 2015. 'p-SCN-Bn-HOPO: A Superior Bifunctional Chelator for (89)Zr ImmunoPET', *Bioconjug Chem*, 26: 2579-91.

Diaz-Alvarez, L., and E. Ortega. 2017. 'The Many Roles of Galectin-3, a Multifaceted Molecule, in Innate Immune Responses against Pathogens', *Mediators Inflamm*, 2017: 9247574.

Dijkers, E. C., J. G. Kosterink, A. P. Rademaker, L. R. Perk, G. A. van Dongen, J. Bart, J. R. de Jong, E. G. de Vries, and M. N. Lub-de Hooge. 2009. 'Development and characterization of clinical-grade 89Zr-trastuzumab for HER2/neu immunoPET imaging', *J Nucl Med*, 50: 974-81.

Dohan, O., A. De la Vieja, V. Paroder, C. Riedel, M. Artani, M. Reed, C. S. Ginter, and N. Carrasco. 2003. 'The sodium/iodide Symporter (NIS): characterization, regulation, and medical significance', *Endocr Rev*, 24: 48-77.

Dumic, J., S. Dabelic, and M. Flogel. 2006. 'Galectin-3: an open-ended story', *Biochim Biophys Acta*, 1760: 616-35.

el-Desouki, M. 1991. 'Tl-201 thyroid imaging in differentiating benign from malignant thyroid nodules', *Clin Nucl Med*, 16: 425-30.

El-Galaly, T. C., L. C. Gormsen, and M. Hutchings. 2018. 'PET/CT for Staging; Past, Present, and Future', *Semin Nucl Med*, 48: 4-16.

Elad-Sfadia, G., R. Haklai, E. Balan, and Y. Kloog. 2004. 'Galectin-3 augments K-Ras activation and triggers a Ras signal that attenuates ERK but not phosphoinositide 3-kinase activity', *J Biol Chem*, 279: 34922-30.

Enewold, L., K. Zhu, E. Ron, A. J. Marrogi, A. Stojadinovic, G. E. Peoples, and S. S. Devesa. 2009. 'Rising thyroid cancer incidence in the United States by demographic and tumor characteristics, 1980-2005', *Cancer Epidemiol Biomarkers Prev*, 18: 784-91.

Eschmann, S. M., G. Reischl, K. Bilger, J. Kupferschlager, M. H. Thelen, B. M. Dohmen, H. Besenfelder, and R. Bares. 2002. 'Evaluation of dosimetry of radioiodine therapy in benign and malignant thyroid disorders by means of iodine-124 and PET', *Eur J Nucl Med Mol Imaging*, 29: 760-7.

Feine, U. 1998. 'Fluor-18-deoxyglucose positron emission tomography in differentiated thyroid cancer', *Eur J Endocrinol*, 138: 492-6.

Ferlay, J., I. Soerjomataram, R. Dikshit, S. Eser, C. Mathers, M. Rebelo, D. M. Parkin, D. Forman, and F. Bray. 2015. 'Cancer incidence and mortality worldwide: sources, methods and major patterns in GLOBOCAN 2012', *Int J Cancer*, 136: E359-86.

Fernandez, P. L., M. J. Merino, M. Gomez, E. Campo, T. Medina, V. Castronovo, X. Sanjuan, A. Cardesa, F. T. Liu, and M. E. Sobel. 1997. 'Galectin-3 and laminin expression in neoplastic and non-neoplastic thyroid tissue', *J Pathol*, 181: 80-6.

Fletcher, J. W., B. Djulbegovic, H. P. Soares, B. A. Siegel, V. J. Lowe, G. H. Lyman, R. E. Coleman, R. Wahl, J. C. Paschold, N. Avril, L. H. Einhorn, W. W. Suh, D. Samson, D. Delbeke, M. Gorman, and A. F. Shields. 2008. 'Recommendations on the use of 18F-FDG PET in oncology', *J Nucl Med*, 49: 480-508.

Fortin, M. A., A. V. Salnikov, M. Nestor, N. E. Heldin, K. Rubin, and H. Lundqvist. 2007. 'Immuno-PET of undifferentiated thyroid carcinoma with radioiodine-labelled antibody cMAb U36: application to antibody tumour uptake studies', *Eur J Nucl Med Mol Imaging*, 34: 1376-87.

Fortuna-Costa, A., A. M. Gomes, E. O. Kozlowski, M. P. Stelling, and M. S. Pavao. 2014. 'Extracellular galectin-3 in tumor progression and metastasis', *Front Oncol*, 4: 138.

Fortunati, N., M. G. Catalano, K. Arena, E. Brignardello, A. Piovesan, and G. Boccuzzi. 2004. 'Valproic acid induces the expression of the Na+/I- symporter and iodine uptake in poorly differentiated thyroid cancer cells', *J Clin Endocrinol Metab*, 89: 1006-9.

Frates, M. C., C. B. Benson, P. M. Doubilet, E. Kunreuther, M. Contreras, E. S. Cibas, J. Orcutt, F. D. Moore, Jr., P. R. Larsen, E. Marqusee, and E. K. Alexander. 2006. 'Prevalence and distribution of carcinoma in patients with solitary and multiple thyroid nodules on sonography', *J Clin Endocrinol Metab*, 91: 3411-7.

Freitas, J. E., M. D. Gross, S. Ripley, and B. Shapiro. 1985. 'Radionuclide diagnosis and therapy of thyroid cancer: current status report', *Semin Nucl Med*, 15: 106-31.

Gasbarri, A., M. P. Martegani, F. Del Prete, T. Lucante, P. G. Natali, and A. Bartolazzi. 1999. 'Galectin-3 and CD44v6 isoforms in the preoperative evaluation of thyroid nodules', *J Clin Oncol*, 17: 3494-502.

Gharib, H. 1994. 'Fine-needle aspiration biopsy of thyroid nodules: advantages, limitations, and effect', *Mayo Clin Proc*, 69: 44-9.

Gharib, H., and J. R. Goellner. 1993. 'Fine-needle aspiration biopsy of the thyroid: an appraisal', *Ann Intern Med*, 118: 282-9.

Gharib, H., J. R. Goellner, A. R. Zinsmeister, C. S. Grant, and J. A. Van Heerden. 1984. 'Fine-needle aspiration biopsy of the thyroid. The problem of suspicious cytologic findings', *Ann Intern Med*, 101: 25-8.

Gharib, H., and E. Papini. 2007. 'Thyroid nodules: clinical importance, assessment, and treatment', *Endocrinol Metab Clin North Am*, 36: 707-35, vi.

Gharib, H., E. Papini, J. R. Garber, D. S. Duick, R. M. Harrell, L. Hegedus, R. Paschke, R. Valcavi, P. Vitti, and Aace Ace Ame Task Force on Thyroid Nodules. 2016. 'American Association of Clinical Endocrinologists, American College of Endocrinology, and Associazione Medici Endocrinologi Medical Guidelines for Clinical Practice for the Diagnosis and Management of Thyroid Nodules--2016 Update', *Endocr Pract*, 22: 622-39.

Gharib, H., E. Papini, R. Paschke, D. S. Duick, R. Valcavi, L. Hegedus, P. Vitti, and Aace Ame Eta Task Force on Thyroid Nodules. 2010a. 'American Association of Clinical Endocrinologists, Associazione Medici Endocrinologi, and European Thyroid Association medical guidelines for clinical practice for the diagnosis and management of thyroid nodules', *J Endocrinol Invest*, 33: 1-50.

———. 2010b. 'American Association of Clinical Endocrinologists, Associazione Medici Endocrinologi, and European Thyroid Association medical guidelines for clinical practice for the diagnosis and management of thyroid nodules: executive summary of recommendations', *J Endocrinol Invest*, 33: 51-6.

Gharib, H., E. Papini, R. Valcavi, H. J. Baskin, A. Crescenzi, M. E. Dottorini, D. S. Duick, R. Guglielmi, C. R. Hamilton, Jr., M. A. Zeiger, M. Zini, and Aace Ame Task Force on Thyroid Nodules. 2006. 'American Association of Clinical Endocrinologists and Associazione Medici Endocrinologi medical guidelines for clinical practice for the diagnosis and management of thyroid nodules', *Endocr Pract*, 12: 63-102.

Gilliland, F. D., W. C. Hunt, D. M. Morris, and C. R. Key. 1997. 'Prognostic factors for thyroid carcinoma. A population-based study of 15,698 cases from the Surveillance, Epidemiology and End Results (SEER) program 1973-1991', *Cancer*, 79: 564-73.

Giraudet, A. L., and D. Taieb. 2017. 'PET imaging for thyroid cancers: Current status and future directions', *Ann Endocrinol (Paris)*, 78: 38-42.

Glunde, K., M. F. Penet, L. Jiang, M. A. Jacobs, and Z. M. Bhujwalla. 2015. 'Choline metabolism-based molecular diagnosis of cancer: an update', *Expert Rev Mol Diagn*, 15: 735-47.

Goellner, J. R., H. Gharib, C. S. Grant, and D. A. Johnson. 1987. 'Fine needle aspiration cytology of the thyroid, 1980 to 1986', *Acta Cytol*, 31: 587-90.

Goetz, J. G., B. Joshi, P. Lajoie, S. S. Strugnell, T. Scudamore, L. D. Kojic, and I. R. Nabi. 2008. 'Concerted regulation of focal adhesion dynamics by galectin-3 and tyrosine-phosphorylated caveolin-1', *J Cell Biol*, 180: 1261-75.

Goldenberg, D. M. 1993. 'Monoclonal antibodies in cancer detection and therapy', *Am J Med*, 94: 297-312.

Gottschalk, Alexander. 1988. *Diagnostic nuclear medicine* (Williams & Wilkins: Baltimore).

Griffith, O. L., C. G. Chiu, A. M. Gown, S. J. Jones, and S. M. Wiseman. 2008. 'Biomarker panel diagnosis of thyroid cancer: a critical review', *Expert Rev Anticancer Ther*, 8: 1399-413.

Hamburger, J. I., and S. W. Hamburger. 1986. 'Fine needle biopsy of thyroid nodules: avoiding the pitfalls', *N Y State J Med*, 86: 241-9.

Hara, H., N. Fulton, T. Yashiro, K. Ito, L. J. DeGroot, and E. L. Kaplan. 1994. 'N-ras mutation: an independent prognostic factor for aggressiveness of papillary thyroid carcinoma', *Surgery*, 116: 1010-6.

Harding, F. A., M. M. Stickler, J. Razo, and R. B. DuBridge. 2010. 'The immunogenicity of humanized and fully human antibodies: residual immunogenicity resides in the CDR regions', *MAbs*, 2: 256-65.

Harmsen, M. M., and H. J. De Haard. 2007. 'Properties, production, and applications of camelid single-domain antibody fragments', *Appl Microbiol Biotechnol*, 77: 13-22.

Haugen, B. R., E. K. Alexander, K. C. Bible, G. M. Doherty, S. J. Mandel, Y. E. Nikiforov, F. Pacini, G. W. Randolph, A. M. Sawka, M. Schlumberger, K. G. Schuff, S. I. Sherman, J. A. Sosa, D. L. Steward, R. M. Tuttle, and L. Wartofsky. 2016. '2015 American Thyroid Association Management Guidelines for Adult Patients with Thyroid Nodules and Differentiated Thyroid Cancer: The American Thyroid Association Guidelines Task Force on Thyroid Nodules and Differentiated Thyroid Cancer', *Thyroid*, 26: 1-133.

Haymart, M. R., S. L. Glinberg, J. Liu, R. S. Sippel, J. C. Jaume, and H. Chen. 2009. 'Higher serum TSH in thyroid cancer patients occurs independent of age and correlates with extrathyroidal extension', *Clin Endocrinol (Oxf)*, 71: 434-9.

Hegedus, L. 2004. 'Clinical practice. The thyroid nodule', *N Engl J Med*, 351: 1764-71.

Herlyn, D., M. Herlyn, Z. Steplewski, and H. Koprowski. 1979. 'Monoclonal antibodies in cell-mediated cytotoxicity against human melanoma and colorectal carcinoma', *Eur J Immunol*, 9: 657-9.

Heskamp, S., R. Raave, O. Boerman, M. Rijpkema, V. Goncalves, and F. Denat. 2017. '(89)Zr-Immuno-Positron Emission Tomography in Oncology: State-of-the-Art (89)Zr Radiochemistry', *Bioconjug Chem*, 28: 2211-23.

Heskamp, S., H. W. van Laarhoven, J. D. Molkenboer-Kuenen, G. M. Franssen, Y. M. Versleijen-Jonkers, W. J. Oyen, W. T. van der Graaf, and O. C. Boerman. 2010. 'ImmunoSPECT and immunoPET of IGF-1R expression with the radiolabeled antibody R1507 in a triple-negative breast cancer model', *J Nucl Med*, 51: 1565-72.

Holland, J. P., V. Divilov, N. H. Bander, P. M. Smith-Jones, S. M. Larson, and J. S. Lewis. 2010. '89Zr-DFO-J591 for immunoPET of prostate-specific membrane antigen expression in vivo', *J Nucl Med*, 51: 1293-300.

Honjo, Y., P. Nangia-Makker, H. Inohara, and A. Raz. 2001. 'Down-regulation of galectin-3 suppresses tumorigenicity of human breast carcinoma cells', *Clin Cancer Res*, 7: 661-8.

Hooft, L., A. A. van der Veldt, O. S. Hoekstra, M. Boers, C. F. Molthoff, and P. J. van Diest. 2008. 'Hexokinase III, cyclin A and galectin-3 are overexpressed in malignant follicular thyroid nodules', *Clin Endocrinol (Oxf)*, 68: 252-7.

Hughes, R. C. 2001. 'Galectins as modulators of cell adhesion', *Biochimie*, 83: 667-76.

Hundahl, S. A., B. Cady, M. P. Cunningham, E. Mazzaferri, R. F. McKee, J. Rosai, J. P. Shah, A. M. Fremgen, A. K. Stewart, and S. Holzer. 2000. 'Initial results from a prospective cohort study of 5583 cases of thyroid carcinoma treated in the united states during 1996. U.S. and German Thyroid Cancer Study Group. An American College of Surgeons Commission on Cancer Patient Care Evaluation study', *Cancer*, 89: 202-17.

Hundahl, S. A., I. D. Fleming, A. M. Fremgen, and H. R. Menck. 1998. 'A National Cancer Data Base report on 53,856 cases of thyroid carcinoma treated in the U.S., 1985-1995 [see commetns]', *Cancer*, 83: 2638-48.

Huston, J. S., D. Levinson, M. Mudgett-Hunter, M. S. Tai, J. Novotny, M. N. Margolies, R. J. Ridge, R. E. Bruccoleri, E. Haber, R. Crea, and et al. 1988. 'Protein engineering of antibody binding sites: recovery of specific activity in an anti-digoxin single-chain Fv analogue produced in Escherichia coli', *Proc Natl Acad Sci U S A*, 85: 5879-83.

Ikemori, R. Y., C. M. Machado, K. M. Furuzawa, S. Nonogaki, E. Osinaga, K. Umezawa, M. A. de Carvalho, L. Verinaud, and R. Chammas. 2014. 'Galectin-3 up-regulation in hypoxic and nutrient deprived microenvironments promotes cell survival', *PLoS One*, 9: e111592.

Inohara, H., Y. Honjo, T. Yoshii, S. Akahani, J. Yoshida, K. Hattori, S. Okamoto, T. Sawada, A. Raz, and T. Kubo. 1999. 'Expression of galectin-3 in fine-needle aspirates as a diagnostic marker differentiating benign from malignant thyroid neoplasms', *Cancer*, 85: 2475-84.

Inohara, H., and A. Raz. 1995. 'Functional evidence that cell surface galectin-3 mediates homotypic cell adhesion', *Cancer Res*, 55: 3267-71.

Jain, R. K. 1990. 'Physiological barriers to delivery of monoclonal antibodies and other macromolecules in tumors', *Cancer Res*, 50: 814s-19s.

Jegerlehner, Sabrina, Jean-Luc Bulliard, Drahomir Aujesky, Nicolas Rodondi, Simon Germann, Isabelle Konzelmann, Arnaud Chiolero, and Nicer Working Group. 2017. 'Overdiagnosis and overtreatment of thyroid cancer: A population-based temporal trend study', *PLoS ONE*, 12: e0179387.

Jones, T. 1996. 'The role of positron emission tomography within the spectrum of medical imaging', *Eur J Nucl Med*, 23: 207-11.

Kahramangil, B., and E. Berber. 2017. 'The use of near-infrared fluorescence imaging in endocrine surgical procedures', *J Surg Oncol*, 115: 848-55.

Kasai, K., and J. Hirabayashi. 1996. 'Galectins: a family of animal lectins that decipher glycocodes', *J Biochem*, 119: 1-8.

Kauhanen, S., M. Seppanen, J. Ovaska, H. Minn, J. Bergman, P. Korsoff, P. Salmela, J. Saltevo, T. Sane, M. Valimaki, and P. Nuutila. 2009. 'The clinical value of [18F]fluoro-dihydroxyphenylalanine positron emission tomography in primary diagnosis, staging, and restaging of neuroendocrine tumors', *Endocr Relat Cancer*, 16: 255-65.

Keller, S., T. Angrisano, E. Florio, R. Pero, M. Decaussin-Petrucci, G. Troncone, M. Capasso, F. Lembo, A. Fusco, and L. Chiariotti. 2013. 'DNA methylation state of the galectin-3 gene represents a potential new marker of thyroid malignancy', *Oncol Lett*, 6: 86-90.

Kendall, E. C. 1915. 'The isolation in crystalline form for the compound containing iodin, which occurs in the thyroid - Its chemical nature and physiologic activity', *Journal of the American Medical Association*, 64: 2042-43.

Kennedy, P. J., C. Oliveira, P. L. Granja, and B. Sarmento. 2018. 'Monoclonal antibodies: technologies for early discovery and engineering', *Crit Rev Biotechnol*, 38: 394-408.

Khoshnevisan, A., M. Jauregui-Osoro, K. Shaw, J. B. Torres, J. D. Young, N. K. Ramakrishnan, A. Jackson, G. E. Smith, A. D. Gee, and P. J. Blower. 2016. '[(18)F]tetrafluoroborate as a PET tracer for the sodium/iodide symporter: the importance of specific activity', *EJNMMI Res*, 6: 34.

Kim, E. J., B. S. Kim, D. B. Choi, S. G. Chi, and T. H. Choi. 2016. 'Enhanced tumor retention of radioiodinated anti-epidermal growth factor receptor antibody using novel bifunctional iodination linker for radioimmunotherapy', *Oncol Rep*, 35: 3159-68.

Kim, H. R., H. M. Lin, H. Biliran, and A. Raz. 1999. 'Cell cycle arrest and inhibition of anoikis by galectin-3 in human breast epithelial cells', *Cancer Res*, 59: 4148-54.

Kim, M. J., E. K. Kim, S. I. Park, B. M. Kim, J. Y. Kwak, S. J. Kim, J. H. Youk, and S. H. Park. 2008. 'US-guided fine-needle aspiration of thyroid nodules: indications, techniques, results', *Radiographics*, 28: 1869-86; discussion 87.

Kim, S., Y. W. Park, B. A. Schiff, D. D. Doan, Y. Yazici, S. A. Jasser, M. Younes, M. Mandal, B. N. Bekele, and J. N. Myers. 2005. 'An orthotopic model of anaplastic thyroid carcinoma in athymic nude mice', *Clin Cancer Res*, 11: 1713-21.

Kitahara, C. M., and J. A. Sosa. 2016. 'The changing incidence of thyroid cancer', *Nat Rev Endocrinol*, 12: 646-53.

Kohatsu, L., D. K. Hsu, A. G. Jegalian, F. T. Liu, and L. G. Baum. 2006. 'Galectin-3 induces death of Candida species expressing specific beta-1,2-linked mannans', *J Immunol*, 177: 4718-26.

Kohler, G., and C. Milstein. 1975. 'Continuous cultures of fused cells secreting antibody of predefined specificity', *Nature*, 256: 495-7.

Kondo, T., S. Ezzat, and S. L. Asa. 2006. 'Pathogenetic mechanisms in thyroid follicular-cell neoplasia', *Nat Rev Cancer*, 6: 292-306.

Kukis, D. L., G. L. DeNardo, S. J. DeNardo, G. R. Mirick, L. A. Miers, D. P. Greiner, and C. F. Meares. 1995. 'Effect of the extent of chelate substitution on the immunoreactivity and biodistribution of 2IT-BAT-Lym-1 immunoconjugates', *Cancer Res*, 55: 878-84.

La Vecchia, C., M. Malvezzi, C. Bosetti, W. Garavello, P. Bertuccio, F. Levi, and E. Negri. 2015. 'Thyroid cancer mortality and incidence: a global overview', *Int J Cancer*, 136: 2187-95.

Le Marer, N. 2000. 'GALECTIN-3 expression in differentiating human myeloid cells', *Cell Biol Int*, 24: 245-51.

Learoyd, D. L., P. J. Roach, G. M. Briggs, L. W. Delbridge, E. G. Wilmshurst, and B. G. Robinson. 1997. 'Technetium-99m-sestamibi scanning in recurrent medullary thyroid carcinoma', *J Nucl Med*, 38: 227-30.

Lepur, A., E. Salomonsson, U. J. Nilsson, and H. Leffler. 2012. 'Ligand induced galectin-3 protein self-association', *J Biol Chem*, 287: 21751-6.

Li, D., C. Lei, Z. Xu, F. Yang, H. Liu, Z. Zhu, S. Li, X. Liu, H. Shu, and H. Zheng. 2016. 'Foot-and-mouth disease virus non-structural protein 3A inhibits the interferon-beta signaling pathway', *Sci Rep*, 6: 21888.

Li, Y., Z. Li, X. Wang, F. Liu, Y. Cheng, B. Zhang, and D. Shi. 2012. 'In vivo cancer targeting and imaging-guided surgery with near infrared-emitting quantum dot bioconjugates', *Theranostics*, 2: 769-76.

Lin, C. I., E. E. Whang, D. B. Donner, X. Jiang, B. D. Price, A. M. Carothers, T. Delaine, H. Leffler, U. J. Nilsson, V. Nose, F. D. Moore, Jr., and D. T. Ruan. 2009. 'Galectin-3 targeted therapy with a small molecule inhibitor activates apoptosis and enhances both chemosensitivity and radiosensitivity in papillary thyroid cancer', *Mol Cancer Res*, 7: 1655-62.

Lindmo, T., E. Boven, F. Cuttitta, J. Fedorko, and P. A. Bunn, Jr. 1984. 'Determination of the immunoreactive fraction of radiolabeled monoclonal antibodies by linear extrapolation to binding at infinite antigen excess', *J Immunol Methods*, 72: 77-89.

Liska, J., V. Altanerova, S. Galbavy, S. Stvrtina, and J. Brtko. 2005. 'Thyroid tumors: histological classification and genetic factors involved in the development of thyroid cancer', *Endocr Regul*, 39: 73-83.

Liu, Y., L. Su, and H. Xiao. 2017. 'Review of Factors Related to the Thyroid Cancer Epidemic', *Int J Endocrinol*, 2017: 5308635.

Livak, K. J., and T. D. Schmittgen. 2001. 'Analysis of relative gene expression data using real-time quantitative PCR and the 2(-Delta Delta C(T)) Method', *Methods*, 25: 402-8.

Lloyd, Ricardo V., Robert Y. Osamura, Guenter Kloeppel, Juan Rosai, Fred T. Bosman, Elaine S. Jaffe, Sunil R. Lakhani, Hiroko Ohgaki, World Health Organization., and International Agency for Research on Cancer. 2017. *WHO classification of tumours of endocrine organs*.

Lopez-Campistrous, A., E. E. Adewuyi, M. G. K. Benesch, Y. M. Ko, R. Lai, A. Thiesen, J. Dewald, P. Wang, K. Chu, S. Ghosh, D. C. Williams, L. J. Vos, D. N. Brindley, and T. P. W. McMullen. 2016. 'PDGFRalpha Regulates Follicular Cell Differentiation Driving Treatment Resistance and Disease Recurrence in Papillary Thyroid Cancer', *EBioMedicine*, 12: 86-97.

Lubitz, C. C., C. Y. Kong, P. M. McMahon, G. H. Daniels, Y. Chen, K. P. Economopoulos, G. S. Gazelle, and M. C. Weinstein. 2014. 'Annual financial impact of well-differentiated thyroid cancer care in the United States', *Cancer*, 120: 1345-52.

Lutje, S., J. Cohnen, B. Gomez, J. Gruneisen, L. Sawicki, H. Rubben, A. Bockisch, L. Umutlu, T. D. Poppel, and A. Wetter. 2017. 'Integrated (68)Ga-HBED-CC-PSMA-PET/MRI in patients with suspected recurrent prostate cancer', *Nuklearmedizin*, 56: 73-81.

Lutje, S., B. Gomez, J. Cohnen, L. Umutlu, M. Gotthardt, T. D. Poeppel, A. Bockisch, and S. Rosenbaum-Krumme. 2017. 'Imaging of Prostate-Specific Membrane Antigen Expression in Metastatic Differentiated Thyroid Cancer Using 68Ga-HBED-CC-PSMA PET/CT', *Clin Nucl Med*, 42: 20-25.

Ma, M. T., L. K. Meszaros, B. M. Paterson, D. J. Berry, M. S. Cooper, Y. Ma, R. C. Hider, and P. J. Blower. 2015. 'Tripodal tris(hydroxypyridinone) ligands for immunoconjugate PET imaging with (89)Zr(4+): comparison with desferrioxamine-B', *Dalton Trans*, 44: 4884-900.

Marcu, L., E. Bezak, and B. J. Allen. 2018. 'Global comparison of targeted alpha vs targeted beta therapy for cancer: In vitro, in vivo and clinical trials', *Crit Rev Oncol Hematol*, 123: 7-20.

Marine, D. 1915. 'Quantitative studies on the in vivo absorption of iodine by dogs' thyroid glands.', *Journal of Biological Chemistry*, 22: 547-50.

Marotta, V., A. Guerra, M. R. Sapio, and M. Vitale. 2011. 'RET/PTC rearrangement in benign and malignant thyroid diseases: a clinical standpoint', *Eur J Endocrinol*, 165: 499-507.

Marques, A. R., C. Espadinha, M. J. Frias, L. Roque, A. L. Catarino, L. G. Sobrinho, and V. Leite. 2004. 'Underexpression of peroxisome proliferator-activated receptor (PPAR)gamma in PAX8/PPARgamma-negative thyroid tumours', *Br J Cancer*, 91: 732-8.

Marqusee, E., C. B. Benson, M. C. Frates, P. M. Doubilet, P. R. Larsen, E. S. Cibas, and S. J. Mandel. 2000. 'Usefulness of ultrasonography in the management of nodular thyroid disease', *Ann Intern Med*, 133: 696-700.

Marti-Climent, J. M., M. Collantes, M. Jauregui-Osoro, G. Quincoces, E. Prieto, I. Bilbao, M. Ecay, J. A. Richter, and I. Penuelas. 2015. 'Radiation dosimetry and biodistribution in non-human primates of the sodium/iodide PET ligand [(18)F]-tetrafluoroborate', *EJNMMI Res*, 5: 70.

Marzola, M. C., M. R. Pelizzo, M. Ferdeghini, A. Toniato, A. Massaro, V. Ambrosini, S. Fanti, M. D. Gross, A. Al-Nahhas, and D. Rubello. 2010. 'Dual PET/CT with (18)F-DOPA and (18)F-FDG in metastatic medullary thyroid carcinoma and rapidly increasing calcitonin levels: Comparison with conventional imaging', *Eur J Surg Oncol*, 36: 414-21.

Maublant, J. C., Z. Zhang, M. Rapp, M. Ollier, J. Michelot, and A. Veyre. 1993. 'In vitro uptake of technetium-99m-teboroxime in carcinoma cell lines and normal cells: comparison with technetium-99m-sestamibi and thallium-201', *J Nucl Med*, 34: 1949-52.

Mazurek, N., Y. J. Sun, J. E. Price, L. Ramdas, W. Schober, P. Nangia-Makker, J. C. Byrd, A. Raz, and R. S. Bresalier. 2005. 'Phosphorylation of galectin-3 contributes to malignant transformation of human epithelial cells via modulation of unique sets of genes', *Cancer Res*, 65: 10767-75.

Mazzaferri, E. L. 1993. 'Management of a solitary thyroid nodule', *N Engl J Med*, 328: 553-9.

McBride, W. J., R. M. Sharkey, H. Karacay, C. A. D'Souza, E. A. Rossi, P. Laverman, C. H. Chang, O. C. Boerman, and D. M. Goldenberg. 2009. 'A novel method of 18F radiolabeling for PET', *J Nucl Med*, 50: 991-8.

Meijs, W. E., H. J. Haisma, R. P. Klok, F. B. van Gog, E. Kievit, H. M. Pinedo, and J. D. Herscheid. 1997. 'Zirconium-labeled monoclonal antibodies and their distribution in tumor-bearing nude mice', *J Nucl Med*, 38: 112-8.

Middendorp, M., I. Selkinski, C. Happel, W. T. Kranert, and F. Grunwald. 2010. 'Comparison of positron emission tomography with [(18)F]FDG and [(68)Ga]DOTATOC in recurrent differentiated thyroid cancer: preliminary data', *Q J Nucl Med Mol Imaging*, 54: 76-83.

Minchinton, A. I., and I. F. Tannock. 2006. 'Drug penetration in solid tumours', *Nat Rev Cancer*, 6: 583-92.

Morgenstern, A., F. Bruchertseifer, and C. Apostolidis. 2012. 'Bismuth-213 and actinium-225 -- generator performance and evolving therapeutic applications of two generator-derived alpha-emitting radioisotopes', *Curr Radiopharm*, 5: 221-7.

Morris, L. G., N. Riaz, A. Desrichard, Y. Senbabaoglu, A. A. Hakimi, V. Makarov, J. S. Reis-Filho, and T. A. Chan. 2016. 'Pan-cancer analysis of intratumor heterogeneity as a prognostic determinant of survival', *Oncotarget*, 7: 10051-63.

Morris, L. G., R. M. Tuttle, and L. Davies. 2016. 'Changing Trends in the Incidence of Thyroid Cancer in the United States', *JAMA Otolaryngol Head Neck Surg*, 142: 709-11.

Morrison, J. A., L. A. Pike, G. Lund, Q. Zhou, B. E. Kessler, K. T. Bauerle, S. B. Sams, B. R. Haugen, and R. E. Schweppe. 2015. 'Characterization of thyroid cancer cell lines in murine orthotopic and intracardiac metastasis models', *Horm Cancer*, 6: 87-99.

Mortensen, J. D., L. B. Woolner, and W. A. Bennett. 1955. 'Gross and microscopic findings in clinically normal thyroid glands', *J Clin Endocrinol Metab*, 15: 1270-80.

Mosci, C., and A. Iagaru. 2011. 'PET/CT imaging of thyroid cancer', *Clin Nucl Med*, 36: e180-5.

Musholt, T. J., T. Clerici, H. Dralle, A. Frilling, P. E. Goretzki, M. M. Hermann, J. Kussmann, K. Lorenz, C. Nies, J. Schabram, P. Schabram, C. Scheuba, D. Simon, T. Steinmuller, A. W. Trupka, R. A. Wahl, A. Zielke, A. Bockisch, W. Karges, M. Luster, K. W. Schmid, and Surgeons Interdisciplinary Task Force Guidelines of the German Association of Endocrine. 2011. 'German Association of Endocrine Surgeons practice guidelines for the surgical treatment of benign thyroid disease', *Langenbecks Arch Surg*, 396: 639-49.

Nakahara, Hideomi, and Takashi Sagawa. 1996. *Kyodai kagaku gijutsu ga Nihon o hakaisuru : senkan Yamato no ayamachi o kurikaesuna = Japan will be destroyed by hyper-science* (Taiyō Kikaku Shuppan: Tōkyō).

Nakahara, S., N. Oka, and A. Raz. 2005. 'On the role of galectin-3 in cancer apoptosis', *Apoptosis*, 10: 267-75.

Nakamoto, Y., M. Tatsumi, D. Hammoud, C. Cohade, M. M. Osman, and R. L. Wahl. 2005. 'Normal FDG distribution patterns in the head and neck: PET/CT evaluation', *Radiology*, 234: 879-85.

Nangia-Makker, P., V. Balan, and A. Raz. 2012. 'Galectin-3 binding and metastasis', *Methods Mol Biol*, 878: 251-66.

Nangia-Makker, P., Y. Honjo, R. Sarvis, S. Akahani, V. Hogan, K. J. Pienta, and A. Raz. 2000. 'Galectin-3 induces endothelial cell morphogenesis and angiogenesis', *Am J Pathol*, 156: 899-909.

Negro, R., G. Greco, and E. Colosimo. 2017. 'Ultrasound Risk Categories for Thyroid Nodules and Cytology Results: A Single Institution's Experience after the Adoption of the 2016 Update of Medical Guidelines by the American Association of Clinical Endocrinologists and Associazione Medici Endocrinologi', *J Thyroid Res*, 2017: 8135415.

Neta, G., P. Rajaraman, A. Berrington de Gonzalez, M. M. Doody, B. H. Alexander, D. Preston, S. L. Simon, D. Melo, J. Miller, D. M. Freedman, M. S. Linet, and A. J. Sigurdson. 2013. 'A prospective study of medical diagnostic radiography and risk of thyroid cancer', *Am J Epidemiol*, 177: 800-9.

Nikiforov, Y. E. 2006. 'Radiation-induced thyroid cancer: what we have learned from chernobyl', *Endocr Pathol*, 17: 307-17.

Nikiforov, Y. E., R. R. Seethala, G. Tallini, Z. W. Baloch, F. Basolo, L. D. Thompson, J. A. Barletta, B. M. Wenig, A. Al Ghuzlan, K. Kakudo, T. J. Giordano, V. A. Alves, E. Khanafshar, S. L. Asa, A. K. El-Naggar, W. E. Gooding, S. P. Hodak, R. V. Lloyd, G. Maytal, O. Mete, M. N. Nikiforova, V. Nose, M. Papotti, D. N. Poller, P. M. Sadow, A. S. Tischler, R. M. Tuttle, K. B. Wall, V. A. LiVolsi, G. W. Randolph, and R. A. Ghossein. 2016. 'Nomenclature Revision for Encapsulated Follicular Variant of Papillary Thyroid Carcinoma: A Paradigm Shift to Reduce Overtreatment of Indolent Tumors', *JAMA Oncol*, 2: 1023-9.

Nikiforova, M. N., P. W. Biddinger, C. M. Caudill, T. G. Kroll, and Y. E. Nikiforov. 2002. 'PAX8-PPARgamma rearrangement in thyroid tumors: RT-PCR and immunohistochemical analyses', *Am J Surg Pathol*, 26: 1016-23.

Nikiforova, M. N., E. T. Kimura, M. Gandhi, P. W. Biddinger, J. A. Knauf, F. Basolo, Z. Zhu, R. Giannini, G. Salvatore, A. Fusco, M. Santoro, J. A. Fagin, and Y. E. Nikiforov. 2003. 'BRAF mutations in thyroid tumors are restricted to papillary carcinomas and anaplastic

or poorly differentiated carcinomas arising from papillary carcinomas', *J Clin Endocrinol Metab*, 88: 5399-404.

Nikiforova, M. N., R. A. Lynch, P. W. Biddinger, E. K. Alexander, G. W. Dorn, 2nd, G. Tallini, T. G. Kroll, and Y. E. Nikiforov. 2003. 'RAS point mutations and PAX8-PPAR gamma rearrangement in thyroid tumors: evidence for distinct molecular pathways in thyroid follicular carcinoma', *J Clin Endocrinol Metab*, 88: 2318-26.

Nikiforova, M. N., and Y. E. Nikiforov. 2009. 'Molecular diagnostics and predictors in thyroid cancer', *Thyroid*, 19: 1351-61.

Nilsson, I. L., F. Arnberg, J. Zedenius, and A. Sundin. 2011. 'Thyroid incidentaloma detected by fluorodeoxyglucose positron emission tomography/computed tomography: practical management algorithm', *World J Surg*, 35: 2691-7.

Nishida, T., S. Katayama, M. Tsujimoto, J. Nakamura, and H. Matsuda. 1999. 'Clinicopathological significance of poorly differentiated thyroid carcinoma', *Am J Surg Pathol*, 23: 205-11.

Nisonoff, A., F. C. Wissler, L. N. Lipman, and D. L. Woernley. 1960. 'Separation of univalent fragments from the bivalent rabbit antibody molecule by reduction of disulfide bonds', *Arch Biochem Biophys*, 89: 230-44.

Nucera, C., M. A. Nehs, M. Mekel, X. Zhang, R. Hodin, J. Lawler, V. Nose, and S. Parangi. 2009. 'A novel orthotopic mouse model of human anaplastic thyroid carcinoma', *Thyroid*, 19: 1077-84.

O'Doherty, J., M. Jauregui-Osoro, T. Brothwood, T. Szyszko, P. K. Marsden, M. J. O'Doherty, G. J. R. Cook, P. J. Blower, and V. Lewington. 2017. '(18)F-Tetrafluoroborate, a PET Probe for Imaging Sodium/Iodide Symporter Expression: Whole-Body Biodistribution, Safety, and Radiation Dosimetry in Thyroid Cancer Patients', *J Nucl Med*, 58: 1666-71.

O'Neill, C. J., L. Vaughan, D. L. Learoyd, S. B. Sidhu, L. W. Delbridge, and M. S. Sywak. 2011. 'Management of follicular thyroid carcinoma should be individualised based on degree of capsular and vascular invasion', *Eur J Surg Oncol*, 37: 181-5.

Ochi, H., H. Sawa, T. Fukuda, Y. Inoue, H. Nakajima, Y. Masuda, T. Okamura, Y. Onoyama, S. Sugano, H. Ohkita, Y. Tei, K. Kamino, and Y. Kobayashi. 1982. 'Thallium-201-chloride thyroid scintigraphy to evaluate benign and/or malignant nodules: usefulness of the delayed scan', *Cancer*, 50: 236-40.

Pal, T., F. D. Vogl, P. O. Chappuis, R. Tsang, J. Brierley, H. Renard, K. Sanders, T. Kantemiroff, S. Bagha, D. E. Goldgar, S. A. Narod, and W. D. Foulkes. 2001. 'Increased risk for nonmedullary thyroid cancer in the first degree relatives of prevalent cases of nonmedullary thyroid cancer: a hospital-based study', *J Clin Endocrinol Metab*, 86: 5307-12.

Pandya, D. N., N. Bhatt, H. Yuan, C. S. Day, B. M. Ehrmann, M. Wright, U. Bierbach, and T. J. Wadas. 2017. 'Zirconium tetraazamacrocycle complexes display extraordinary stability and provide a new strategy for zirconium-89-based radiopharmaceutical development', *Chem Sci*, 8: 2309-14.

Papini, E. 2003. 'The dilemma of non-palpable thyroid nodules', *J Endocrinol Invest*, 26: 3-4.

Papini, E., R. Guglielmi, A. Bianchini, A. Crescenzi, S. Taccogna, F. Nardi, C. Panunzi, R. Rinaldi, V. Toscano, and C. M. Pacella. 2002. 'Risk of malignancy in nonpalpable thyroid nodules: predictive value of ultrasound and color-Doppler features', *J Clin Endocrinol Metab*, 87: 1941-6.

Pappalardo, V., S. La Rosa, A. Imperatori, N. Rotolo, M. L. Tanda, A. Sessa, L. Dominioni, and G. Dionigi. 2016. 'Thyroid cancer with tracheal invasion: a pathological estimation', *Gland Surg*, 5: 541-45.

Pazaitou-Panayiotou, K., M. Capezzone, and F. Pacini. 2007. 'Clinical features and therapeutic implication of papillary thyroid microcarcinoma', *Thyroid*, 17: 1085-92.

Peng, W., H. Y. Wang, Y. Miyahara, G. Peng, and R. F. Wang. 2008. 'Tumor-associated galectin-3 modulates the function of tumor-reactive T cells', *Cancer Res*, 68: 7228-36.

Penna, G. C., F. Vaisman, M. Vaisman, M. Sobrinho-Simoes, and P. Soares. 2016. 'Molecular Markers Involved in Tumorigenesis of Thyroid Carcinoma: Focus on Aggressive Histotypes', *Cytogenet Genome Res*, 150: 194-207.

Pentlow, K. S., M. C. Graham, R. M. Lambrecht, N. K. Cheung, and S. M. Larson. 1991. 'Quantitative imaging of I-124 using positron emission tomography with applications to radioimmunodiagnosis and radioimmunotherapy', *Med Phys*, 18: 357-66.

Perk, L. R., G. W. Visser, M. J. Vosjan, M. Stigter-van Walsum, B. M. Tijink, C. R. Leemans, and G. A. van Dongen. 2005. '(89)Zr as a PET surrogate radioisotope for scouting biodistribution of the therapeutic radiometals (90)Y and (177)Lu in tumor-bearing nude mice after coupling to the internalizing antibody cetuximab', *J Nucl Med*, 46: 1898-906.

Peterson, E., P. De, and R. Nuttall. 2012. 'BMI, diet and female reproductive factors as risks for thyroid cancer: a systematic review', *PLoS One*, 7: e29177.

Phung, Y. T., D. Barbone, V. C. Broaddus, and M. Ho. 2011. 'Rapid generation of in vitro multicellular spheroids for the study of monoclonal antibody therapy', *J Cancer*, 2: 507-14.

Pinchera, A., F. Aghini-Lombardi, L. Antonangeli, and P. Vitti. 1996. '[Multinodular goiter. Epidemiology and prevention]', *Ann Ital Chir*, 67: 317-25.

Pisarek, H., T. Stepien, R. Kubiak, E. Borkowska, and M. Pawlikowski. 2009. 'Expression of somatostatin receptor subtypes in human thyroid tumors: the immunohistochemical and molecular biology (RT-PCR) investigation', *Thyroid Res*, 2: 1.

Popoveniuc, G., and J. Jonklaas. 2012. 'Thyroid nodules', *Med Clin North Am*, 96: 329-49.

Porter, R. R. 1959. 'The hydrolysis of rabbit y-globulin and antibodies with crystalline papain', *Biochem J*, 73: 119-26.

Powsner, Rachel A., and Edward R. Powsner. 2006. *Essential nuclear medicine physics* (Blackwell Pub.: Malden, Mass.).

Prasad, M. L., N. S. Pellegata, Y. Huang, H. N. Nagaraja, A. de la Chapelle, and R. T. Kloos. 2005. 'Galectin-3, fibronectin-1, CITED-1, HBME1 and cytokeratin-19 immunohistochemistry is useful for the differential diagnosis of thyroid tumors', *Mod Pathol*, 18: 48-57.

Pressman, D. , and G. Keighley. 1948. 'The zone of activity of antibodies as determined by the use of radioactive tracers; the zone of activity of nephrotoxic anti-kidney serum.', *J Immunol*, 59: 141-46.

Pugliese, G., C. Iacobini, C. M. Pesce, and S. Menini. 2015. 'Galectin-3: an emerging all-out player in metabolic disorders and their complications', *Glycobiology*, 25: 136-50.

Qi, J., N. Li, K. Fan, P. Yin, C. Zhao, Z. Li, Y. Lin, L. Wang, and X. Zha. 2014. 'beta1,6 GlcNAc branches-modified PTPRT attenuates its activity and promotes cell migration by STAT3 pathway', *PLoS One*, 9: e98052.

Rabes, H. M., E. P. Demidchik, J. D. Sidorow, E. Lengfelder, C. Beimfohr, D. Hoelzel, and S. Klugbauer. 2000. 'Pattern of radiation-induced RET and NTRK1 rearrangements in 191 post-chernobyl papillary thyroid carcinomas: biological, phenotypic, and clinical implications', *Clin Cancer Res*, 6: 1093-103.

Rago, T., M. Scutari, F. Santini, V. Loiacono, P. Piaggi, G. Di Coscio, F. Basolo, P. Berti, A. Pinchera, and P. Vitti. 2010. 'Real-time elastosonography: useful tool for refining the presurgical diagnosis in thyroid nodules with indeterminate or nondiagnostic cytology', *J Clin Endocrinol Metab*, 95: 5274-80.

Rago, T., and P. Vitti. 2008. 'Role of thyroid ultrasound in the diagnostic evaluation of thyroid nodules', *Best Pract Res Clin Endocrinol Metab*, 22: 913-28.

Rahbari, R., L. Zhang, and E. Kebebew. 2010. 'Thyroid cancer gender disparity', *Future Oncol*, 6: 1771-9.

Rashidian, M., J. R. Ingram, M. Dougan, A. Dongre, K. A. Whang, C. LeGall, J. J. Cragnolini, B. Bierie, M. Gostissa, J. Gorman, G. M. Grotenbreg, A. Bhan, R. A. Weinberg, and H. L. Ploegh. 2017. 'Predicting the response to CTLA-4 blockade by longitudinal noninvasive monitoring of CD8 T cells', *J Exp Med*, 214: 2243-55.

Reiners, C., K. Wegscheider, H. Schicha, P. Theissen, R. Vaupel, R. Wrbitzky, and P. M. Schumm-Draeger. 2004. 'Prevalence of thyroid disorders in the working population of Germany: ultrasonography screening in 96,278 unselected employees', *Thyroid*, 14: 926-32.

Ricarte-Filho, J. C., M. Ryder, D. A. Chitale, M. Rivera, A. Heguy, M. Ladanyi, M. Janakiraman, D. Solit, J. A. Knauf, R. M. Tuttle, R. A. Ghossein, and J. A. Fagin. 2009. 'Mutational

profile of advanced primary and metastatic radioactive iodine-refractory thyroid cancers reveals distinct pathogenetic roles for BRAF, PIK3CA, and AKT1', *Cancer Res*, 69: 4885-93.

Riesco-Eizaguirre, G., P. Gutierrez-Martinez, M. A. Garcia-Cabezas, M. Nistal, and P. Santisteban. 2006. 'The oncogene BRAF V600E is associated with a high risk of recurrence and less differentiated papillary thyroid carcinoma due to the impairment of Na+/I- targeting to the membrane', *Endocr Relat Cancer*, 13: 257-69.

Roman, B. R., L. G. Morris, and L. Davies. 2017. 'The thyroid cancer epidemic, 2017 perspective', *Curr Opin Endocrinol Diabetes Obes*, 24: 332-36.

Rosato, L., N. Avenia, P. Bernante, M. De Palma, G. Gulino, P. G. Nasi, M. R. Pelizzo, and L. Pezzullo. 2004. 'Complications of thyroid surgery: analysis of a multicentric study on 14,934 patients operated on in Italy over 5 years', *World J Surg*, 28: 271-6.

Rousseaux, J., R. Rousseaux-Prevost, and H. Bazin. 1983. 'Optimal conditions for the preparation of Fab and F(ab')2 fragments from monoclonal IgG of different rat IgG subclasses', *J Immunol Methods*, 64: 141-6.

Ruhlmann, M., W. Jentzen, V. Ruhlmann, C. Pettinato, G. Rossi, I. Binse, A. Bockisch, and S. Rosenbaum-Krumme. 2016. 'High Level of Agreement Between Pretherapeutic 124I PET and Intratherapeutic 131I Imaging in Detecting Iodine-Positive Thyroid Cancer Metastases', *J Nucl Med*, 57: 1339-42.

Ryman, J. T., and B. Meibohm. 2017. 'Pharmacokinetics of Monoclonal Antibodies', *CPT Pharmacometrics Syst Pharmacol*, 6: 576-88.

Salajegheh, A., E. Dolan-Evans, E. Sullivan, S. Irani, M. A. Rahman, H. Vosgha, V. Gopalan, R. A. Smith, and A. K. Lam. 2014. 'The expression profiles of the galectin gene family in primary and metastatic papillary thyroid carcinoma with particular emphasis on galectin-1 and galectin-3 expression', *Exp Mol Pathol*, 96: 212-8.

Santhanam, P., L. B. Solnes, and S. P. Rowe. 2017. 'Molecular imaging of advanced thyroid cancer: iodinated radiotracers and beyond', *Med Oncol*, 34: 189.

Sathekge, M. M., R. B. Mageza, M. N. Muthuphei, M. C. Modiba, and R. C. Clauss. 2001. 'Evaluation of thyroid nodules with technetium-99m MIBI and technetium-99m pertechnetate', *Head Neck*, 23: 305-10.

Sawin, C. T., and D. V. Becker. 1997. 'Radioiodine and the treatment of hyperthyroidism: the early history', *Thyroid*, 7: 163-76.

Schlapschy, M., U. Binder, C. Borger, I. Theobald, K. Wachinger, S. Kisling, D. Haller, and A. Skerra. 2013. 'PASylation: a biological alternative to PEGylation for extending the plasma half-life of pharmaceutically active proteins', *Protein Eng Des Sel*, 26: 489-501.

Schmidt, M. M., and K. D. Wittrup. 2009. 'A modeling analysis of the effects of molecular size and binding affinity on tumor targeting', *Mol Cancer Ther*, 8: 2861-71.

Sciacchitano, S., L. Lavra, A. Morgante, A. Ulivieri, F. Magi, G. P. De Francesco, C. Bellotti, L. B. Salehi, and A. Ricci. 2018. 'Galectin-3: One Molecule for an Alphabet of Diseases, from A to Z', *Int J Mol Sci*, 19.

Scott-Combes, D., and R. Kinsman. 2007. *The British Association of Endocrine Surgeons: Second National Audit Report 2007* (Dendrite Clinical Systems Ltd: Oxfordshire, United Kingdom).

Segev, D. L., D. P. Clark, M. A. Zeiger, and C. Umbricht. 2003. 'Beyond the suspicious thyroid fine needle aspirate. A review', *Acta Cytol*, 47: 709-22.

Seidlin, S. M., L. D. Marinelli, and E. Oshry. 1946. 'Radioactive iodine therapy; effect on functioning metastases of adenocarcinoma of the thyroid', *J Am Med Assoc*, 132: 838-47.

Semmler, W., and Markus Schwaiger. 1997. *Impact of molecular biology and new technical developments on diagnostic imaging* (Springer: Berlin ; New York).

Serafini, A. N. 1993. 'From monoclonal antibodies to peptides and molecular recognition units: an overview', *J Nucl Med*, 34: 533-6.

Sewell, W., A. Reeb, and R. Y. Lin. 2013. 'An orthotopic mouse model of anaplastic thyroid carcinoma', *J Vis Exp*.

Shankar, J., S. M. Wiseman, F. Meng, K. Kasaian, S. Strugnell, A. Mofid, A. Gown, S. J. Jones, and I. R. Nabi. 2012. 'Coordinated expression of galectin-3 and caveolin-1 in thyroid cancer', *J Pathol*, 228: 56-66.

Siegel, R. L., K. D. Miller, and A. Jemal. 2015. 'Cancer statistics, 2015', *CA Cancer J Clin*, 65: 5-29.

———. 2018. 'Cancer statistics, 2018', *CA Cancer J Clin*, 68: 7-30.

Singh, T. D., S. Y. Jeong, S. W. Lee, J. H. Ha, I. K. Lee, S. H. Kim, J. Kim, S. J. Cho, B. C. Ahn, J. Lee, and Y. H. Jeon. 2015. 'Inverse Agonist of Estrogen-Related Receptor gamma Enhances Sodium Iodide Symporter Function Through Mitogen-Activated Protein Kinase Signaling in Anaplastic Thyroid Cancer Cells', *J Nucl Med*, 56: 1690-6.

Slominski, A., J. Wortsman, L. Kohn, K. B. Ain, G. M. Venkataraman, A. Pisarchik, J. H. Chung, C. Giuliani, M. Thornton, G. Slugocki, and D. J. Tobin. 2002. 'Expression of hypothalamic-pituitary-thyroid axis related genes in the human skin', *J Invest Dermatol*, 119: 1449-55.

Spitzweg, C., W. Joba, W. Eisenmenger, and A. E. Heufelder. 1998. 'Analysis of human sodium iodide symporter gene expression in extrathyroidal tissues and cloning of its complementary deoxyribonucleic acids from salivary gland, mammary gland, and gastric mucosa', *J Clin Endocrinol Metab*, 83: 1746-51.

Stabin, M. G., R. B. Sparks, and E. Crowe. 2005. 'OLINDA/EXM: the second-generation personal computer software for internal dose assessment in nuclear medicine', *J Nucl Med*, 46: 1023-7.

Stewart, G. A., and D. R. Stanworth. 1975. 'The effect of acid treatment upon the susceptibility of rabbit IgG to proteolytic cleavage with various enzymes', *Immunochemistry*, 12: 713-21.

Sun, G. H., S. DeMonner, and M. M. Davis. 2013. 'Epidemiological and economic trends in inpatient and outpatient thyroidectomy in the United States, 1996-2006', *Thyroid*, 23: 727-33.

Takenaka, Y., H. Inohara, T. Yoshii, K. Oshima, S. Nakahara, S. Akahani, Y. Honjo, Y. Yamamoto, A. Raz, and T. Kubo. 2003. 'Malignant transformation of thyroid follicular cells by galectin-3', *Cancer Lett*, 195: 111-9.

Tan, G. H., and H. Gharib. 1997. 'Thyroid incidentalomas: management approaches to nonpalpable nodules discovered incidentally on thyroid imaging', *Ann Intern Med*, 126: 226-31.

Thery, C., M. Boussac, P. Veron, P. Ricciardi-Castagnoli, G. Raposo, J. Garin, and S. Amigorena. 2001. 'Proteomic analysis of dendritic cell-derived exosomes: a secreted subcellular compartment distinct from apoptotic vesicles', *J Immunol*, 166: 7309-18.

Thurber, G. M., M. M. Schmidt, and K. D. Wittrup. 2008. 'Antibody tumor penetration: transport opposed by systemic and antigen-mediated clearance', *Adv Drug Deliv Rev*, 60: 1421-34.

Townsend, D. W. 2008. 'Combined positron emission tomography-computed tomography: the historical perspective', *Semin Ultrasound CT MR*, 29: 232-5.

Tran Cao, H. S., S. Kaushal, C. S. Snyder, W. M. Ongkeko, R. M. Hoffman, and M. Bouvet. 2010. 'Real-time imaging of tumor progression in a fluorescent orthotopic mouse model of thyroid cancer', *Anticancer Res*, 30: 4415-22.

Traub-Weidinger, T., D. Putzer, E. von Guggenberg, G. Dobrozemsky, B. Nilica, D. Kendler, R. Bale, and I. J. Virgolini. 2015. 'Multiparametric PET imaging in thyroid malignancy characterizing tumour heterogeneity: somatostatin receptors and glucose metabolism', *Eur J Nucl Med Mol Imaging*, 42: 1995-2001.

Tufano, R. P., S. I. Noureldine, and P. Angelos. 2015. 'Incidental thyroid nodules and thyroid cancer: considerations before determining management', *JAMA Otolaryngol Head Neck Surg*, 141: 566-72.

Turner, J. W., and R. P. Spencer. 1976. 'Thyroid carcinoma presenting as a pertechnetate "hot" nodule, but without 131I uptake: case report', *J Nucl Med*, 17: 22-3.

Tuttle, R. M. 2018. 'Controversial Issues in Thyroid Cancer Management', *J Nucl Med*, 59: 1187-94.

Untergasser, A., I. Cutcutache, T. Koressaar, J. Ye, B. C. Faircloth, M. Remm, and S. G. Rozen. 2012. 'Primer3--new capabilities and interfaces', *Nucleic Acids Res*, 40: e115.

Vaccarella, S., L. Dal Maso, M. Laversanne, F. Bray, M. Plummer, and S. Franceschi. 2015. 'The Impact of Diagnostic Changes on the Rise in Thyroid Cancer Incidence: A Population-Based Study in Selected High-Resource Countries', *Thyroid*, 25: 1127-36.

Vaccarella, S., S. Franceschi, F. Bray, C. P. Wild, M. Plummer, and L. Dal Maso. 2016. 'Worldwide Thyroid-Cancer Epidemic? The Increasing Impact of Overdiagnosis', *N Engl J Med*, 375: 614-7.

Vahrmeijer, A. L., M. Hutteman, J. R. van der Vorst, C. J. van de Velde, and J. V. Frangioni. 2013. 'Image-guided cancer surgery using near-infrared fluorescence', *Nat Rev Clin Oncol*, 10: 507-18.

Van Nostrand, D., S. Moreau, V. V. Bandaru, F. Atkins, S. Chennupati, M. Mete, K. Burman, and L. Wartofsky. 2010. '(124)I positron emission tomography versus (131)I planar imaging in the identification of residual thyroid tissue and/or metastasis in patients who have well-differentiated thyroid cancer', *Thyroid*, 20: 879-83.

Volante, M., P. Collini, Y. E. Nikiforov, A. Sakamoto, K. Kakudo, R. Katoh, R. V. Lloyd, V. A. LiVolsi, M. Papotti, M. Sobrinho-Simoes, G. Bussolati, and J. Rosai. 2007. 'Poorly differentiated thyroid carcinoma: the Turin proposal for the use of uniform diagnostic criteria and an algorithmic diagnostic approach', *Am J Surg Pathol*, 31: 1256-64.

Vugts, D. J., C. Klaver, C. Sewing, A. J. Poot, K. Adamzek, S. Huegli, C. Mari, G. W. Visser, I. E. Valverde, G. Gasser, T. L. Mindt, and G. A. van Dongen. 2017. 'Comparison of the octadentate bifunctional chelator DFO*-pPhe-NCS and the clinically used hexadentate bifunctional chelator DFO-pPhe-NCS for (89)Zr-immuno-PET', *Eur J Nucl Med Mol Imaging*, 44: 286-95.

Vugts, D. J., and G. A. van Dongen. 2011. '(89)Zr-labeled compounds for PET imaging guided personalized therapy', *Drug Discov Today Technol*, 8: e53-61.

Wagner, M., M. Wuest, I. Hamann, A. Lopez-Campistrous, T. P. W. McMullen, and F. Wuest. 2018. 'Molecular imaging of platelet-derived growth factor receptor-alpha (PDGFRalpha) in papillary thyroid cancer using immuno-PET', *Nucl Med Biol*, 58: 51-58.

Wang, L., H. Inohara, K. J. Pienta, and A. Raz. 1995. 'Galectin-3 is a nuclear matrix protein which binds RNA', *Biochem Biophys Res Commun*, 217: 292-303.

Wang, L. Y., B. R. Roman, J. C. Migliacci, F. L. Palmer, R. M. Tuttle, A. R. Shaha, J. P. Shah, S. G. Patel, and I. Ganly. 2015. 'Cost-effectiveness analysis of papillary thyroid cancer surveillance', *Cancer*, 121: 4132-40.

Wang, W., H. Macapinlac, S. M. Larson, S. D. Yeh, T. Akhurst, R. D. Finn, J. Rosai, and R. J. Robbins. 1999. '[18F]-2-fluoro-2-deoxy-D-glucose positron emission tomography localizes residual thyroid cancer in patients with negative diagnostic (131)I whole body scans and elevated serum thyroglobulin levels', *J Clin Endocrinol Metab*, 84: 2291-302.

Warburg, O., F. Wind, and E. Negelein. 1927. 'The Metabolism of Tumors in the Body', *Journal of General Physiology*, 8: 519-30.

Wartofsky, L. 2010. 'Increasing world incidence of thyroid cancer: increased detection or higher radiation exposure?', *Hormones (Athens)*, 9: 103-8.

Werk, E. E., Jr., B. M. Vernon, J. J. Gonzalez, P. C. Ungaro, and R. C. McCoy. 1984. 'Cancer in thyroid nodules. A community hospital survey', *Arch Intern Med*, 144: 474-6.

Williams, D. 2008. 'Radiation carcinogenesis: lessons from Chernobyl', *Oncogene*, 27 Suppl 2: S9-18.

Wolff, J. 1964. 'Transport of Iodide and Other Anions in the Thyroid Gland', *Physiol Rev*, 44: 45-90.

Wong, K. J., K. E. Baidoo, T. K. Nayak, K. Garmestani, M. W. Brechbiel, and D. E. Milenic. 2011. 'In Vitro and In Vivo Pre-Clinical Analysis of a F(ab')(2) Fragment of Panitumumab for Molecular Imaging and Therapy of HER1 Positive Cancers', *EJNMMI Res*, 1.

Wreesmann, V. B., R. A. Ghossein, M. Hezel, D. Banerjee, A. R. Shaha, R. M. Tuttle, J. P. Shah, P. H. Rao, and B. Singh. 2004. 'Follicular variant of papillary thyroid carcinoma:

genome-wide appraisal of a controversial entity', *Genes Chromosomes Cancer*, 40: 355-64.

Xin, M., X. W. Dong, and X. L. Guo. 2015. 'Role of the interaction between galectin-3 and cell adhesion molecules in cancer metastasis', *Biomed Pharmacother*, 69: 179-85.

Xing, M., D. Clark, H. Guan, M. Ji, A. Dackiw, K. A. Carson, M. Kim, A. Tufaro, P. Ladenson, M. Zeiger, and R. Tufano. 2009. 'BRAF mutation testing of thyroid fine-needle aspiration biopsy specimens for preoperative risk stratification in papillary thyroid cancer', *J Clin Oncol*, 27: 2977-82.

Xing, M., W. H. Westra, R. P. Tufano, Y. Cohen, E. Rosenbaum, K. J. Rhoden, K. A. Carson, V. Vasko, A. Larin, G. Tallini, S. Tolaney, E. H. Holt, P. Hui, C. B. Umbricht, S. Basaria, M. Ewertz, A. P. Tufaro, J. A. Califano, M. D. Ringel, M. A. Zeiger, D. Sidransky, and P. W. Ladenson. 2005. 'BRAF mutation predicts a poorer clinical prognosis for papillary thyroid cancer', *J Clin Endocrinol Metab*, 90: 6373-9.

Yamada, K. M., and E. Cukierman. 2007. 'Modeling tissue morphogenesis and cancer in 3D', *Cell*, 130: 601-10.

Yeh, M. W., A. J. Bauer, V. A. Bernet, R. L. Ferris, L. A. Loevner, S. J. Mandel, L. A. Orloff, G. W. Randolph, D. L. Steward, and Force American Thyroid Association Surgical Affairs Committee Writing Task. 2015. 'American Thyroid Association statement on preoperative imaging for thyroid cancer surgery', *Thyroid*, 25: 3-14.

Yoshii, T., T. Fukumori, Y. Honjo, H. Inohara, H. R. Kim, and A. Raz. 2002. 'Galectin-3 phosphorylation is required for its anti-apoptotic function and cell cycle arrest', *J Biol Chem*, 277: 6852-7.

Yusufi, N., S. Mall, H. O. Bianchi, K. Steiger, S. Reder, R. Klar, S. Audehm, M. Mustafa, S. Nekolla, C. Peschel, M. Schwaiger, A. M. Krackhardt, and C. D'Alessandria. 2017. 'In-depth Characterization of a TCR-specific Tracer for Sensitive Detection of Tumor-directed Transgenic T Cells by Immuno-PET', *Theranostics*, 7: 2402-16.

Zhai, C., D. Summer, C. Rangger, G. M. Franssen, P. Laverman, H. Haas, M. Petrik, R. Haubner, and C. Decristoforo. 2015. 'Novel Bifunctional Cyclic Chelator for (89)Zr Labeling-Radiolabeling and Targeting Properties of RGD Conjugates', *Mol Pharm*, 12: 2142-50.

Zhou, Y., T. Arai, Y. Horiguchi, K. Ino, T. Matsue, and H. Shiku. 2013. 'Multiparameter analyses of three-dimensionally cultured tumor spheroids based on respiratory activity and comprehensive gene expression profiles', *Anal Biochem*, 439: 187-93.

Ziemianska, K., J. Kopczynski, and A. Kowalska. 2016. 'Repeated nondiagnostic result of thyroid fine-needle aspiration biopsy', *Contemp Oncol (Pozn)*, 20: 491-95.

8 **ACKNOWLEDGMENTS**

I would like to thank Prof. Dr. Markus Schwaiger for being my first advisor and for offering me the opportunity to do my PhD at the Department of Nuclear Medicine.

I would like to express my deepest gratitude to my mentor, P.D. Dr. Calogero D'Alessandria, for having me as part of his workgroup, for supervising me and for his guidance and patience.

I'm extremely grateful to Prof. Dr. Gabriele Multhoff for being my second advisor, providing me useful suggestions in my project as well as in our collaborations.

I'm also grateful to Prof. Dr. Wolfgang Weber, for the support to my project, and to Prof. Dr. Armando Bartolazzi, whose work and findings were the essential base of my project.

Special thanks to Prof. Dr. Angela Otto and Joseph Hintermair for their help with cell cultures.

I'd like to acknowledge our PET technicians Sybille Reder and Markus Mittelhäuser, their (hard) work was fundamental for my project.

I am grateful for the contribution of Dr. Katja Steiger and her group in immunohistochemical studies, and for the help provided by the group of Prof. Dr. Angela Krackhardt, in particular Sabine Mall, in PCR analyses.

Thanks also to Dr. Miriam Bräuer for training me for animal handling, Dr. Stefan Stangl for flow cytometry measurements, Prof. Dr. Dieter Saur for providing the US system, and Dr. Stephan Nekolla for dosimetric studies. Furthermore, I am grateful to all my other colleagues, too many to be mentioned one by one, for the practical suggestions, helpful advice and nice talks we had during these years.

Finally, I would like to thank everyone who supported me from "outside"; my Elena for all the love and care past, present and future, my family, in particular my brother Ivan and my parents, that I always feel next to me despite the distance, and my friends for their unconditional support.